

Max-Planck-Institut für Biochemie  
Abteilung für Molekulare Strukturbiologie

# **Noise Reduction and Segmentation Techniques Developed for Multidimensional Electron Microscopy of Biological Specimens**

**Achilleas S. Frangakis**

Vollständiger Abdruck der von der Fakultät für Physik der  
Technischen Universität München  
zur Erlangung des akademischen Grades eines

Doktors der Naturwissenschaften

genehmigten Dissertation.

Vorsitzender: Univ.-Prof. Dr. J. L. van Hemmen  
Prüfer der Dissertation: 1. Univ.-Prof. Dr. E. Sackmann  
2. apl. Prof. Dr. W. Baumeister

Die Dissertation wurde am 15-2-2001 bei der Technischen Universität München  
eingereicht und durch die Fakultät für Physik am 8-5-2001 angenommen.



## **Acknowledgments**

First and foremost I would like to thank Dr. R. Hegerl for supporting my work in every possible way. His approach to image processing problems, his care in research and his advice have proven invaluable.

I am grateful to Prof. W. Baumeister for creating a fantastic framework around the electron microscopy group, pursuing a great scientific challenge.

I want to thank Prof. E. Sackmann for reviewing my thesis and allowing me to graduate in his department.

From my colleagues I would like to point out Jochen Böhm. His unique way of approaching and solving problems helped to deepen into every discussion. It was always a pleasure working with him!

A big thank you goes to my friends and colleagues Günter Pfeifer, Stephan Nickell, Erika Seemüller, Michael Nitsch, Barbara Kapelari, Arne Stoschek, Dieter Typke, Dimitris Genaris and Stavros Panageas for many helpful discussions. Apart from the scientific part, maybe most important was the psychological support. Each of them has had a big influence on the success of the thesis.

I grateful to Dani Nicastro for being helpful and patient in pointing out the importance and the biological significance of the projects, as well as trying to explain complicated biological procedures.

I want to thank Beate Rockel, Rachel Horowitz, and Rudo Grimm, who provided most of the data used in this thesis. The development of appropriate methods was a real challenge.

Last but not least I want to thank my parents. Without their love and help nothing would have been possible.



## Abstract

Computed tomography techniques are the most widely applicable non-invasive methods for giving unique insights into the three dimensional (3D) organization of pleomorphic biological objects. Recent advances in the recording schemes improve the speed and resolution and provide new insights into the structural organization of different specimens. The boundaries in the applicability are set by dose limitation, limited accessibility of the data and resolution. In electron tomography the resolution limits are improved down to 2-4 nm, which should allow the identification of large biological macromolecules in their native environment. However the low signal to noise ratio hinders the application of image processing methods for data analysis, such as visualization, segmentation and feature extraction. In this thesis four image processing techniques have been developed and implemented in the field of electron microscopy in order to improve the performance in terms of signal reconstruction, processing time and visualization.

A new noise reduction (denoising) technique is proposed based on nonlinear anisotropic diffusion. Diffusion methods for signal reconstruction became widely applicable due to their well-established mathematical properties and their general well posedness. Several different methods have been proposed mainly focused on edge detection and edge preservation, but none of them became applicable for highly degraded data. A new hybrid approach has been developed, which combines conventional diffusion methods and overcomes the handicaps of the present realizations. This diffusion technique shows a superior performance as compared to existing diffusion realizations, as well as to conventional methods typically applied in image processing (e.g. low pass filtering, median filtering) and invariant wavelet filtering. Several quantitative measures to assess the signal reconstruction performance have been established. The best reconstruction performance is observed at spatial frequencies lower than half of the Nyquist frequency. The method is therefore appropriate for the mostly oversampled electron microscopic data. The signal to noise ratio improvement is demonstrated by means of Fourier shell correlation functions. Several examples demonstrating the significant improvement of the visualization quality of the data sets are presented. Additionally the method proves to be an excellent preprocessing step for object detection and segmentation techniques.

Mean curvature motion is a novel approach for object detection. It is a nonlinear anisotropic diffusion process, where the diffusion flux is explicitly set to zero in the direction of the gradient. As the level sets of the image (isointensity contours) move as a function of their own curvature, they degrade to concave regions and disappear to singularities, which can be detected a posteriori indicating the position of a feature. This method can be applied as a preprocessing step for object detection in two-dimensions (2D) as well as in 3D is robust with respect to noise (for a signal to noise ratio larger than 0.1) and rotational and translation invariant. Additionally is also a parameter-free

method since the only parameter, which has to be determined (iteration time) depends directly on the size of the feature to be identified. An extended performance evaluation on real and artificial data, as well as with an interactively selected data set is presented.

Automatic grouping and segmentation is a challenging problem in the image-processing field. The main goal of image segmentation is an image simplification, such that the interesting parts of the image are separated from each other and the effective size of the image reduces to the substantial part. Decreasing of the effective processing size and improvement of the visualization capabilities are the two most important effects of each segmentation technique. A segmentation procedure is in general not objective, as compared when different individuals perceive distinct features as the important objects in the image. Two techniques covering a broad field have been developed, the active contours as an interactive segmentation tool and an eigenvector based approach for automated image analysis.

The “snake” segmentation based on the movement of an active contour towards a detectable boundary has been applied at various image processing applications. Nevertheless, due to the missing wedge, the low signal to noise ratio and the pleomorphic features is not directly applicable for interactive segmentation in the field of electron microscopy. A modification of the partial differential equations is proposed in order to block the level set movement in the direction of the missing information. The technique remains very sensitive to the initial conditions and is therefore not applicable for automated segmentation. Interactively the user has the option to determine an arbitrary boundary, near to the object of interest, which will be approached by the snake in a finite time. Application examples in 2D and 3D are presented.

The use of eigenvectors for segmentation of multidimensional images in the field of electron microscopy is a novel approach. With the use of the second smallest eigenvector of an affinity matrix containing similarity measures between the pixels a foreground/background separation is attained. Several similarity measures e.g. distance, gray value, texture can be implemented in the algorithm. The most dominant feature in the image could be always automatically segmented improving the visualization significantly. The parameter choice turns out to be very robust, making the method widely applicable for various 2D and 3D electron microscopic images.

## Contents

<b>Abstract .....</b>	<b>i</b>
<b>Chapter 1 .....</b>	<b>1</b>
<b>Multidimensional Electron Microscopy of Biological Specimens .....</b>	<b>1</b>
1.1 Introduction.....	1
1.2 Transmission Electron Microscopy .....	3
1.3 Noise Model.....	5
1.4 Specimen Preparation .....	6
1.5 Three-Dimensional Electron Tomographic Reconstruction .....	7
<b>Chapter 2 .....</b>	<b>9</b>
<b>Nonlinear Anisotropic Diffusion .....</b>	<b>9</b>
2.1 Diffusion Types .....	10
2.1.1 Linear Diffusion.....	10
2.1.2 Nonlinear Isotropic Diffusion.....	10
2.1.3 Nonlinear Anisotropic Diffusion .....	10
2.1.4 Properties of the Diffusion Processes .....	12
2.2 Comparison of Different Diffusion Methods.....	13
2.2.1 2D Synthetic Data .....	13
2.2.2 Pleomorphic Cellular Structures.....	14
2.3 Comparison of the Hybrid Diffusion Approach with Invariant Wavelet Transform Filtering.....	20
2.3.1 Synthetic Data.....	20
2.3.2 Three-Dimensional Biological and Medical Data .....	23
2.4 Notes on Denoising Strategies.....	29
2.5 Correlation Averaging as a Method to Evaluate the Transfer Function of the Nonlinear Anisotropic Diffusion Process .....	31
2.5.1 Frequency Equalization .....	32
2.5.2 Assessment of the Performance on Real Electron Microscopic Data.....	34
2.6 Discussion.....	35
<b>Chapter 3 .....</b>	<b>37</b>
<b>Object Detection in 2D and 3D Electron Microscopic Images..</b>	<b>37</b>
3.1 The Algorithm.....	38
3.1.1 Mean Curvature Motion.....	38
3.1.2 Peak Search Method .....	41
3.2 Object Detection with Simulated EM Data .....	41
3.2.1 Detection in 2D Images .....	42
3.2.2 Detection in Volume Data .....	43

3.3 Application on Real Data.....	44
3.3.1 2D Processing .....	44
3.3.2 Comparison of the Performance of Interactive Particle Detection and Automatic Procedure .....	45
3.3.3 3D Processing .....	47
3.4 Discussion.....	48
<b>Chapter 4.....</b>	<b>51</b>
<b>Multidimensional Image Segmentation with Active Contours. 51</b>	
4.1 Segmentation Technique.....	52
4.1.1 Discretization Scheme .....	54
4.1.2 Initialization of the Segmentation Curve .....	55
4.2 Missing Wedge Compensation with a modified Discretization Stencil .....	55
4.3 Performance Study of Snake Segmentation.....	56
4.3.1 Two Dimensional Electron Microscopic Data.....	56
4.3.2 Simulations on 3D Synthetic Data.....	60
4.3.3 Snake Segmentation of Three Dimensional Electron Microscopic Data.....	60
4.4 Discussion .....	62
<b>Chapter 5.....</b>	<b>65</b>
<b>Multidimensional Image Segmentation with Eigenvectors.....</b>	<b>65</b>
5.1 Algorithm.....	66
5.1.1 Graph theoretical approach.....	66
5.1.2 Construction of the Affinity Matrix.....	66
5.1.3 Algorithms for Graph Partition.....	68
5.1.4 Implementation of the Algorithm .....	69
5.2 Segmentation Results.....	70
5.2.1 2D Segmentation.....	70
5.2.2 Segmentation of 2D Single Particle Images .....	73
5.2.3 Segmentation of 3D Images.....	75
5.3 Discussion.....	80
<b>References.....</b>	<b>81</b>

## Chapter 1

# Multidimensional Electron Microscopy of Biological Specimens

### 1.1 Introduction

In recent years the importance of non-invasive 3D imaging in several fields related to biology and medicine has rapidly grown. This growth has been fostered by improvements in imaging modalities as well as by the widening availability of powerful hardware for computing and visualizing 3D image data. The boundaries in the applicability of these 3D imaging techniques are usually set by dose limitations, exposure time, and resolution. The closer one approaches these boundaries – which is always the goal in any area – the more degraded the recorded signal becomes. Statistical processes in the recorded data severely aggravate the automated data analysis procedures, which include visualization, feature extraction, and segmentation. These image-processing problems are particularly demanding in the field of electron microscopy.

Two-dimensional electron microscopy and electron tomography (three-dimensional electron microscopy) are by no means new imaging techniques (Hoppe 1968, Hart 1968, De Rosier and Klug 1972). Nevertheless due to recent developments in hardware and software the ultimate goal of molecular resolution when imaging small pleomorphic biological objects, such as cells and subcellular structures in a near-to-native state, has come significantly closer to being attained. The identification and visualization of macromolecular structures in a cellular context with a resolution of approximately 2-4 nm should be possible with the constraint of a good signal-to-noise ratio (SNR) (Boehm et al. 2000). Due to the irradiation sensitivity of biological samples the dose has to be restricted to the minimum needed for statistically defined images. Therefore the unambiguous identification of macromolecular structures in unperturbed cellular compartments is not yet feasible. By means of correlation techniques the tomographic reconstruction is scanned with templates created from high-resolution objects obtained from techniques as X-ray crystallography, nuclear magnetic resonance (NMR) spectroscopy, and electron microscopy. These high-resolution techniques are based on the averaging of thousand or even several hundred thousand molecules and achieve a remarkable resolution (Nitsch et al. 1998). The combination of electron tomography and known high-resolution structures will allow the determination of the position of individual macromolecules within the cellular environment, and will provide new

insights into the spatial distribution and functional interactions of molecular machines inside the cell.

To achieve a sufficiently high SNR for visualization and identification, powerful hardware and software are necessary. Additionally, a good preparation technique is essential in order to preserve the specimen properties as a snapshot of its native state as well as to prevent radiation damage. Even though significant improvement has been made during recent years the SNR remains unsatisfactory. Most of the electron tomographic reconstructions suffer from a very low SNR, which make further scrutiny of the sample very difficult. Therefore a good signal improvement technique (“denoising” technique) is necessary. Additionally the investigation of more complex and rather thick objects increases the image complexity. Image simplification techniques (interactive or automated) are necessary for separating the image into parts with similar or coherent properties, which improve the visualization capabilities as a consequence of focusing the 3D images on the parts of most interest and minimizing their size to the substantial parts.

In this thesis four methods have been developed and implemented in order to pursue the above mentioned goals, namely: (a) a hybrid approach for nonlinear anisotropic diffusion, as a noise reduction method, (b) mean curvature motion for object detection, (c) snakes or active contour models for interactive image segmentation and (d) eigenvector segmentation for fully automated region-based segmentation. They are mainly based on partial differential equations (PDE) and most of them can be expressed through the heat equation. PDE based methods are one of the best mathematically founded techniques in image processing, therefore stable algorithms can be found.

Nonlinear anisotropic diffusion was proposed as an edge-detection and edge-enhancing technique in the early 90’s (Perona and Malik 1988). The properties of linear diffusion as well as the scale space properties of the nonlinear and anisotropic realizations established this method in the field of computer science. Nevertheless for denoising of EM data none of these methods are appropriate. A novel version of nonlinear anisotropic diffusion is introduced, which outperforms other diffusion denoising methods, standard techniques (e.g. low-pass filtering, median filtering), and rotation invariant wavelet filtering, with respect to denoising performance (SNR improvement, cross-correlation coefficient, etc.). In addition to the significant SNR enhancement achieved by this variant the visual impression appears even better. The visualization of the data is facilitated and especially in 3D overcomes the human perception ability (Frangakis et. al 2001). This method is furthermore an excellent preprocessing step for the methods applied subsequently.

With a small modification of the diffusion equation the so-called mean curvature motion is achieved. Mean curvature motion was first proposed by Alvarez et. al (1993) as the ultimate edge-enhancing technique due to its total anisotropy. After some mathematical calculations it was proven that it is equivalent to the movement of the level sets of an image as a function of the local curvature. Due to severe modifications of the image properties, which is a highly undesirable property for qualitative image analysis, the method is not appropriate for “further” edge-enhancement or denoising. A novel application of this method is as an automatic object detection method. Object detection

is very important in electron microscopy because the most important noise reduction technique is based on correlation averaging of several thousand identical copies of the same object. The collection of these objects is a very time consuming task and subjected to the human subjectivity. The common techniques for object selection are usually based on correlation. In this manner the signal properties buried in the noise are exploited. With mean curvature motion a different strategy is proposed, in which signal preservation no more plays an essential role, as is usual in every other object detection and denoising technique. On the contrary, signal and noise are eliminated in parallel, under the assumption that the structure of the objects is significantly larger than the noise and therefore the curvature lower. Processing with MCM creates singularities which correspond to the position of the object (Boehm et. al 2000). The approach has several benefits for instance it is rotational invariant, fast, and independent from user-dependent parameters.

Denoising and edge-enhancing the 3D images improve the image representation significantly; nevertheless they do not simplify the image context. In order to achieve a good visualization, segmentation of the 3D image is usually necessary. The segmentation procedure separates the image in places with coherent properties. It can be automated or semi-automated as the user or the application requires. A segmentation procedure, in contrast to denoising can not be objective, but is always dependent on subjective interactions. The segmentation techniques can be separated into two larger groups: contour-based and region-based approaches. In the contour based approaches a curve (also called snake) is pushed towards an object and stops at the detectable boundary (Kass et. al 1988). An advantage of this kind of approach is that the user can interact with the boundary in order to force a “correct” segmentation. Region-based techniques make the decision by defining a global objective function. The advantage thereby is that decisions are made when information from the whole image is taken into account.

In contrast to snakes, eigenvectors segmentation belongs to the region-based approaches and produces a result after the whole image has been taken into account at the same time (Malik et. al 2000). The advantage thereby is that no premature decisions are taken. For this region-based segmentation the information contained in the first eigenvectors of an affinity matrix, describing the similarity connection between different pixels, is taken into account. With this approach a foreground/background separation is attained. Several similarity criteria can be integrated in the algorithm in order to facilitate the segmentation procedure. The algorithm possesses of one tremendous virtue: The segmentation results have been always satisfying.

## 1.2 Transmission Electron Microscopy

Electron microscopy is the only technique capable of visualizing molecular interactions in a cellular context, with a resolution in the nanometer range. The performance of the visualization is strongly dependent on the specimen preparation and the electron microscope itself.

The image formation is the result of the interaction of an electron beam with the Coulomb potential of the specimen and the subsequent magnification by the objective lens. Thin biological objects are weakly forward scattering phase objects, therefore the image is approximately a projection of the density distribution, which is in its part linearly related to the Coulomb potential of the specimen. The electrons interact with atoms by elastic and inelastic scattering. Bright-field contrast is produced either by intercepting the electrons scattered at angles larger than the objective aperture (scattering contrast) or by interference between the scattered wave and the incident wave at the image point (phase contrast). In transmission electron microscopy both the elastically scattered and the inelastically scattered electrons contribute to the image intensity, nevertheless for thin and weakly scattering specimens, as observed in biological electron microscopy, the phase contrast gives the major contribution. The image can be considered as a superposition of a high-resolution elastic image and a blurred inelastic image. Zero-loss filtering allows removing the background of inelastically scattered electrons, which considerably increases the contrast (energy filtering) (Grimm et. al 1997).

In the case of phase contrast the electron beam modulation is described with the phase contrast transfer function (CTF). It characterizes the effect of the instrument on the image formation and is independent of the particular specimen in question:

$$CTF(f) = -2 \cdot \sin\left(\frac{\pi}{2} \cdot (C_s \lambda^3 f^4 - 2\Delta z \lambda f^2)\right), \quad (1)$$

where  $C_s$  is the spherical aberration constant,  $\Delta z$  the defocus,  $\lambda$  the wavelength of the electron beam, and  $f$  the spatial frequency. A typical image of an object modulated by the CTF and the corresponding power spectrum describing the squared amplitudes as the function of the spatial frequencies  $f_x$  and  $f_y$  is presented in Fig. 1.

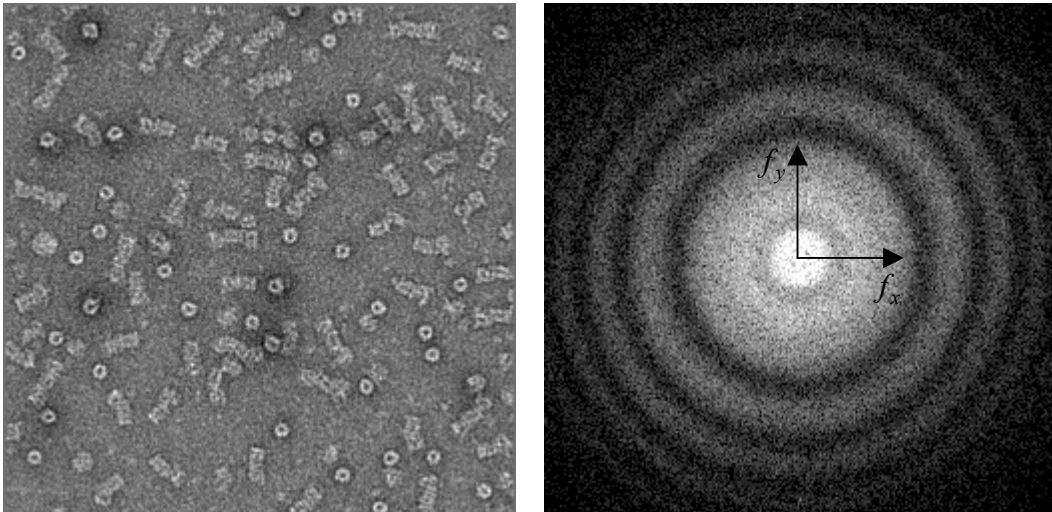


**Fig. 1.** Electron microscopic image of negative stained biological macromolecules (26S proteasome) and the corresponding power spectrum.

The electron beam is extracted from a field emission gun (FEG) in order to decrease the damping of the CTF at high spatial frequencies caused by spatial and temporal incoherence. The electrons are then accelerated with a tension that usually ranges between 100-300kV. The condenser system creates a parallel electron beam, which irradiates the specimen. The heart of the electron microscope is the objective lens whose properties determine the quality of the image (Fig. 2). The intermediate and projection lenses serve to magnify the primary image produced by the objective. The projection lens enlarges any defects of the objective lens, whereas defects in the projector itself are not subject to subsequent significant magnification and are thus not usually evident. The resulting image can be recorded by direct exposure of a photographic film or digitally via a fluorescent screen coupled by a fiber-optic plate to a CCD camera.

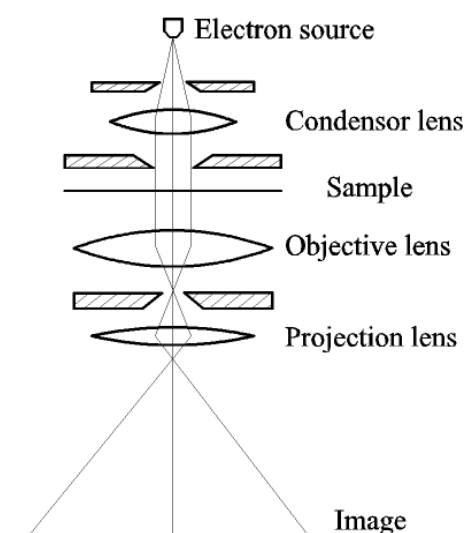


Fig. 2. Scheme of a transmission electron microscope

The primary goals at the frontier of experimental transmission electron microscopes are:

(a) To improve resolution: The higher the accelerating voltage the faster the electrons and the longer the mean free path inside the specimen. The use of a FEG makes the wavelength almost monochromatic (less chromatic aberration) and improves the phase contrast. In addition, the use of an energy filter serves to remove the inelastically scattered electrons (less blurring) whereas a decelerator improves the efficiency of the CCD camera.

(b) To preserve structural information and specimen consistency: The specimen preparation is very important. The specimen may be cooled to liquid-helium temperature in order to reduce the effects of the radiation damage and the electron dose has to be kept to a minimum.

### 1.3 Noise Model

The major noise contribution is associated with the illuminating beam (also called particle noise). The number of particles  $\lambda$  in a given area (e.g., pixel) follows a Poisson

distribution  $P(k, \lambda) = \frac{\lambda^k}{k!} \cdot e^{-\lambda}$ , with the variance  $\sigma_{Part}^2 \sim \lambda$ . Considering  $\lambda$  as the signal, its variance can be equivalently written  $\sigma_{Sign}^2 \sim \lambda^2$ , i. e., the signal-to-noise-ratio ( $SNR = \frac{\sigma_{Sign}^2}{\sigma_{Part}^2} = \lambda$ ) is proportional to  $\lambda$ . In the case of bright-field imaging of a weakly scattering objects the signal is given by  $\Delta\lambda = \lambda - E\{\lambda\}$ , where  $E\{\lambda\}$  is the expectation value of all particles illuminating the specimen. Assuming that  $\Delta\lambda \ll E\{\lambda\}$ , the noise becomes signal-independent and therefore the approximation of additive Gaussian noise is valid (Hegerl et. al 1976). Other noise sources, e.g. noise of the recording system, multiple scattering, etc., can then also be assumed as normally distributed.

For various imaging techniques the noise can be (possibly after an appropriate transformation, see also Donoho 1996) closely modeled as additive Gaussian and signal-independent. The signal reconstruction problem for this case is formulated in the following way: Let  $\mathbf{y}$  be the noisy observation of  $\mathbf{x}$ , degraded by the noise  $\mathbf{n}$ , such that

$$\mathbf{y} = \mathbf{A} \cdot \mathbf{x} + \mathbf{n}, \quad (2)$$

$\mathbf{A}$  represents a transformation matrix describing a linear operation applied on the object. The estimate  $\hat{\mathbf{x}}$  from  $\mathbf{y}$  has to be determined, such that the remaining noise in  $\hat{\mathbf{x}}$  is sufficiently low and  $\hat{\mathbf{x}}$  resembles  $\mathbf{x}$  sufficiently closely. Depending on the image processing task and the specimen under scrutiny the noise sources vary. Apart from the typical noise sources listed above, missing information as in the case of 3D electron microscopic reconstructions can introduce deterministic features in the image, which do not belong to the object. These features shall be removed from the  $\mathbf{y}$ , or at least shall not affect the reconstruction performance.

## 1.4 Specimen Preparation

Probably the most important step in recording good electron microscope images is a reproducible and stable specimen preparation. Apart from the electron microscope modalities a good specimen preparation in conjunction with adequate image processing methods allows for extraction of structural information. In the electron microscopy field several (different) preparation techniques are employed in order to stabilize and preserve the structural information of the biological sample and to improve the signal-to-noise ratio. The preparation techniques used for the specimen processed here can be distinguished into negatively stained samples and frozen hydrated samples.

The negative staining preparation is usually used for single particle analysis. A heavy metal solution, e.g. uranyl acetate is applied to the specimen, in order to fixate it and enhance the contrast. Even though this technique is fast, the resolution is limited, due to the granularity of the heavy metal used. Additionally structural changes (e.g. flattening) can appear.

Cryo-electron microscopy is more promising in terms of resolution. Here frozen hydrated biological samples are embedded in vitreous ice by plunging them into liquid ethane; i.e. the sample is kept in a near-to-native state and protected against radiation damage. However the contrast of these samples is very low.

## 1.5 Three-Dimensional Electron Tomographic Reconstruction

Three-Dimensional tomographic reconstruction is a method similar to the well known tomographic reconstruction in medical imaging (X-ray tomography, etc.). All these methods are based theoretically on the “central section theorem”, stating: The Fourier transform of the 2D-projection image corresponds to the central section through the 3D Fourier transform of the object, which is perpendicular to the projection direction (Radon 1917). This theorem can be used to perform a 3D reconstruction: The 2D Fourier transforms of the projections are derived and placed in the 3D Fourier domain, according to the corresponding angle. After interpolation and 3D inverse Fourier transformation, the reconstructed object appears in real space. In practice a different algorithm, namely filtered backprojection is mainly used for reconstruction in electron tomography due to its simplicity and general applicability (Koster et al. 1997). With this algorithm the recorded images are multiplied with a ramp filter in the Fourier domain, transformed back in the real space and inversely projected into the reconstructed volume.

The typical experimental approach in electron tomography is to tilt the specimen about an axis perpendicular to the electron beam and to record an image for each tilt view. Unfortunately, the specimen cannot be tilted over the full angular range from  $-90$  to  $+90$  degrees, because the specimen holder masks the object at high tilt angles. Additionally, the total electron dose has to be kept below a critical limit in order to avoid excessive radiation damage. Therefore the number of projection views has to be limited and the images suffer from an extremely low signal-to-noise ratio. Image shifts resulting from mechanical inaccuracies of the tilt stage and from specimen drift require an alignment of the projection images with respect to a common origin, a process also prone to errors. As a consequence of these effects, the interpretation of volumetric data obtained by electron tomography is severely aggravated by artifacts and a noisy appearance. Of the artifacts, those arising from the limited tilt range are easy to understand in the Fourier domain (“missing wedge”) and, in real space, may be described by a point spread function expressing an anisotropic resolution.



## Chapter 2

# Nonlinear Anisotropic Diffusion

Transmission electron microscopy is used to investigate the structural organization of biological objects (e.g. macromolecular assemblies or organelles) at a resolution in the nanometer range. By means of techniques similar to medical computer tomography, it is possible to reconstruct the 3D density of the specimen and to reveal the 3D structure of the biological object (Koster et. al 1997). Although electron microscopes are able to image biological objects with a resolution down to 0.3nm, the structural information is not directly accessible since most of the signal is buried in noise (SNR<0dB). The standard method for denoising is correlation averaging, where many thousand identical particles are averaged in order to reveal structural information with a resolution down to 0.8nm. In the case of pleomorphic objects (such as cells or organelles) averaging is not possible, due to the uniqueness of the structure, nevertheless denoising exigently necessary. Particularly with regard to the three-dimensionality of the observed objects, denoising plays an essential role, since the human eye is not able to extract the same amount of information (by interpolation, lowpass filtering, classification, etc.) as in the 2D case. An interpretation of the 3D images using surface- and volume-rendering techniques is difficult due to the noise sensitivity of rendering algorithms. A denoising algorithm suitable for such applications must be able to preserve as much signal as possible while reducing the noise sufficiently.

A multidimensional implementation of a powerful signal reconstruction method, namely nonlinear anisotropic diffusion is presented. This technique exploits the scale space representation of the local signal and performs noise reduction on the basis of global signal properties. The proposed method is applied for noise reduction on 3D electron microscopic data and medical computed X-ray tomography (electron beam CT) for fast imaging of human organs. Qualitative and quantitative measures are used for assessing the spectral signal reconstruction performance on synthetic and biomedical volumetric images, revealing the real potential of the method. The superior signal reconstruction performance of the novel hybrid diffusion technique in the field of electron microscopy over conventional noise reduction methods (e.g. Gaussian and median filtering) as well as invariant wavelet filtering is proven.

## 2.1 Diffusion Types

### 2.1.1 Linear Diffusion

The evolution of an image  $I = I(\mathbf{x}, t)$  processed by a diffusion technique can be described with the following partial differential equation (PDE):

$$I_t = \text{div}(\mathbf{G} \cdot \nabla I), \quad (3)$$

where  $\nabla I$  is the gradient with respect to the coordinate vector  $\mathbf{x}$  in a space of arbitrary dimension  $N$ ,  $I_t$  denotes the derivative related to the processing time  $t$ , and  $\mathbf{G}$  is a tensor called diffusivity, designed to steer the direction of the diffusion process. The diffusivity is a quadratic, positive semidefinite matrix, with dimension  $N$ . In the simplest case,  $\mathbf{G}$  is a diagonal with constant elements  $g$ . The resulting linear isotropic diffusion corresponds to Gaussian real space filtering with a variance that increases with time  $\sigma^2 = 2 \cdot g \cdot t$ .

### 2.1.2 Nonlinear Isotropic Diffusion

In order to improve on the linear isotropic diffusion, especially with respect to edge preservation, Perona and Malik used a monotonically decreasing function  $g(I)$  instead of a constant  $g$ , such that the diffusion flux was minimized over edges (Perona and Malik 1988). This nonlinear, yet isotropic process results in intraregional smoothing between well-preserved edges and avoids the overall blurring that is typical for linear diffusion. They solved a PDE of the form:

$$I_t = \text{div}(g(\nabla I) \nabla I) \quad (4)$$

with a scalar diffusivity:

$$g(\nabla I) = \frac{1}{1 + |\nabla I|^2 / \kappa^2}, \quad (5)$$

where  $\kappa$  is user defined and contrast dependent.

Apart from discretization problems, this approach is still limited by the isotropy of the equation: Only the intensity of diffusion flux can be controlled but not its direction. This results in a preservation of noise along the edges, a highly undesirable property.

### 2.1.3 Nonlinear Anisotropic Diffusion

In the nonlinear anisotropic case the diffusivity  $\mathbf{G}$  has nondiagonal elements different from zero. The direction information is gained from the structure tensor  $\mathbf{J}_0 = \nabla I \cdot \nabla I^T$  or from its average over a small 3D image  $\mathbf{J}_{\sigma_T} = \mathbf{J}_0 * \mathbf{K}_{\sigma_T}$ , where  $\mathbf{K}_{\sigma_T}$  is a Gaussian filter with variance  $\sigma_T$ . The eigenvectors  $\mathbf{v}_i$  of  $\mathbf{J}$  and the corresponding eigenvalues  $\mu_i$

characterize the local structural features of the image  $I$  within a neighborhood of size  $O(\sigma_T)$ . Each eigenvalue  $\mu_i$  reflects the gray level variance in the direction of the eigenvector  $\mathbf{v}_i$ . The first eigenvector  $\mathbf{v}_1$  corresponding to the eigenvalue  $\mu_1$  is a local average over the directions of maximum variance. The eigenvalues are non-negative since the structure tensor is positive semidefinite. In the case of a non-averaged structure tensor ( $\sigma = 0$ ), the relations  $\mathbf{v}_1 = \nabla I / |\nabla I|$  and  $\mu_1 = |\nabla I|^2$  hold, while all other eigenvalues are equal to zero. The structural information expressed in the eigenvalues  $\mu_i$  and eigenvectors  $\mathbf{v}_i$  is used to define the diffusivity tensor.

$$\mathbf{G} = [\mathbf{v}_1 \quad \mathbf{v}_2 \quad \mathbf{v}_3] \cdot \begin{bmatrix} \lambda_1(\mu_1, \mu_2, \mu_3) & 0 & 0 \\ 0 & \lambda_2(\mu_1, \mu_2, \mu_3) & 0 \\ 0 & 0 & \lambda_3(\mu_1, \mu_2, \mu_3) \end{bmatrix} \cdot [\mathbf{v}_1 \quad \mathbf{v}_2 \quad \mathbf{v}_3]^T \quad (6)$$

The parameters  $\lambda_i$  steer the diffusion flux in the directions of  $\mathbf{v}_i$ .

The major problem is how to define the diffusion tensor such that the overall isotropy of the process is preserved. For instance, the question arises how to choose the  $\lambda_i$  values such that a *line-feature* being processed with a 1D diffusion flux and a *surface-feature* with a 2D diffusion flux. The application of the wrong flux would produce artifacts in the former case, such as a unidirectional broadening of the line (e.g., sword-like structures) and in latter case the shape of the surface would remain unrevealed. A solution to this problem could be given with the second eigenvalue  $\mu_2$ , which is capable of detecting the kind of the local geometric feature. Unfortunately in the case of very noisy data this local information is very uncertain. Therefore, only a 1D diffusion flux ( $\lambda_1 = \lambda_2$ ) is applied.

### 2.1.3.1 Coherence and Edge Enhancing Diffusion

In his 2D setup, Weickert has proposed two different realizations of diffusion processes, namely coherence enhancing diffusion (CED) and edge enhancing diffusion (EED). Extending the method from 2D to 3D the parameters are chosen such that:

$$\lambda_1 = \lambda_2 = \alpha \text{ and } \lambda_3 = \alpha + (1 - \alpha) \cdot \exp\left(-C / (\mu_1 - \mu_3)^2\right) \quad (7)$$

with user-defined global parameters  $\alpha$  and  $C$  (Weickert 1999). Usually a small value has to be assigned to  $\alpha$ . For  $\alpha \rightarrow 1$  the approach converges to Gaussian filtering, realized perfectly for  $\alpha = 1$ . The amount of flux in the orientation perpendicular to the gradient is determined by the difference  $\mu_1 - \mu_3$ . This difference is large for flowlike structures (e.g., parallel lines running in the same direction as in a fingerprint) due to a high variance in one direction and consequently such structures are extremely enhanced. Areas containing only noise are characterized by  $\mu_1 \approx \mu_2 \approx \mu_3$  and therefore remain unmodified. With CED the diffusion flux can be steered in the preferred local orientation and can thus, as an example, be used to connect interrupted lines.

The second approach called edge enhancing diffusion (EED) is based on the eigenvectors of the non-averaged structure tensor  $\mathbf{J}_0$  and uses

$$\lambda_1 = \lambda_2 = \frac{1}{1 + \mu_1/\kappa^2} \text{ and } \lambda_3 = 1 \text{ (see eq. 5).} \quad (8)$$

Due to  $\mu_1 = |\nabla I|^2$ , this approach is equivalent to the method proposed by Perona and Malik. Therefore, edges are preserved and smoothing the areas between these edges reduces the noise.

### 2.1.3.2 Hybrid Diffusion

The 3D implementation of anisotropic diffusion of the present here is a hybrid approach that combines the advantages of EED and CED according to the following strategy. Since the difference  $\mu_1 - \mu_3$  reflects the local relation between structure and noise it can be used as a switch: EED is applied when this value is smaller than a suitably chosen threshold parameter, and CED otherwise. Both processes take place simultaneously within one iteration step, depending on the local threshold parameter. If the build-up of a specific edge takes more iterations, the other edges are going to be preserved and enhanced, so that no signal degradation takes place. A useful threshold parameter can be derived *ad-hoc* from the variance, calculated over a sub-3D-image of  $I$  that only contains noise. It is possible to verify the appropriate choice of the sub-3D-image by lowpass filtering or even by visual control of the images used for the 3D reconstruction. It is also important to notice that the hybrid model retains the properties of the diffusion processes.

For the discretization of the model central differences are utilized. The additive operator splitting (AOS) (Weickert 1998) schemes definitely showed a superior performance to the standard iterative methods, but in order to switch between the different diffusion types, the simulations were performed with the simple explicit Euler method. In order to preserve small structures, with a size of only a few pixels, the gradient approximation proposed by Sethian (1998) is used. It shows a better performance than the standard central-difference gradient approximation.

### 2.1.4 Properties of the Diffusion Processes

Diffusion processes have many attractive properties, which makes the method very reliable, even though it is nonlinear and anisotropic. Three important features are pointed out: a) The process converges to a constant gray value image and the mean  $m$  is preserved. b) The MiniMax principle is fulfilled and consequently new extremes are not created. c) With  $r(s)$  as a convex function of the solution  $s$  of the diffusion process, the Lyapunov functional  $\Phi = \int r(s) ds$  decreases. Popular convex functions are the energy

$r(s) = s^2$ , variance  $r(s) = (s - m)^2$  and  $r(s) = s \cdot \log(s)$ . For  $s > 0$  the function  $r(s) = -s \cdot \log(s)$  can be interpreted as the entropy. Since anisotropic diffusion filters increase the entropy, the original image is embedded into a family of subsequently likelier versions of it, which contain less information. Moreover, for  $t \rightarrow \infty$ , the process reaches the state with the lowest possible information, namely a constant image. From the previous statements, becomes clear that in spite of contrast enhancing properties, nonlinear anisotropic diffusion simplifies the original image in a steady way.

## 2.2 Comparison of Different Diffusion Methods

### 2.2.1 2D Synthetic Data

In order to illustrate the effects of different diffusion processes, they are applied on a 2D test-image (“Barbara” Fig. 3a), which was degraded by additive white noise (Fig. 3b). The example demonstrates how diffusion can be steered by an appropriate setting of parameters in the diffusivity matrix. On the basis of many test calculations using 2D and 3D synthetic data (see ch. 2.3.1), the hybrid diffusion approach turns out to be superior to conventional methods as well as other diffusion denoising methods and invariant wavelet filtering. This can be stated in a quantitative manner by assessing the similarity between the original noise-free signal and the denoised version of the degraded signal, e.g. on the basis of the mean square error or the cross correlation coefficient.

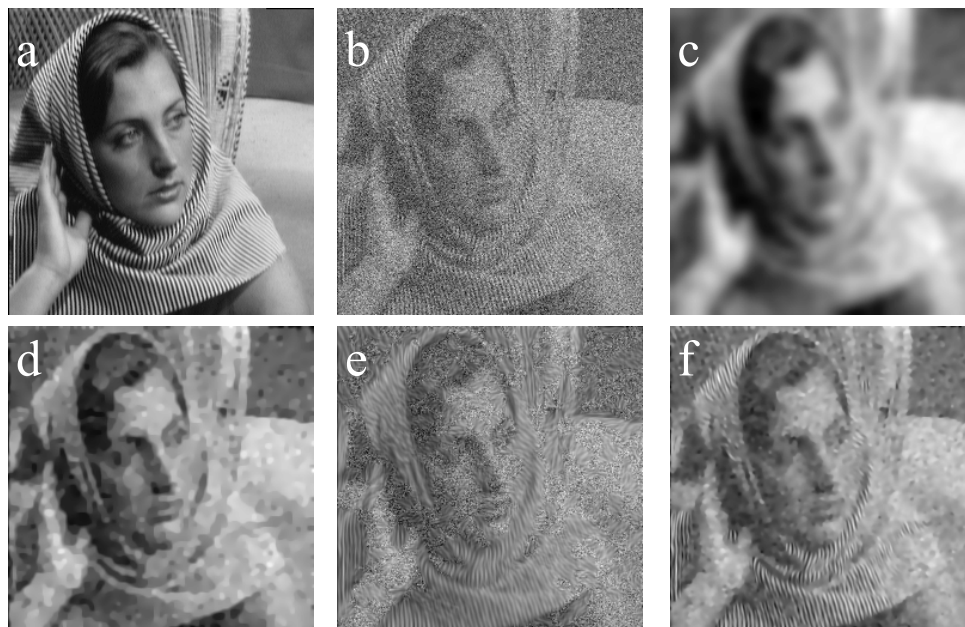


**Fig. 3.** Noise reduction based on different types of diffusion. (a) Original image of “Barbara”, (b) White Gaussian Noise degraded version (SNR=1), (c) Gaussian filtering (linear isotropic diffusion), (d) edge enhancing diffusion, (e) Coherence enhancing diffusion, (f) Hybrid diffusion.

The simulations with test images give an impression of how a method works and a feeling for the correct adjustment of the parameters. The application of linear diffusion

creates a blurred image. With edge enhancing diffusion the edges are better preserved, as the diffusion flux is smaller in places with large gradient. A “staircasing” effect is observed. Places with nearly the same gray value create a small plateau, which differs with a significant gradient from the environment. High frequencies are here better preserved, even though the line features on the clothes of “Barbara” are eliminated (Fig. 3d). In case of the coherence enhancing diffusion the line features are preserved and enhanced, but the rest of the image remains unchanged (Fig. 3e). The hybrid approach combines the advantages of the latter two methods (Fig. 3f). A significant noise reduction is achieved in the image with parallel preservation of high frequency features.

### 2.2.2 Pleomorphic Cellular Structures

In the following, the hybrid realization of nonlinear anisotropic diffusion is applied to real volumetric data as obtained by electron tomography. The first example for the applicability of the hybrid diffusion approach is a vesicle with actin filaments (Grimm et. al 1997). A comparison of the hybrid approach with the other diffusion methods on real data is made. The size of the longitudinal elongated vesicle is 100nm in diameter and the resolution of the reconstruction is approximately 7nm. The position, connectivity, and strength of the actin filaments, pictured as dark lines in Fig. 4, or as thin white fibers running parallel to the direction of the cylinder in Fig. 5, are the features of interest. The quality of representation of these features can also be used as a criterion for the judgement of the performance of the respective method. For this 3D image a comparison with standard techniques in image processing (e.g. low-pass and median filter) is also presented. In the case of low pass filtering the noise and the signal are simultaneously degraded. Though producing a satisfactory smooth background, the filaments are thickened and interrupted. The isosurface representation appears corrupted due to a lack of information. Median filtering results in good edge preservation, but the noise reduction is not satisfactory. The results after application of either EED or CED confirm the properties described in the previous section. EED produces the typical staircase effects and imposes an artificial appearance in the 3D images. The connectivity of the filaments is not improved or even preserved. It shows a behavior basically opposite to CED. In this case no noise reduction has taken place, nevertheless the connectivity of the filaments is significantly improved. At last the result of the hybrid diffusion approach is presented. It combines an excellent noise reduction of the background with a clear representation of the filaments. In Fig. 4 and Fig. 5 the results of different types of filtering for the vesicle with actin filaments are illustrated in tomographic and isosurface representation.

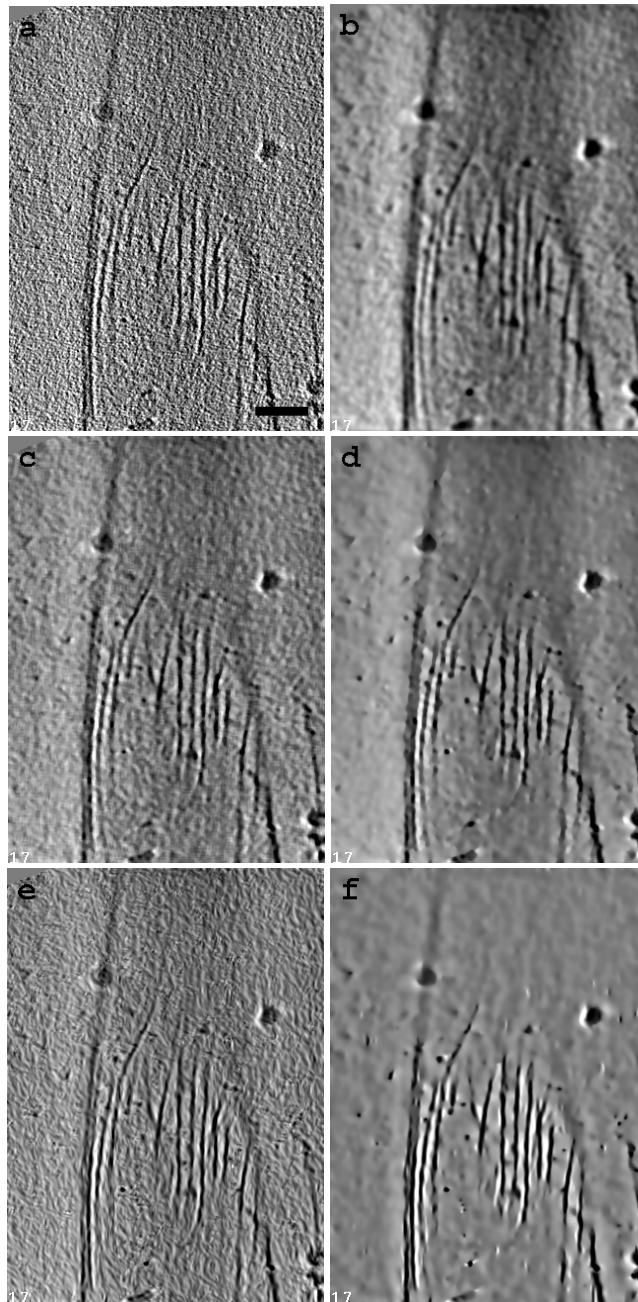


**Fig. 4.** Comparison of different filtration types of a x-y slice from an electron tomographic reconstructed 3D image of a vesicle with actin filaments. (a) slice from the original reconstruction, (b) Gaussian filter, (c) median filter, (d) EED, (e) CED and (f) hybrid EED/CED. Bar = 20nm.

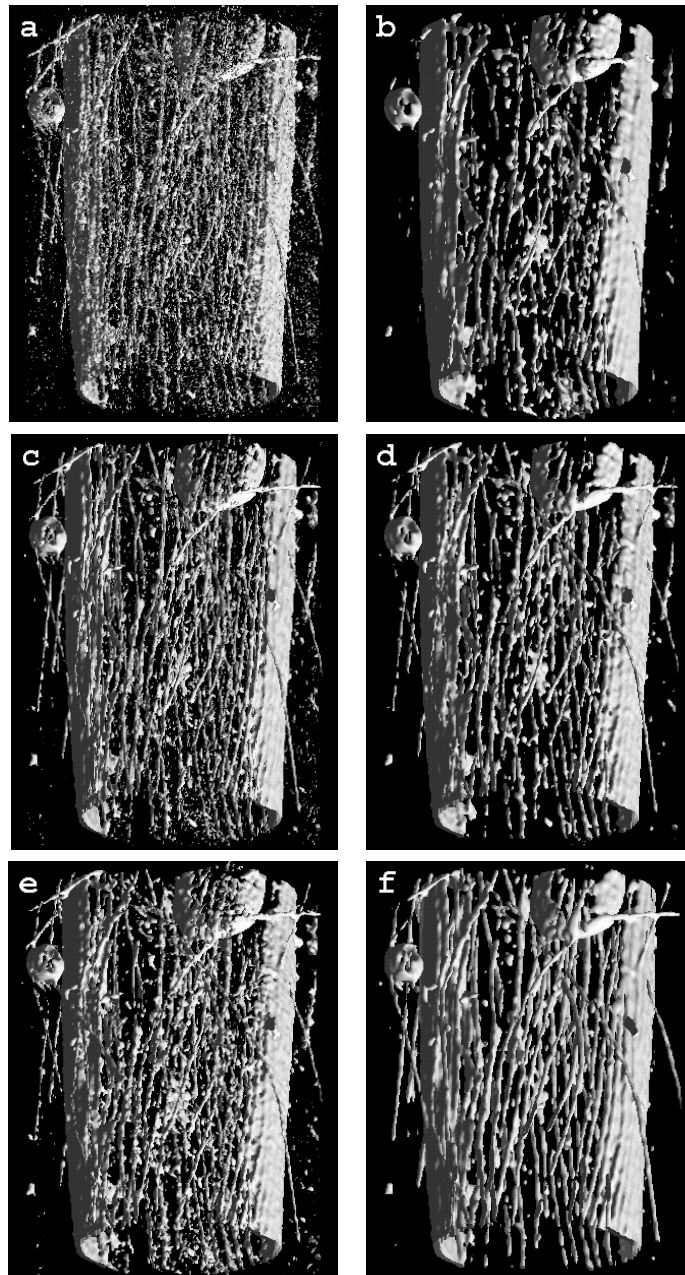


**Fig. 5.** Isosurface representation of a vesicle with actin filaments (3D image 256\*256\*128 Voxels). The order of the representation is the same as in Fig. 4.

In order to visualize the irregular three-dimensional structure of chromatin, a highly organized complex of DNA and proteins (mainly histons) (Horowitz et al., 1998) chromatin fibers were investigated by electron tomography. For this purpose, long chromatin fibers were isolated from erythrocytes of the amphibian *N. maculosus*, and tilt

series of this specimen were recorded within an angular range of  $-60^\circ$  to  $+60^\circ$  at  $5^\circ$  increment. The 3D reconstruction was performed with weighted backprojection.

Due to the extremely low electron dose that had to be used in acquiring the tomograms as well as the low contrast produced by ice-embedded specimens, the resulting SNR is exceedingly low (below 0.1). The visualization of the resulting 3D maps by isosurface representation or volume rendering is severely hindered due to the high noise level. In this case the denoised data representation outperforms even the perceptual ability of the human visual system. For “real world” data the performance of a denoising method can not be quantified in general. Therefore the visual inspection of the original as well as of the processed data and verification of the expected result are the most common criteria for judging the denoising results. Here, the 3D arrangement (zigzag path) of the DNA and nucleosomes of the reconstructed chromatin needs to be visualized.

In this data set a comparison with lowpass filtering and median filtering is performed. As shown in Fig. 6, hybrid diffusion outperforms clearly both. It achieves a considerable reduction of noise combined with sufficient signal preservation. Studying the structure of the fiber on the basis of a simple isosurface representation has become feasible (Fig. 7).

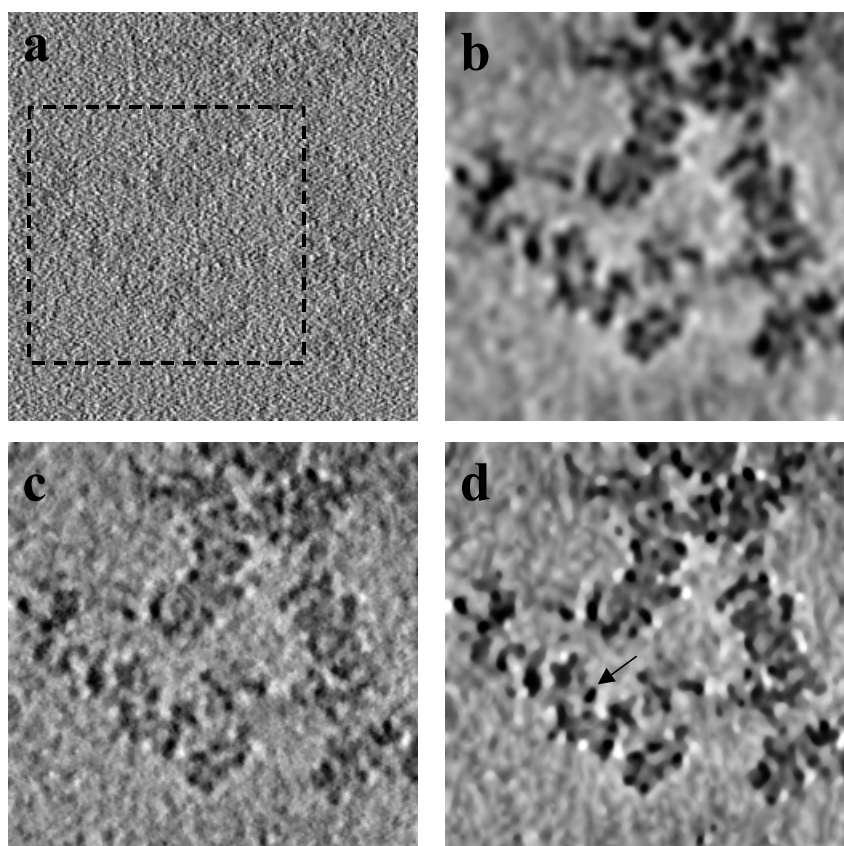


**Fig. 6.** Noise reduction methods applied to a 3D map of chromatin as obtained by electron tomography. (a) Central xy-slice through the 3D reconstruction and its processed versions using. Dotted box indicates the sub-3D image used for the volume rendering presentation (Fig. 7) (b) Gaussian filtering, (c) median filtering and (d) hybrid diffusion. Arrow points to a single nucleosome, which could be identified.

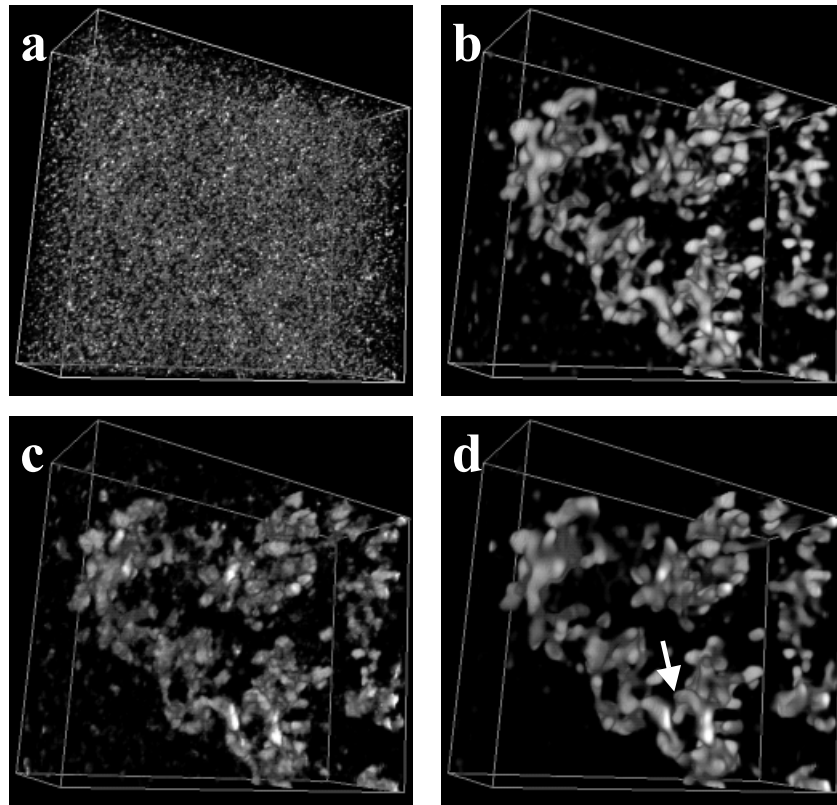


**Fig. 7.** Volume rendering representation of 3D tomographic reconstruction of chromatin: Order as in Fig. 6. Arrow points to zig-zag structure of the chromatin conformation.

### 2.2.2.1 Path Tracing with Neural Network for Revealing the Backbone of Chromatin

The hybrid diffusion technique improves the SNR of the tilt series significantly, although the real path of the DNA strand in space remains, with some exceptions (Fig. 7 arrow), not revealed. In order to propose a possible path of the DNA in space a self-organized neural network has been used.

Neural networks (NN) have been proven as very powerful tools, with applications in various fields of science and industry (Haykin 1994). The principle of a NN is the adaptive primary elements, which receive signals from an event space, and signal representations are automatically mapped onto a set of output responses in such a way that the responses acquire the same topological order as the primary events. Neural networks are characterized from arbitrary geometry, which is applied from the neighborhood function between the different neurons. Assuming the 1D path of the strand in space, 465 processing units (neurons) have been used, coupled with an internal 1D neighborhood, for the self-organizing process.

The input set (training set) of the neural network was the set of Cartesian coordinates  $x$  with a gray value  $-I(x)$  higher than a threshold (very robust, reduces the processing time) of the denoised tilt series. Due to the low SNR of the original reconstruction and the requirement of correct classification of all nucleosomes (produce higher contrast) the

gray value  $-I(\mathbf{x})$  is used like a weighting value, determining the mass of modification of the neuron position  $\mathbf{w}_i$ . Additionally with the use of the gray values the correct classification of the nucleosomes (higher contrast) is facilitated. A short-range lateral feedback between neighboring units has been implemented in the NN, as a form of a 1D Gaussian neighborhood  $G$  with the following influence function:

$$g(i, k) = \exp\left(-\frac{(i-k)^2}{\sigma^2}\right),$$

where  $i$  is the index of the „winner neuron“, which is defined as the neuron with the minimal distance  $|\mathbf{x}(k) - \mathbf{w}_i(k)|$  to the input vector. The learning algorithm then has the following form:

$$\mathbf{w}_k(n+1) = \mathbf{w}_k(n) + g(i, k) \cdot lr(n) \cdot I(\mathbf{x}) \cdot (\mathbf{x} - \mathbf{w}_k(n)), \quad (7)$$

Where  $lr(n)$  is the learning rate, which is reduced sequentially during the process.

The result from revealing the path of the strand is presented in Fig. 8. The NN has converged to the position presented above after starting from random position in 3D space. The convergence result is reproducible and independent from the start positions of the neurons. The fit of the NN is optimal in the Chromatin isosurface. The path of the NN Fig. 8 just presents one possible path of the strand in space. The revealing of the correct path is aggravated by the missing wedge and the resulting elongation in z-direction and in particular by the low SNR. The NN was unable to approximate a possible path of the strand in the unfiltered reconstruction.

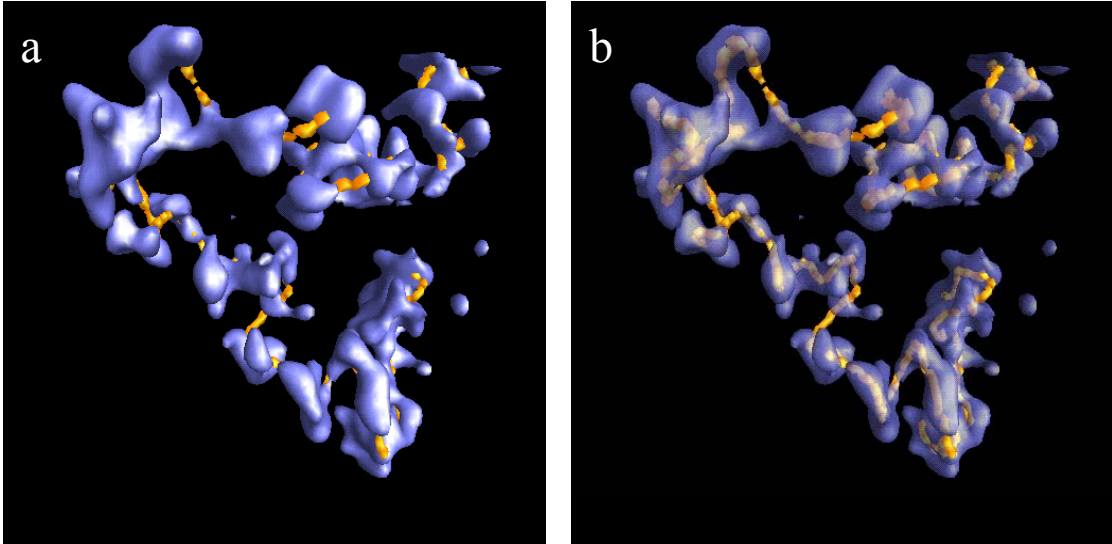


**Fig. 8.** Perspective view of the chromatin isosurface (blue) classified by a neural network (gold). (a) Nontransparent isosurface in order to present the gaps bridged by the NN. (b) Transparent isosurface with NN. Fitting of NN in the isosurface.

## 2.3 Comparison of the Hybrid Diffusion Approach with Invariant Wavelet Transform Filtering

Invariant wavelet transform filtering is one of the most powerful techniques for signal reconstruction (Stoschek & Hegerl 1997). A comparison of wavelet transform filtering with nonlinear anisotropic diffusion is desired, in order to find the appropriate technique applicable in the field of electron microscopy. The techniques are principally different, as wavelet filtering is a transform-based method and nonlinear diffusion a real-space one. Nevertheless, they share the property of using *multiscale representations* to allow for local signal recognition on the basis of global signal properties (Witkin 1993). Detailed information on the wavelet technique can be found in Strang 1996.

### 2.3.1 Synthetic Data

In order to evaluate the signal reconstruction performance of invariant wavelet denoising and nonlinear anisotropic diffusion, both methods are applied on multidimensional data. For a thorough comparison a synthetic 3D data set of size 256x256x128 pixels is generated. It contains a mix of isotropic smooth and anisotropic line-type signals simulating typical biomedical data. The test data consists of a Gaussian blob, a hollow tube, a star-like structure, and a quasi-periodic structure with oscillating concentric waves starting at a common origin in space. The signal completely fills the frequency space. To simulate realistic noise conditions white and colored Gaussian noise is added to the data with a SNR=0.5 and SNR=1, respectively, i. e., the actual signal gets substantially degraded (see Fig. 9 a-c). The colored noise is synthesized by lowpass filtering, the white noise using a low-pass filter with a cut-off frequency  $f_{cut-off} = 0.25 \cdot f_n$ , where  $f_n$  denotes the Nyquist frequency.

Data	NR	MSE	CCC
White noise	2	4	0.19
LP	0.15	0.25	0.737
MF	0.23	0.27	0.719
WF	0.15	0.21	0.782
NAD	0.097	0.2	0.78
Colored noise	2.5	9.55	0.474
LP	0.57	3.26	0.725
MF	0.67	3.51	0.726
WF	0.37	2.52	0.759
NAD	0.49	3.26	0.759

**Table 1:** A quantitative comparison of following denoising methods: Lowpass filtering (LP), median filtering (MF), wavelet filtering (WF) and nonlinear anisotropic diffusion (NAD). For measuring the performance three criteria are used: The noise reduction (NR) as the ratio of the noise in the noisy and denoised data, mean squared error (MSE) as the absolute deviation and cross correlation coefficient (CCC) as the relative similarity for the data in Fig. 9.

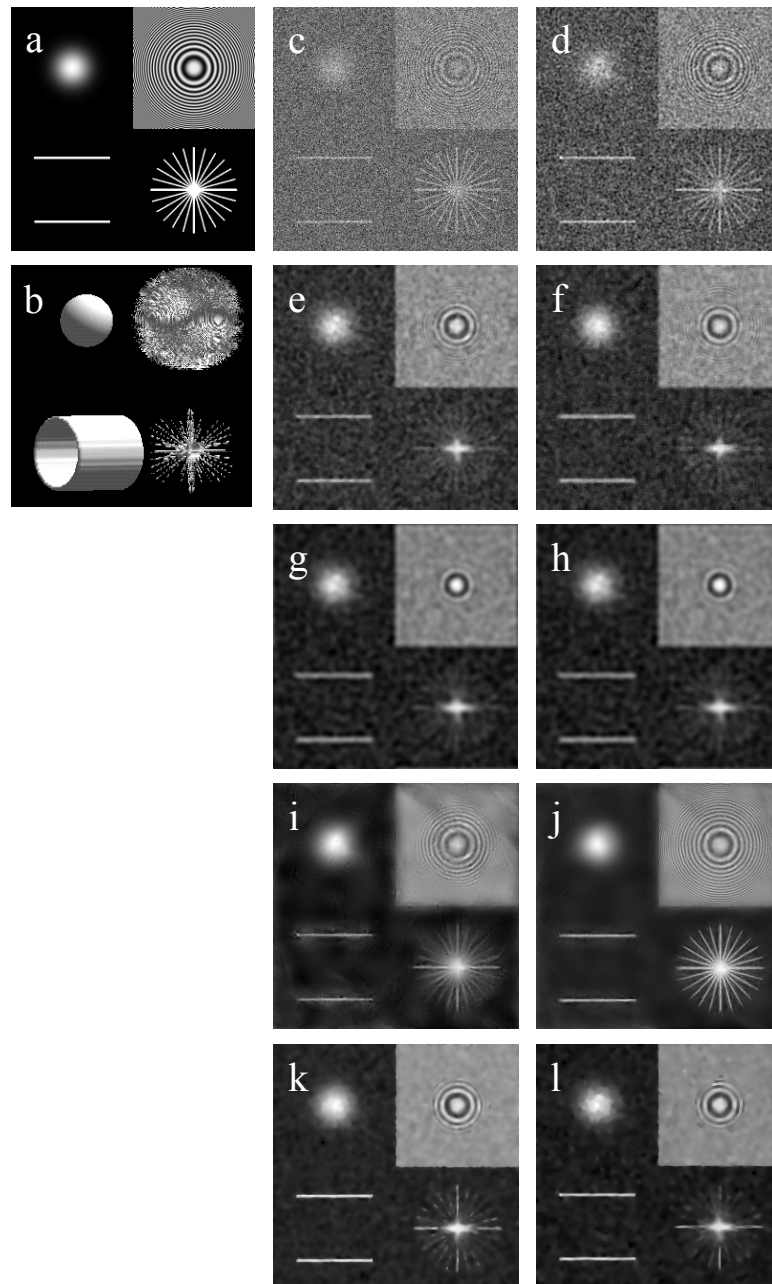


**Fig. 9.** Comparison of different noise reduction methods using synthetic volumetric data corrupted by noise. In the central column the white noise (c, e, g, i, k) is referred, in the right column colored noise (d, f, h, j, l). (a) central x-y section through the original 3D image, (b) isosurface representation of the whole 3D image (c) data corrupted with additive white Gaussian noise (SNR=0.5), (d) data corrupted with colored noise (SNR=0.5), (e-l) denoised versions of the central section processed by (e, f) lowpass filter, (g, h) median filter, (i, j) invariant wavelet filtering, (k, l) anisotropic diffusion.

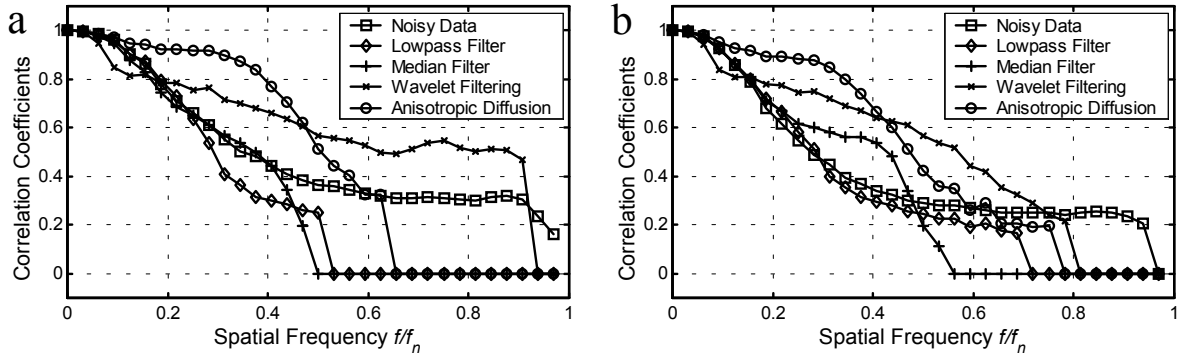


**Fig. 10.** Signal-to-Noise ratio improvement assessed by Fourier shell correlation in the frequency domain using synthetic data degraded by additive white noise (SNR=0.5) (a) and colored noise (SNR=1) (b). The curves present the cross correlation coefficients calculated between original and processed data depicted in Fig. 9.

For the experiments the exact knowledge about the noise parameters as provided in this synthetic environment is not used, nor the exact spectral signal-noise relationship in the data. Instead, a *blind denoising* of the data is attempted with the only prior knowledge about the noise to be additive and signal-independent. Thus a real-world noise reduction task is simulated as closely as possible. A quantitative comparison is provided in Table 1 and a qualitative comparison of different noise reduction methods in Fig. 10. For this and all the following experiments Daubechies-type wavelet basis functions are utilized and  $n-4$  levels of downsampling with  $n = \log_2 N$ , where  $N$  is the size of the dyadic signal along one dimension. With respect to computational costs the invariant wavelet filtering is performed here as a pseudo-3D scheme by applying the filtering to consecutive 2D slices through the 3D image.

Comparing the visual quality of the denoising with the measured values an inconsistent interpretation of the results is obtained. Both wavelet filtering and anisotropic diffusion outperform median and lowpass filter, as demonstrated in Fig. 9 and by analysis of the numerical values of noise reduction, mean squared error, and cross correlation coefficient (Table 1). However, when comparing wavelet filtering and anisotropic diffusion, the visual quality deviates significantly from what is measured. Especially in the case of colored noise, wavelet filtering outperforms all other methods. These deviations are attribute to the fact that relatively “simple” similarity measures (such as MSE or CCC) are largely determined by the power of low frequency components of the images, and can thus hardly lead to a conclusion of how well high-frequency fine details are reproduced. However, a sufficient preservation of fine detail largely defines the visual impression and is of great importance in various imaging tasks. A more advanced statistical similarity measure is therefore used that is intended to compare the similarity of two statistically independent sets. The Fourier shell correlation (FSC) compares two scenes  $i, j$  by the similarity of their correlation coefficients in rings or shells in the Fourier domain (Saxton et. al 1982). This measure is aimed at deriving a score for similarity that is independent of the sampling density at each spatial frequency. The FSC is defined as:

$$FSC(f) = \frac{\sum_{f' \in [f, f+\Delta f]} F_i F_j^*}{\sqrt{\sum_{f' \in [f, f+\Delta f]} |F_i|^2 \sum_{f' \in [f, f+\Delta f]} |F_j|^2}}, \quad (9)$$

where  $f$  denotes the spatial frequency and  $\Delta f$  the thickness of the shell.  $F_i(f')$  and  $F_j(f')$  are the complex Fourier coefficients of the two images ( $i, j$ ) in Fourier space and  $*$  denotes the complex conjugate.

In the following the relationship of the correlation coefficient with the SNR is derived. Assuming two images exhibiting the same signal degraded by additive noise, the cross-correlation coefficient CCC can be written as:

$$CCC = \frac{E\{(x+n_i)(x+n_j)\}}{\sqrt{E\{(x+n_i)^2\}}\sqrt{E\{(x+n_j)^2\}}} = \frac{\sigma_x^2}{\sqrt{(\sigma_x^2 + \sigma_{n_i}^2) \cdot (\sigma_x^2 + \sigma_{n_j}^2)}} = \frac{\frac{\sigma_x^2}{\sigma_n^2}}{\frac{\sigma_x^2}{\sigma_n^2} + 1} = \frac{SNR}{SNR + 1} \quad (10)$$

$E$  denotes the expectation value and  $\sigma_k$  the variance of the respective signal  $k$  ( $x$  represents the signal and  $n$  the noise). Therefore it is assumed that the noise has the same statistical properties in both compared realizations  $E\{n_i^2\} = E\{n_j^2\} = \sigma_n^2$  and are statistically independent  $E\{n_i \cdot n_j\} = E\{n_i\} \cdot E\{n_j\}$ . Equation 10 shows that an improvement of the correlation coefficient is equivalent to increasing the SNR.

The results of this comparison are shown in Figs. 10a and 10b and can be summarized as follows:

- (i) Invariant wavelet filtering and anisotropic diffusion clearly outperform median and lowpass filtering.
- (ii) Anisotropic diffusion exhibits an excellent performance at lower frequencies, achieving a considerable SNR improvement. However, due to the low pass characteristic of the diffusion and the discretization stencil, higher frequency components of the signal ( $> 0.5 \cdot f_n$ , where  $f_n = 0.5 \cdot f_a$  is the Nyquist frequency and  $f_a$  the sampling frequency) are irreversibly degraded.
- (iii) Invariant wavelet filtering is best in preserving signal in a frequency range upon  $0.5 \cdot f_n$ .
- (iv) The above statements i and ii hold for both white and colored noise.
- (v) Using other synthetic data (not shown here) the FSC curves corroborate this results.

## 2.3.2 Three-Dimensional Biological and Medical Data

### 2.3.2.1 Statistical Comparison using Redundant Data

Directly measuring of the performance of denoising methods on real-world data is not possible, because the true signal is unknown. Therefore an indirect method to obtain

quantitative comparisons is utilized. A certain class of biological specimens can be identically reproduced (such as specific macromolecular assemblies). In order to reveal the structural information of the specimen, a noise reduction procedure based on averaging is used. Instead of referring to a single instance of the specimen, a high number of identical copies of it (up to several thousand) are recorded. Averaging over multiple instances (after registering them into a common coordinate system) reveals the structural information (Saxton 1982). Each individual instance is considered as a single realization of the same statistical process. Therefore, adding  $n$  equivalent signals increases the SNR by a factor of  $\sqrt{n}$  when assuming additive signal-independent noise. The averaging technique can be considered as an ideal artifact-free noise reduction method. However, the averaging method is not applicable to unique structures (e.g., cells). Nevertheless, reproducible structures in conjunction with averaging can be used in order to evaluate the performance of the denoising methods for non-reproducible specimens. In order to compare different denoising techniques, 500 noisy but structurally identical 3D objects have been processed with low-pass and median filtering, wavelet denoising, and nonlinear anisotropic diffusion. Fig. 11 shows xy-slices through a 3D reconstructed single particle. The FSC coefficients of two statistically independent ensemble averages, containing 250 particles each, are compared (Fig. 12). The results confirm the FSC curves of the artificial data. For low-frequency signal components ( $f/f_n < 0.35$ ) anisotropic diffusion outperforms all other denoising methods considering the amount of noise that is removed. Invariant wavelet filtering does not reach a similar amount of noise removal. Note that in this example the data are oversampled, i. e., no high frequency signal components exist for  $f/f_n > 0.5$ .

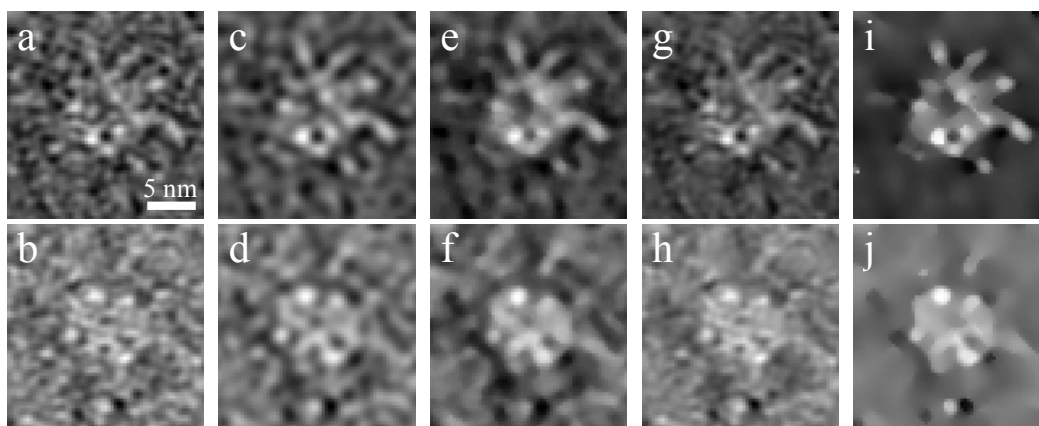


**Fig. 11.** Two exemplary xy-slices through the 3D reconstruction of a single macromolecule as obtained by electron tomography (the diameter of the particle is about 15 nm). Rows represent the slice processed by different noise reduction methods: Original 3D tomography image (a-b) and (c-j) denoised versions with (c-d) lowpass filter, with a cut-off frequency at  $0.25 \cdot f_n$ , (e-f) median filter, (g-h) invariant wavelet filtering, (i-j) nonlinear anisotropic diffusion.

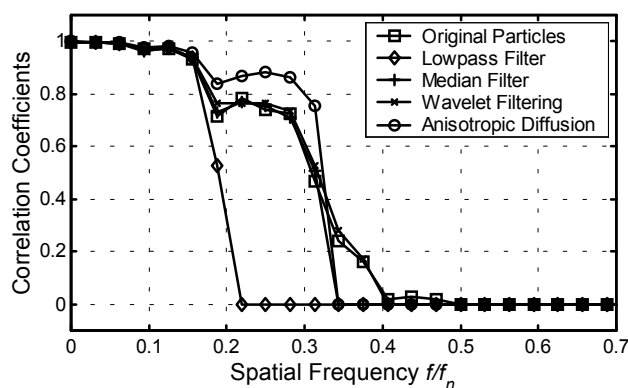


**Fig. 12.** Statistical comparison of different denoising techniques applied to single particle data as shown in Fig. 11. The Fourier shell correlation coefficients of two statistically independent ensembles, containing 250 particles each, are presented.

### 2.3.2.2 Noise Reduction on Unique Cellular Structures

After comparing the performance of nonlinear anisotropic diffusion with median and lowpass filter, here the performance of wavelet transform filtering (Fig. 13b) and nonlinear anisotropic diffusion (Fig. 13c) on highly noise-degraded data is exploited. An adequate example is the electron tomographic reconstruction of the ice-embedded chromatin (Horowitz et. al 1997).

In the original image the real structure can not be identified. The wavelet filtering manages to enhance the image quality, nevertheless several artifacts (or overpronunciation of small structures) make the result somehow artificial and unsatisfactory. The image created after processing with nonlinear anisotropic diffusion is excellent. Apart from the very smooth background, the edges of the chromatin have been preserved or even enhanced significantly.

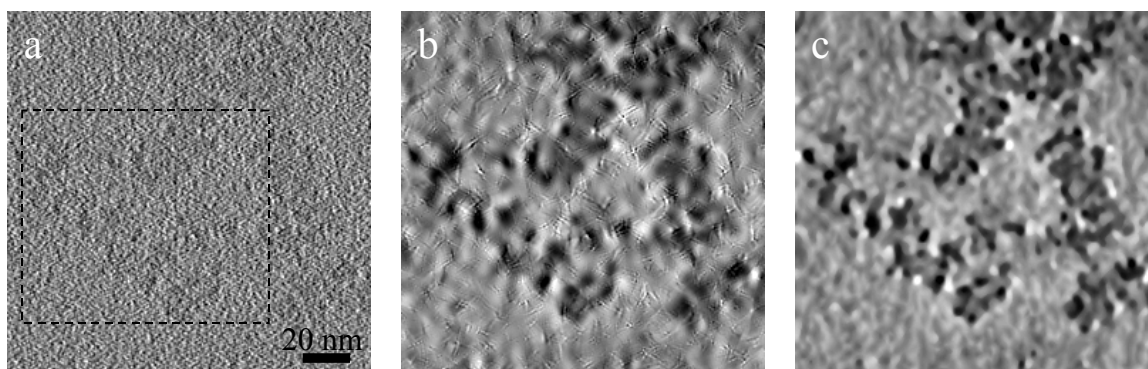


**Fig. 13.** Noise reduction applied on a 3D map of chromatin (a DNA-protein complex) as obtained by electron tomography. (a) Central xy-slice through the 3D reconstruction and its processed versions using (b) invariant wavelet filtering and (c) nonlinear anisotropic diffusion. The dotted box indicates the xy-boundaries of the volume rendering representation shown in Fig. 14.

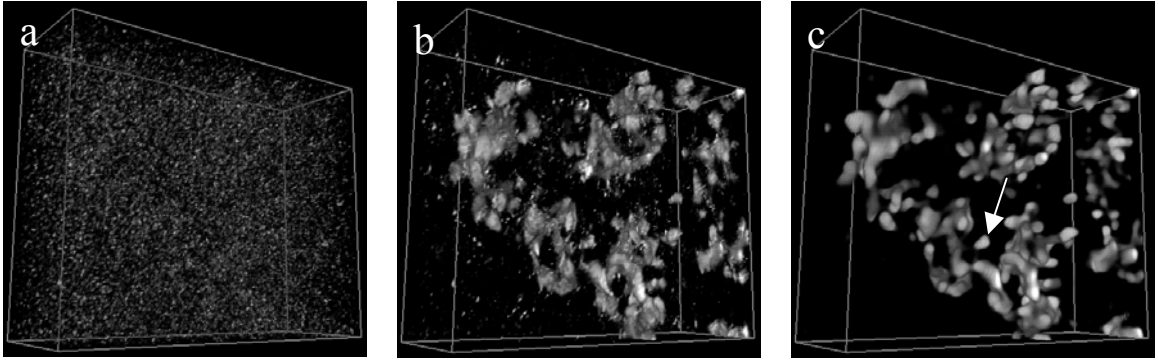


**Fig. 14.** Volume rendering representation of 3D tomographic reconstruction of chromatin: (a) original data, (b) invariant wavelet filtering and (c) nonlinear anisotropic diffusion. The volumes have been thresholded between  $m_{image} \pm 3.5 \cdot \sigma^2_{image}$ , where  $m_{image}$  and  $\sigma^2_{image}$  are the mean and variance of the image respectively. The arrow indicates the location of an individual nucleosome.

The volume rendering representations of the original and processed volume data are presented in Fig. 14. In the original data set it is very hard even to perceive a 3D structure (Fig. 14 a). The noise reduction using anisotropic diffusion is superior to wavelet filtering, as individual nucleosomes can unambiguously be identified. Additionally several artifacts occurring at the wavelet transform filtering are avoided. (Fig. 14 b, c).

A different example presents a 3D reconstructed *Pyrodictium abyssi* cell with an excellent SNR (Baumeister et. al. 1999). The quasi-periodic surface-layer of the cell consisting of regularly arranged proteins is clearly visible as textured structure (Fig. 15 a). After applying the discussed denoising techniques to the 3D reconstruction (Fig. 15 b, c) this regular pattern can be employed as a preservation criterion for the high frequency components. In Fig. 16 the line-plots through the 3D power spectra are compared that have been calculated from the textured area in the unprocessed reconstruction and the denoised 3D images, respectively. The results corroborate our previous findings on synthetic data. Anisotropic diffusion degrades signal components at frequencies  $f/f_n > 0.4$  due to its low pass characteristic. Therefore the second order reflex is nearly suppressed, where the wavelet transform maintains this reflex (Fig. 16). Thus wavelet denoising enhances the texture structures and enables the visualization of single units, i.e. single particles and small complexes. It can be concluded that wavelet denoising performs better than the anisotropic diffusion if the data contain strong high frequency signal components.

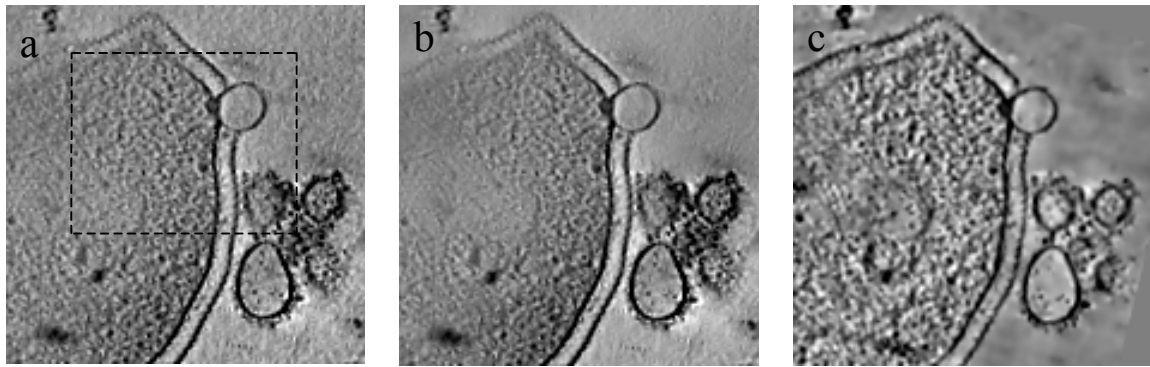


**Fig. 15.** Comparison of the denoising applied to a 3D reconstruction of a *Pyrodictium* cell; One  $xy$ -slice of (a) the original reconstruction, (b) denoised by Wavelet transform, (c) and by nonlinear anisotropic diffusion. The dotted box (a) indicates the  $xy$ -position of the area that is visualized by surface rendering in Fig. 17.

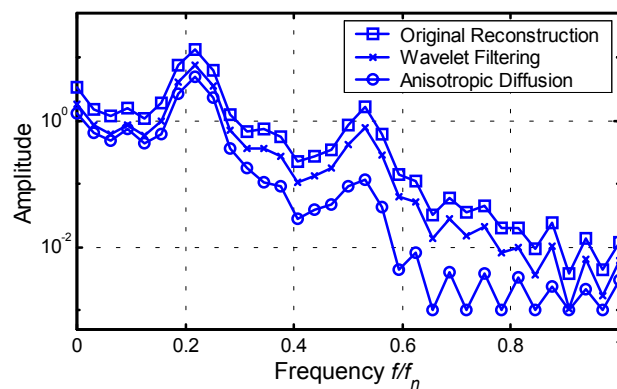


**Fig. 16.** Comparison of line-plots through the 3D power spectra (non-central) calculated from the textured area of the original and denoised *Pyrodictium* cell. The quotients of the second to the first order peaks are 0.1263, 0.1057, 0.0204, for the original, wavelet and anisotropic diffusion denoised respectively. It can be verified that both denoising methods imply an information loss, whereby the anisotropic diffusion dumps -in this case- the higher frequencies with a factor 5 higher than wavelet transform.

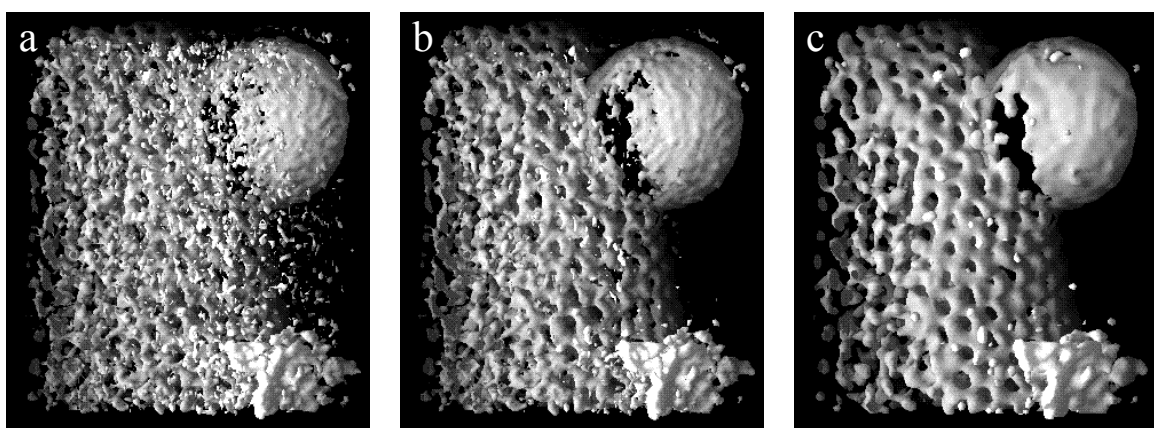


**Fig. 17.** Isosurface presentation of the *Pyrodictium abyssi* cell. The surface-layer of the cell appears as regular network structure. The cell interacts with a vesicle (top). Resolution of the reconstruction has been approximated to 8nm. (a) Isosurface from the original reconstruction and denoised versions with (b) Wavelet filtering, (c) Nonlinear anisotropic diffusion.

### 2.3.2.3 Electron Beam Computed Tomography

A new and promising development arising from classical X-ray tomography is “electron beam computed tomography”. It is the fast alternative to computed X-ray tomography (CT) in medical imaging. A full 3D data set can be recorded in 50-100 msec, which allows for time-sensitive investigations, such as examination of a heart with very little motion artifacts (Wang et. al 1996). Therefore, this new imaging technique is used to detect calcifications of blood vessels (Bielak et. al 1994), to extract the course of the coronary arteries, or to analyze walls and masses in the heart (Aschenbach et. al 1996). Other researchers want to use it for microtherapy using minimally invasive instruments guided by this imaging. However, in comparison to standard or helical CT data the SNR is considerably decreased, which prevents the application of automatic segmentation techniques for extraction of anatomical contours. The main source of noise in EBCT data is connected to the photon statistics of the x-rays. At the detector of the EBCT this noise can be approximated by a Poisson type statistics. Other noise sources coming from the electronics of the imaging system are negligible against the photon noise. After the tomographic reconstruction the noise can be closely modeled as Gaussian additive noise.



**Fig. 18.** Comparison of noise reduction methods on medical computed X-ray tomography (electron beam CT). Shown is a slice out of the volume data showing the mediastinum in the center enclosed by the two lungs on both sides. (a) original data (b) invariant wavelet filtering, (c) anisotropic diffusion. The dotted line represents the path of the line plot presented in Fig. 19.

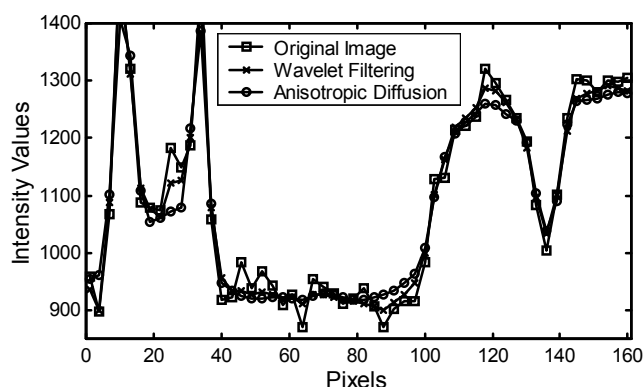


**Fig. 19.** Preservation of edges demonstrated as an effect of noise reduction methods. Shown are the line plots along the path in the slice given in Fig. 18.

Various methods for extraction of features from medical images are based on edge detection. In the following experiment the question of how well different noise reduction methods preserve edges is addressed. For this reason the proposed 3D denoising is applied and the line plots through the 3D images are compared, see Fig. 19. The edge preservation results appear to be similar for both methods, while stronger smoothing is achieved by anisotropic diffusion. The edges remain unshifted and segmentation procedures are feasible.

## 2.4 Notes on Denoising Strategies

The denoising strategy is the first question to be answered in an image processing step. By strategy it is meant the definition of the “side” conditions to be considered. A very important question is in which processing step to apply the denoising procedure. The simplest method one can do is a 2D denoising of the projection images before the 3D reconstruction. The second approach is to apply 3D image processing after the 3D image has been reconstructed. The third approach would be to exploit the 3D continuity of the 3D sinogram of the reconstruction. Thereby the set of aligned projection images is piled to a stack, which is subjected to a 3D denoising process. Subsequently, the projection images are re-extracted and used for the final 3D reconstruction. The third dimension of the stack corresponds to the tilt angle. When moving from top to bottom of the stack, any point of the object oscillates around the direction thereby following a part of a sine-curve. The finer the angular increment the higher the connectivity of this curve becomes. Assuming correct alignment and calibration of the projections, flow like features similar to that of a sinogram - should appear along the third dimension. This a priori information could be used to design the diffusion process accordingly. The features should be recognized and emphasized by coherence enhancing diffusion.

The recorded tilt-series presents the tomographic reconstruction of a frozen-hydrated mitochondrion from *Neurospora crassa* (Nicastro et al. 1999). The raw data consists of 126 projection images recorded with an CM 120 Biofilter (Philips, Eindhoven) operating at 120 kV in the zero-loss mode of the energy filter. The images cover an angular range from  $-55^\circ$  to  $60^\circ$  and are recorded with a pixel size of 1.7nm at the specimen level. The final reconstruction is performed by  $r^*$ -weighted backprojection. Due to the small angular increment, the present tilt series is a good candidate to test the different approaches.

As shown in Fig. 21 by isosurface representation, the reconstructed mitochondrion appears as an ellipsoid with a size of about 1000 nm. The inner membranes form a complex three-dimensional network of interconnected lamellae. Denoising by the hybrid approach allows one to segment and visualize this network using one threshold value for the isosurface representation. In Fig. 20 a, c, e, g the horizontal and in Fig. 20 b, d, f, h the vertical sections through the final density maps are presented. According to visual inspection, denoising the volumetric data of the final 3D reconstruction gives the best result. Edges appear with clear contrast and the density levels correspond well to the original data. Additionally no artifacts have been created. The map obtained after 2D denoising of the projection images is much less clear. The data is smoothed and the

continuity of edges is less precise. The contrast fades out locally. Also the map resulting from 3D denoising of the projection stack (sinogram) shows less contrast. However, special details, e.g. gold markers, appear with a contrast higher than that obtained with the normal approach. The vertical section also reveals a tendency to overamplify vertical high-contrast features while horizontal structures appear to be suppressed.

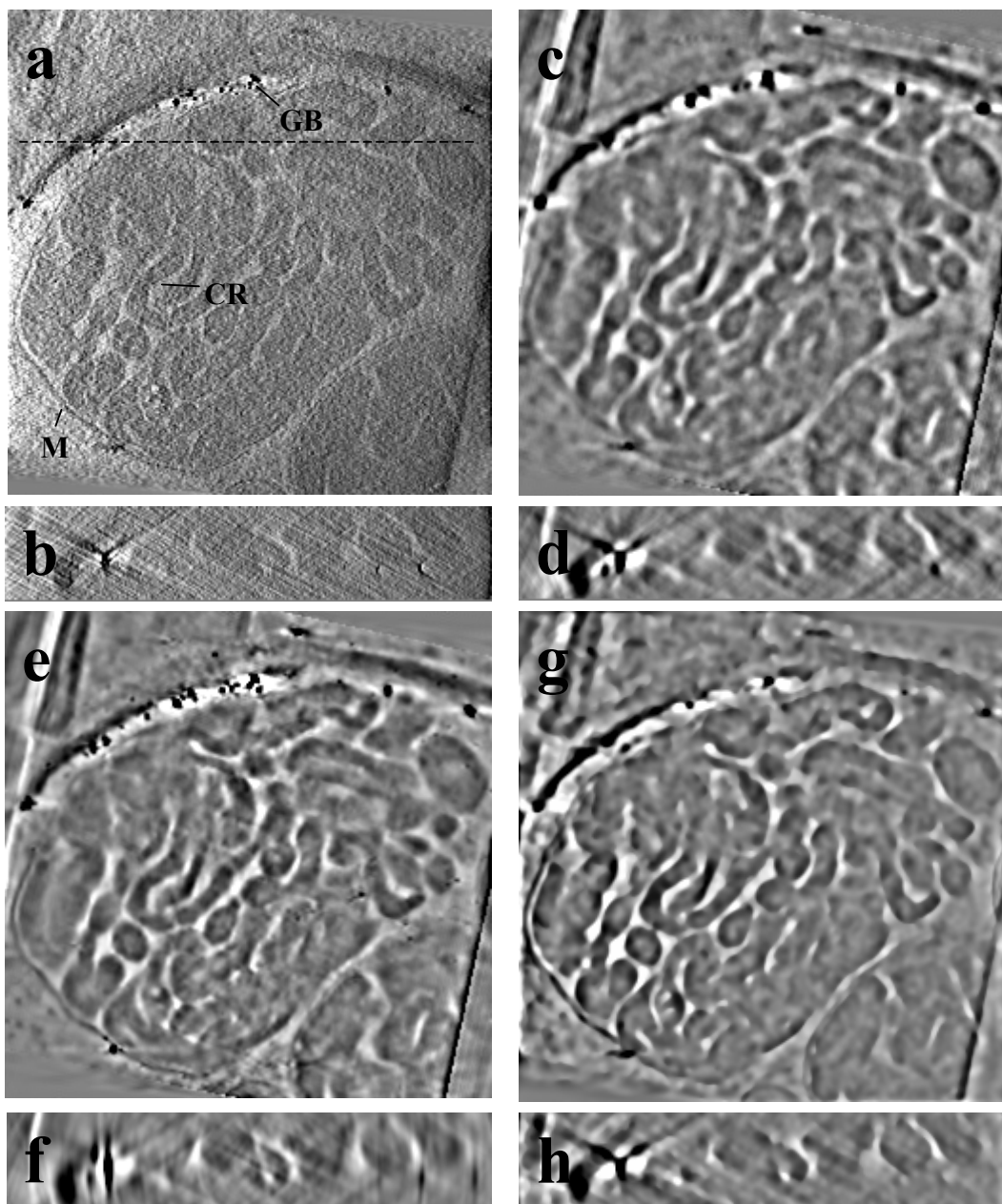


**Fig. 20.** Comparison of the denoising result using the hybrid diffusion approach, but different strategies. (a) A x-y slice from the original reconstruction. Line represents the position of the y-z slices used for the comparison (b) y-z slice from the original reconstruction. (c) the same slice as in (a), except that the images have been first filtered with the hybrid approach and used for the reconstruction afterwards. (d) y-z slice from this reconstruction. (e) x-y slice from the denoised sinogram and (f) y-z slice from this reconstruction. (g) y-z slice from the 3D denoised version and (h) corresponding y-z slice. GB = Gold bead, CR = cristae, M = Membrane.

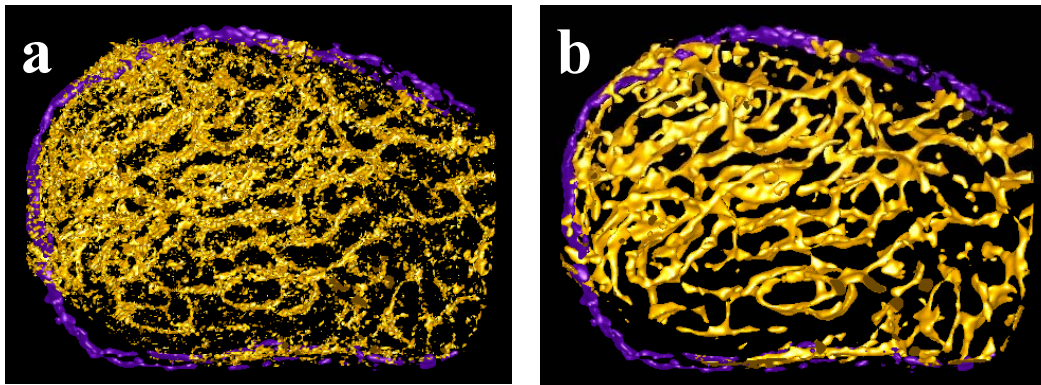


**Fig. 21.** Isosurface presentation of the reconstructed mitochondrion. (a) Original reconstruction and (b) the denoised version using the 3D hybrid approach.

## 2.5 Correlation Averaging as a Method to Evaluate the Transfer Function of the Nonlinear Anisotropic Diffusion Process

In electron microscopy, efficient noise reduction of macromolecules is normally achieved by correlation averaging (see Ch. 3). Before averaging, the signals are brought into register using cross-correlation functions. The method combines the information contained in the images of many individual, but structurally identical molecules. Each 3D image is considered to be a single realization of a statistical process. It provides a signal corresponding to the structure of the object, e.g. a projection view or a density map, degraded by noise. When assuming additive, signal-independent noise adding up equivalent signals of  $n$  3D images increases the signal-to-noise ratio by a factor  $\sqrt{n}$ . In the context of this approach it is possible to estimate the resolution of the averaged 3D image by comparing the averages of two statistically independent, equal-sized subsets of the corresponding ensemble. The comparison occurs with the Fourier shell correlation between the subsets. It is a frequency-dependent measurement of similarity between the two subsets, and therefore can be used to estimate the resolution (Saxton et. al 1982).

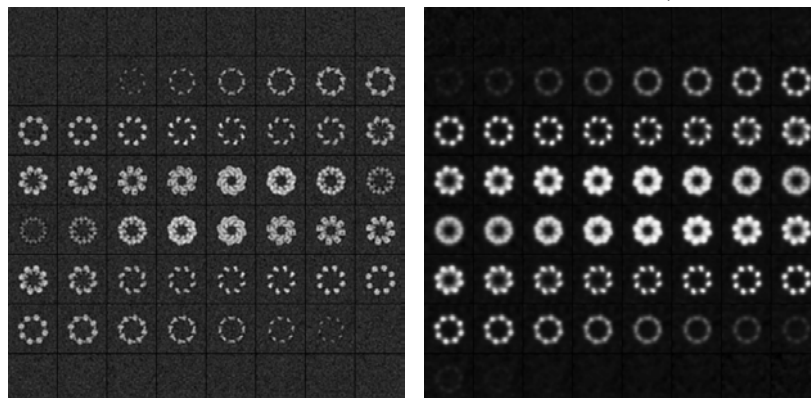


**Fig. 22.** Results of correlation averaging of two ensembles represented by slices through the volumetric data. On the left side the average of the original particles (noisy ensemble). On the right side the average of the particles denoised by EED (denoised ensemble).

Averaging is conceptually free from signal degradation, while all other denoising methods smooth the noise and more or less also the signal. In order to study how the signal is affected by nonlinear anisotropic diffusion, a set of real 3D images of a biological macromolecule was subjected to denoising and averaging. The results were assessed in the frequency domain by means of the FSC. For this purpose, 500 copies were produced from the known 3D density map of the *Thermosome* molecule (Nitsch et. al 1998) and degraded by additive colored noise. Using EED, a denoised version was created from each individual copy. Finally, averaged 3D images were calculated from both, the original “noisy” 3D images (noisy ensemble) and the denoised versions (denoised ensemble). The results are presented in Fig. 22. The average of the denoised ensemble appears smoother and significant details are suppressed. Obviously, the signal is degraded by the diffusion process.

In contrast to the apparent signal degradation, the cross-correlation coefficients of the denoised ensemble are higher than those of the noisy ensemble, indicating a higher resolution, or SNR improvement (see ch. 2.3.2.1). This surprising result does not reflect a contradiction, because nonlinear anisotropic diffusion enhances the SNR and simultaneously reduces the magnitude of the Fourier coefficients. The statement may become clearer when linear diffusion is considered. In this case, the average 3D image is also blurred but the RCF is not changed at all. Since linear diffusion is equivalent to a linear filtration using a gaussian kernel, the data in the Fourier domain are damped by a factor which is constant within shells, and the cross-correlation coefficients used for the RCF remain unchanged. Obviously, the RCF-curves in Fig. 23 reflect the gain in the SNR when linear diffusion is replaced by the edge-enhancing approach.

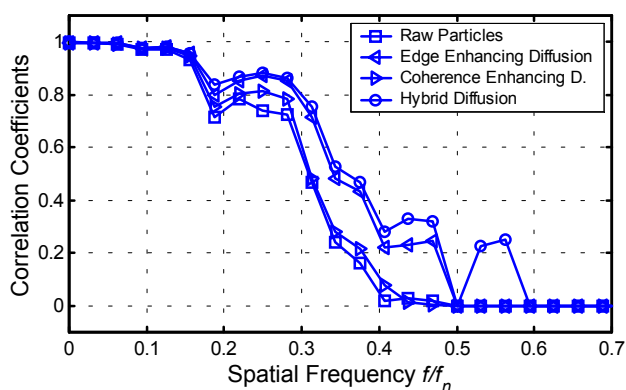


Fig. 23. Fourier shell correlation function of the denoised and original particles.

### 2.5.1 Frequency Equalization

Hybrid diffusion is a nonlinear process and cannot be described by a linear time invariant theory. Nevertheless, the improvement of the SNR described above gives some justification to improve the visual appearance of the average 3D image by using a linear frequency enhancement. The global energy in the 3D image decreases with increasing evolution time when diffusion is applied (Weickert 1998). Due to Parseval’s theorem, the energy in the Fourier domain decreases correspondingly. The amount of this decrease can be determined as a function of frequency by investigating 3D image

ensembles. As above, original and denoised 3D images representing the *Thermosome* molecule are used to calculate the root mean square amplitudes on each shell in the Fourier domain. The curve in Fig. 24 shows the ratio of mean amplitudes of the original and the denoised data and reveals a “bandstop” characteristic of edge-enhancing diffusion.

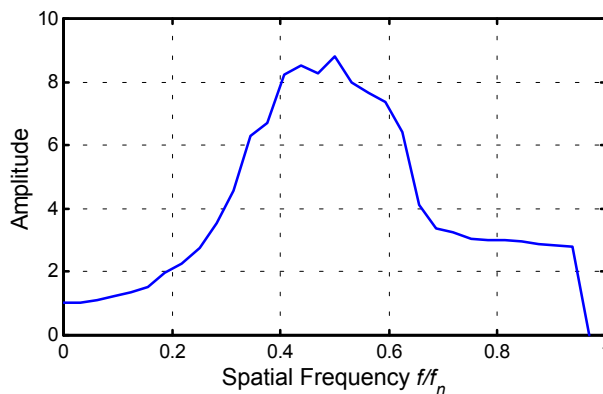


Fig. 24. Ratio of the root mean square amplitudes in the Fourier domain.

This function can be used for equalization in the conventional manner. The result when equalizing the average of the denoised particles is shown in Fig. 25. The edges are more distinct and the output looks similar to the average of the original particles. Furthermore, the noise enhancement is minimal.

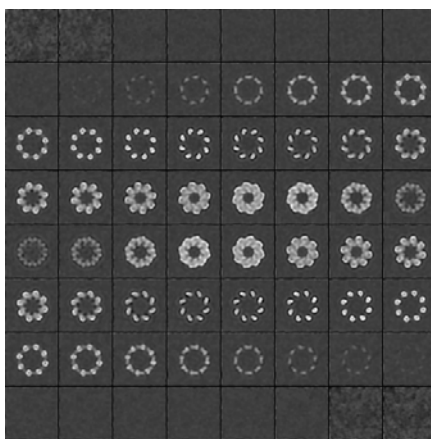
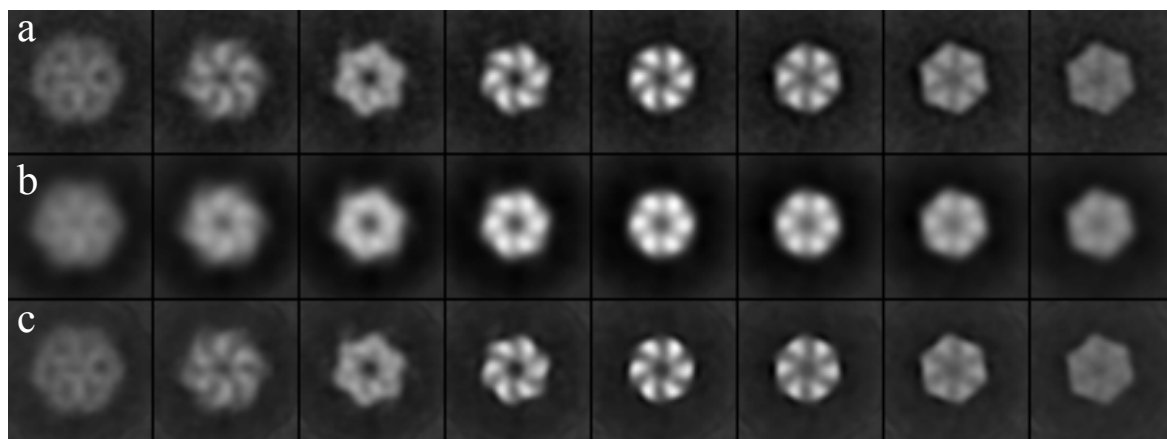


Fig. 25. Equalization of the nonlinear diffusion process

The idea arising from this observation is to determine a global “transfer function” and to equalize the data in the Fourier domain after the diffusion process. It is an open question whether or not such a function can be applied to all objects. The expected answer is no, considering the non-linearity of the diffusion procedure and the diversity of objects studied by electron tomography. It is perhaps possible to define transfer functions for distinct classes of objects. In any case, further investigations are needed to clarify this point.

### 2.5.2 Assessment of the Performance on Real Electron Microscopic Data

In order to confirm the results also with real noise a noise ensemble of VAT macromolecules has been subjected to the same procedure as with the *Thermosome* (Rockel et al. 1999). The difference here is the noise is not simulated but real. In Fig. 26 three rows of x-y slices from an averaged VAT particle are presented. For the averaging 468 individual VAT negatively stained particles have been used. In the first row is the original averaging (Fig 26a), in the second row the average of VAT after denoising with nonlinear anisotropic diffusion (Fig 26b) and in the third row the equalization of the process (Fig. 26c). The average of the denoised particles looks significantly more blurred than the average from the original particles, nevertheless the information can be regained after equalizing the process. This process becomes really interesting in the case of applying the equalization function to single particles or even cell or organelles. In this case the dumping of the low frequencies due to the diffusion process gets reversed, without enhancing the noise level, as would be the case in a linear process. In Fig. 27 an example of this approach is presented.



**Fig. 26.** Row presentation of the (a) average of the original reconstructed VAT particles, (b) averaged of the denoised particles and (c) the equalized particles.

In order to demonstrate the effect of the equalization process on not averaged single particle realizations, a single VAT particle has been chosen from the denoised ensemble and equalized. In Fig. 27a xy slices from the original VAT particle are presented. Due to the high noise level in the 3D image the structure is hardly recognizable. In Fig. 27b the denoised version is presented, where several significant blobs can be identified. At least the denoised particle has been equalized. The contrast of the equalized particle is similar to the original one. The 3D image does not look any longer blurred but seems to have a similar resolution to the original reconstructed version, with one difference: The noise has been eliminated.

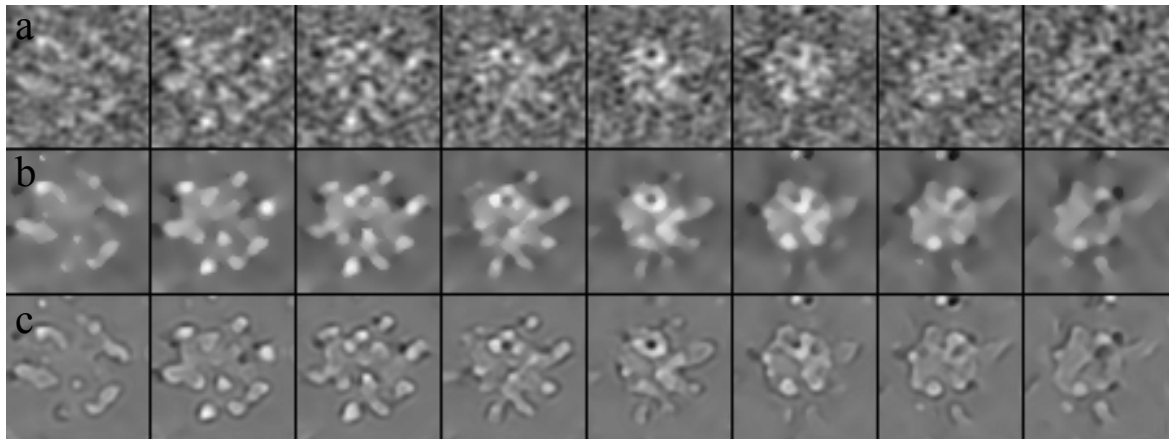


**Fig. 27.** Comparison of the equalization process in single realizations: (a) xy-slices of a single VAT particle, (b) denoised particle with nonlinear diffusion, (c) equalization of the denoised particle

After comparing the FSC curves of the original and denoised VAT particles the same effects as with the *Thermosomes* is observed. The denoised VAT average looks smoother and the FSC curve looks significantly better than the FSC curve of the original VAT particles. This demonstrates the significant SNR improvement gained by the hybrid approach of nonlinear anisotropic diffusion.

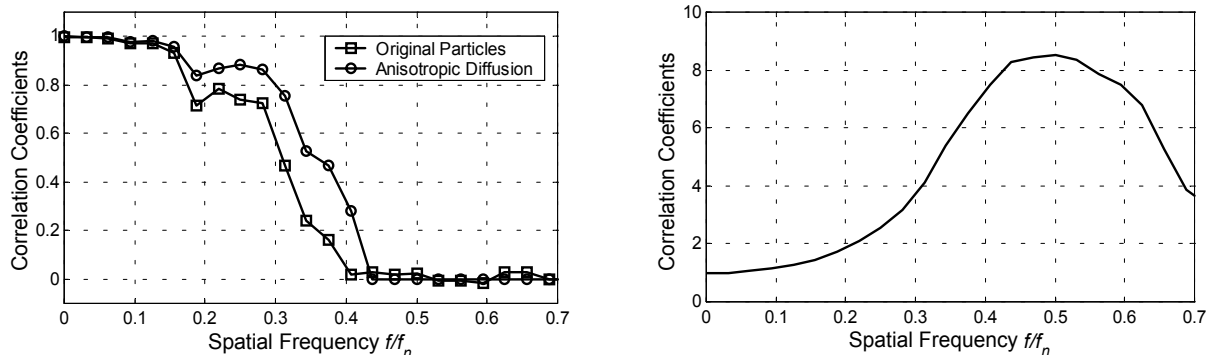


**Fig. 28.** (a) Comparison of the FSC curve of the original and the denoised VAT particles (b) equalization curve.

## 2.6 Discussion

Imaging methods in biology can suffer from a high noise level severely aggravating the visualization and interpretation of these data. In contrast to 2D data, where the human visual system is capable of adapting to various signal distortions, the interpretation of volumetric data is a demanding task which relies, entirely on computer-based visualization methods. Especially in highly degraded data the retrieval of information out of the noise remains infeasible even with advanced visualization equipment. Therefore, noise reduction is an indispensable preprocessing step.

Nonlinear anisotropic diffusion is at the moment the state-of-the-art tool for denoising electron tomographic reconstructions. The best performance is obtained on data that predominantly contain low frequency signal components. The upper frequency limit for the method to provide a significant improvement of the SNR has experimentally been determined to be bound by half the Nyquist frequency. Considering, that electron micrographs are always oversampled, this frequency sector is the most important one. The comparison with other methods, e.g. median and invariant wavelet filtering, confirms the first statement.

Further advantages of the nonlinear anisotropic diffusion arise from the solid mathematical foundation of the method. The process yields an excellent edge preservation or even enhancement without creating any artifacts or anisotropies. Therefore several other post-processing methods are facilitated and can unfold their whole potential. Additionally nonlinear anisotropic diffusion is a very fast method, which can be integrated at many image processing packages.

## Chapter 3

# Object Detection in 2D and 3D Electron Microscopic Images

Object detection and identification in 2D or 3D images are tasks of major interest in electron microscopy, since there is a great need for reliable detection methods. Therefore the application of the algorithms is on two major fields essential:

- a) In order to reveal molecular resolution in 2D electron microscopy up to one million particles must be averaged after extraction from several thousand electron micrographs. The collection of molecules is usually done interactively under visual control. This procedure is time consuming and strongly affected by human subjectivity. Up to now many methods have been proposed to automate this procedure, but none of them has become a standard. Automatic detection of molecules from such micrographs (2D scenes) would facilitate and accelerate the analysis considerably.
- b) With the recent and exciting development in electron tomography and the improvement of the resolution down to a molecular level, proteins can be identified and studied in an unperturbed cellular context. In order to localize the molecules a fast, automated procedure is necessary.

There is a large variety used for detecting a target in a scene. The ideal detection method should be robust with respect to a low signal-to-noise ratio (SNR), varying object orientation, object deformations, background variations, and image distortions, and it should be able to cope with multiple occurrence of the object. Considering the low SNR, cross correlation between target and scene would be the method of choice due to the high significance of the cross correlation peak. However, cross correlation is not rotationally invariant and requires scanning the whole angular range. This is a computationally ineffective approach, especially in the case of searching 3D targets in extended volume data. Therefore, a new approach is presented, where the task is separated into two independent steps:

- 1) The scene or volume will be segmented into small areas of interest where objects can be located with a probability higher than in the original environment
- 2) The resulting areas will be further analyzed using established methods, e.g. image classification.

To perform the first step mean curvature motion (MCM) is used, which can be understood as a nonlinear, anisotropic diffusion process or, equivalently, as a geometric method where level curves (isointensity contours) of the image move as a function of the local curvature and the modulus of the image gradient (Alvarez et al. 1993)

The development was motivated from several virtues of the method: First of all it contains only one parameter, which can be automatically derived from the size of the object. Second, the method is one of the fastest possible schemes based on curvature controlled approach. Third, the method is translation and rotation invariant. Fourth, it is not affected from contrast differences.

From a more general point of view it may be interesting to note that the approach is different from a typical image restoration method which seeks to reduce noise and to preserve the signal. Using MCM, signal and noise are iteratively and simultaneously degraded. Therefore noise degrades faster due to higher curvature. The remaining signal then simply indicates the position of the object that should be detected.

### 3.1 The Algorithm

#### 3.1.1 Mean Curvature Motion

Mean curvature motion can be considered either as a special case of nonlinear anisotropic diffusion, or as an evolution of a level curve moving as a function of the local curvature. Linear diffusion in a two-dimensional image  $I$  can be described by the equation

$$I_t = \partial_{xx} I + \partial_{yy} I,$$

where the subscripts denote differentiation with respect to the time  $t$  and to the Cartesian coordinates  $x$  and  $y$ . After a principal axis transformation (Karhunen-Loewe transformation) in the direction of the highest variance, the diffusion equation can be rewritten, in the following form,

$$I_t = \partial_{\xi\xi} I + \partial_{\eta\eta} I, \quad (11)$$

with  $\xi \perp \nabla I$  and  $\eta \parallel \nabla I$ . Neglecting the diffusion flux in the direction of the gradient  $\nabla I$  results in an anisotropic diffusion process represented by the simple equation

$$I_t = \partial_{\xi\xi} I. \quad (12)$$

Alvarez et al. (1993) derived a “real anisotropic diffusion equation” of the form

$$\frac{\partial I}{\partial t} = |\nabla I| \cdot \operatorname{div} \left( \frac{\nabla I}{|\nabla I|} \right) \quad (13)$$

with the aim to improve the edge preservation by smoothing the image along level lines. Apart from the dimension-independent form, this equation is identical to the previous one, as can be shown by straightforward calculations.

The name “mean curvature motion” (MCM) originates from a more geometric point of view. The basic idea was formulated first in the theorem of Grayson (1987), which states

that a curve moving under its own curvature is going to collapse to a point and disappear. Following Osher and Sethian (1988), the motion of the zero level set of a higher dimensional image  $I$  can be described by

$$I_t = F(\kappa)|\nabla I|, \quad (14)$$

where  $F(\kappa)$  is a function of the curvature  $\kappa$ . Substituting the motion function  $F(\kappa)$ :

$$F(\kappa) = \kappa = \operatorname{div} \left( \frac{\nabla I}{|\nabla I|} \right) \quad (15)$$

again results in the ALM equation. In two dimensions the curvature  $\kappa$  in Cartesian coordinates can be described by

$$\kappa = \frac{I_{xx}I_y^2 - 2I_xI_yI_{xy} + I_{yy}I_x^2}{(I_x^2 + I_y^2)^{3/2}} \quad (16)$$

and in three dimensions the mean curvature  $\kappa_{Mean}$ :

$$\kappa_{Mean} = \frac{\left[ (I_{yy} + I_{zz})I_x^2 + (I_{xx} + I_{zz})I_y^2 + (I_{xx} + I_{yy})I_z^2 - 2I_xI_yI_{xy} - 2I_xI_zI_{xz} - 2I_yI_zI_{yz} \right]}{(I_x^2 + I_y^2 + I_z^2)^{3/2}} \quad (17)$$

For the discretization scheme the level set technique has been used.

The discretization operators are defined in the following way:

$$D^{-x}I \equiv \frac{I(x, y, z, t) - I(x - h, y, z, t)}{h}, \quad D^{+x}I \equiv \frac{I(x + h, y, z, t) - I(x, y, z, t)}{h}, \quad (18)$$

$$D^{0x}I \equiv \frac{I(x + h, y, z, t) - I(x - h, y, z, t)}{2h}$$

For the 2D case the equation can be written in the following form:

$$D^{+t}I = dt \left\{ \begin{array}{l} (D^{0x}I_{i,j})^2 \cdot D^{0y0y}I_{i,j} + (D^{0y}I_{i,j})^2 \cdot D^{0x0x}I_{i,j} \\ - \max(D^{0x}I_{i,j} \cdot D^{0y}I_{i,j}, 0) \cdot (-I_{i-1,j+1} + I_{i,j+1} + I_{i+1,j} - 2 \cdot I_{i,j} - I_{i+1,j-1} + I_{i,j-1} + I_{i-1,j}) \\ - \min(D^{0x}I_{i,j} \cdot D^{0y}I_{i,j}, 0) \cdot (I_{i+1,j+1} - I_{i,j+1} - I_{i+1,j} + 2 \cdot I_{i,j} + I_{i-1,j-1} - I_{i,j-1} - I_{i-1,j}) \end{array} \right\} \quad (19)$$

$$/ \left( (D^{0x}I_{i,j})^2 + (D^{0y}I_{i,j})^2 \right)$$

or with the discretization operators:

$$D^{+t}I = dt \cdot \frac{\left\{ \begin{array}{l} (D^{0x}I)^2 \cdot D^{0y0y}I + (D^{0y}I)^2 \cdot D^{0x0x}I \\ - \max(D^{0x}I \cdot D^{0y}I, 0) \cdot (D^{-x+y}I + D^{+x-y}I) \\ - \min(D^{0x}I \cdot D^{0y}I, 0) \cdot (D^{-x-y}I + D^{+x+y}I) \end{array} \right\}}{\left( (D^{0x}I)^2 + (D^{0y}I)^2 \right)} \quad (20)$$

In the 3D case:

$$D^{+t}I = dt \cdot \left\{ \begin{array}{l} (D^{0x}I_{i,j,k})^2 (D^{0y0y}I_{i,j,k} + D^{0z0z}I_{i,j,k}) + (D^{0y}I_{i,j,k})^2 \cdot (D^{0x0x}I_{i,j,k} + D^{0z0z}I_{i,j,k}) \\ + (D^{0z}I_{i,j,k})^2 \cdot (D^{0x0x}I_{i,j,k} + D^{0y0y}I_{i,j,k}) \\ - \max(D^{0x}I_{i,j,k} \cdot D^{0y}I_{i,j,k}, 0) \cdot \\ (-I_{i-1,j+1,k} + I_{i,j+1,k} + I_{i+1,j,k} - 2 \cdot I_{i,j,k} - I_{i+1,j-1,k} + I_{i,j-1,k} + I_{i-1,j,k}) \\ - \min(D^{0x}I_{i,j,k} \cdot D^{0y}I_{i,j,k}, 0) \cdot \\ (I_{i+1,j+1,k} - I_{i,j+1,k} - I_{i+1,j,k} + 2 \cdot I_{i,j,k} + I_{i-1,j-1,k} - I_{i,j-1,k} - I_{i-1,j,k}) \\ - \max(D^{0x}I_{i,j,k} \cdot D^{0z}I_{i,j,k}, 0) \cdot \\ (-I_{i-1,j,k+1} + I_{i,j,k+1} + I_{i+1,j,k} - 2 \cdot I_{i,j,k} - I_{i+1,j,k-1} + I_{i,j,k-1} + I_{i-1,j,k}) \\ - \min(D^{0x}I_{i,j,k} \cdot D^{0z}I_{i,j,k}, 0) \cdot \\ (I_{i+1,j,k+1} - I_{i,j,k+1} - I_{i+1,j,k} + 2 \cdot I_{i,j,k} + I_{i-1,j,k-1} - I_{i,j,k-1} - I_{i-1,j,k}) \\ - \max(D^{0y}I_{i,j,k} \cdot D^{0z}I_{i,j,k}, 0) \cdot \\ (-I_{i,j+1,k-1} + I_{i,j+1,k} + I_{i,j,k+1} - 2 \cdot I_{i,j,k} - I_{i,j-1,k+1} + I_{i,j-1,k} + I_{i,j,k-1}) \\ - \min(D^{0y}I_{i,j,k} \cdot D^{0z}I_{i,j,k}, 0) \cdot \\ (I_{i,j+1,k+1} - I_{i,j+1,k} - I_{i,j,k+1} + 2 \cdot I_{i,j,k} + I_{i,j-1,k-1} - I_{i,j-1,k} - I_{i,j,k-1}) \end{array} \right\} / \quad (21)$$

$$\left( (D^{0x}I_{i,j,k})^2 + (D^{0y}I_{i,j,k})^2 + (D^{0z}I_{i,j,k})^2 \right)$$

or with the discretization operators:

$$D^{+t}I = dt \cdot \frac{\left\{ \begin{array}{l} (D^{0x}I)^2 (D^{0y0y}I + D^{0z0z}I) + (D^{0y}I)^2 \cdot (D^{0x0x}I + D^{0z0z}I) + (D^{0z}I)^2 \cdot (D^{0x0x}I + D^{0y0y}I) \\ - \max(D^{0x}I \cdot D^{0y}I, 0) \cdot (D^{-x+y}I + D^{+x-y}I) - \min(D^{0x}I \cdot D^{0y}I, 0) \cdot (D^{-x-y}I + D^{+x+y}I) \\ - \max(D^{0x}I \cdot D^{0z}I, 0) \cdot (D^{-x+z}I + D^{+x-z}I) - \min(D^{0x}I \cdot D^{0z}I, 0) \cdot (D^{-x-z}I + D^{+x+z}I) \\ - \max(D^{0y}I \cdot D^{0z}I, 0) \cdot (D^{-z+y}I + D^{+z-y}I) - \min(D^{0y}I \cdot D^{0z}I, 0) \cdot (D^{-z-y}I + D^{+z+y}I) \end{array} \right\}}{\left( (D^{0x}I)^2 + (D^{0y}I)^2 + (D^{0z}I)^2 \right)} \quad (22)$$

The discretization model is very stable and fulfills the min-max principle, but it does not satisfy the mean value principle. With the above described discretization stencil the further simulations and the image segmentation are presented.

### 3.1.2 Peak Search Method

MCM forces the level sets of the image to move along their vector field with a speed that is a function of the curvature. Hence, structures, artifacts and noise degrade to convex objects, called “blobs” further on. The longer the procedure lasts, the more level sets degrade to points, consequently objects with smaller diameter disappear first. The rate of alteration of the radius  $r(t)$  of the objects as a function of the iteration time  $t$  can be described by the following equation

$$r(t) = \sqrt{r(0)^2 - c \cdot t^2}, \quad (23)$$

where  $c$  is a constant.

The resulting image consists of blobs with different sizes. To facilitate further analysis only those blobs corresponding to an object of interest with high probability should be detected. All searched particles degrade to blobs with almost the same diameter, which can easily be detected, applying the equation described above. To detect only the blobs of interest, independent from large-scale gradients on the image, a more sophisticated scheme is used than a simple maximum detection algorithm, since the search strategy is extremely important for the success of the method. The procedure is the following: First, a maximum of an area is determined. A circle with the diameter of the particle is cut out and the maximum of the boundary of the circle is calculated. If the maximum satisfies a certain threshold the peak is going to be further classified. This procedure ensures that only the objects with the predetermined size are going to be detected. The method was implemented in the EM software package (Hegerl 1996).

## 3.2 Object Detection with Simulated EM Data

Imaging of biological macromolecules with the electron microscope has to be done with a very low electron dose in order to avoid radiation damage of the objects. In addition to the resulting noise, any processing is aggravated by noise-like background variations originating from the superimposed image of the specimen support. Frequently enough, the SNR is so low that particles cannot be identified unambiguously by the eye. Therefore, in a first approach, simulated images have been used to assess quantitatively the performance of the proposed detection method. With artificial data, the number and position of particles is known and the SNR can be modified.

In order to assess the performance of the method, simulated tilt series with real particles have been reconstructed. Several microscope properties, e.g. alignment problems, alignment error, transfer function, etc. have been included (with typical values) in the reconstruction of the synthetic volumes. The particles have been placed inside these volumes with random translation and rotation.

### 3.2.1 Detection in 2D Images

To make the simulation as realistic as possible, images have been recorded with the electron microscope showing a thin film of amorphous ice with some small gold clusters embedded. The gold clusters are used as alignment markers in further processing steps. Projections of biological macromolecules were pasted into the images using known but random translation and orientation positions. The contrast of the particles was chosen such that the SNR corresponds to approximately  $-1\text{dB}$ .

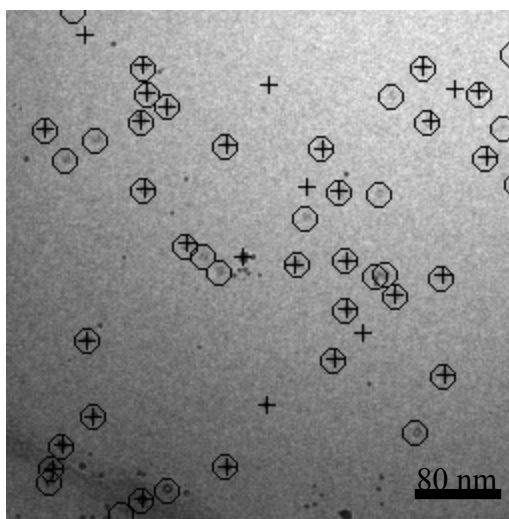


**Fig. 29.** Realistic background image, including contamination, with particles pasted in (marked by circles), corresponding to an SNR of  $-1\text{dB}$ . The crosses (+) visualize the detection result.

The resulting image (Fig. 29) was processed using MCM for segmentation in order to derive the most likely positions for particles. More than 70% of the particles have been detected correctly. The gold particles in the image don't affect the result at all, as their radius is smaller from the particles to be detected. The algorithm is robust with respect to noise and long-wavelength gradients and is independent from the local gray mean value.

An important discussion point is the performance of the method on closely placed or overlapping particles. A characteristic attribute of the method is that two connected surfaces remain connected for the whole processing time, even if the junction is one pixel. Two overlapping particles are not detected immediately with the peak search method described above. A second point of interest is the performance of the method on particles that consist on two subunits, which does not build a coherent surface. In this case it is possible that the high contrast areas, characterizing each subunit, disappear due to the small surface they include and the low contrast background remains. Hence, such a particle would not get detected at all. The drawbacks described above affect the detection of particles and limit the performance of the algorithm.

### 3.2.2 Detection in Volume Data

In the following test calculations the typical artifacts of the electron tomographic reconstructions are simulated in order to exploit the performance of the detection method realistically. To illustrate how MCM affects the object to be detected, the evolution of a macromolecule *Thermosome* is presented, which is moving under its curvature (Fig. 30).

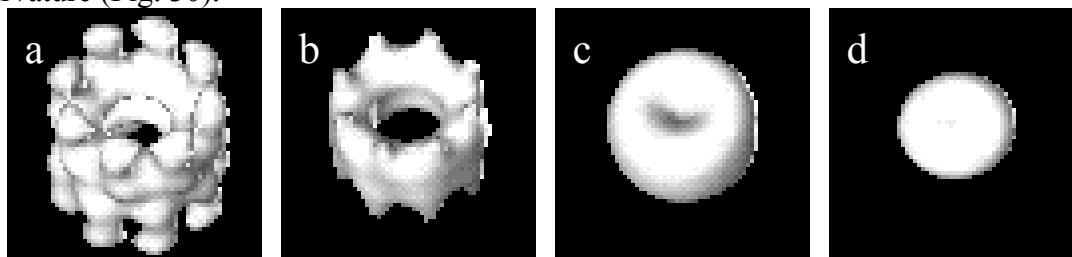


**Fig. 30.** Evolution of the *Thermosome* molecule under the effect of MCM. The size of the particle is about  $10 \times 10 \times 14 \text{ nm}^3$  and the volume size is  $20 \times 20 \times 20$  voxels. (a) Original particle and evolution after (b) 6 iterations, (c) 12 iterations and (d) 20 Iterations.

After processing the particle with MCM the following observations are made: The protrusions of the particle, places with high curvature, are eliminated first. The particle degrades slowly to a toroidal structure. By further processing the particle degrades to a sphere (Fig. 30d). The created blob is in the center of the position of the particle and is the place to be detected with the peak search algorithm. In general the position, where the level sets degrade is not known. Nevertheless for symmetric particle it is always the center and for non-symmetric particles the place of the singularity can be found easily.

An artificial volume with 500 randomly rotated and translated *Thermosomes* has been generated. The volume was projected from  $-60^\circ$  to  $+60^\circ$  with an increment of  $3^\circ$  using the x-axis as tilt axis (41 Projections). Colored noise was added to the projected images, simulating the shot noise of the electrons as well as the low pass effect of the transfer function of the microscope. The drift of the specimen holder, mostly in one direction, has been simulated by convolutions with an anisotropic low pass kernel. Additionally, each projection image was subjected to a random displacement with a variance of one pixel, in order to simulate the alignment errors. The resulting images were used to reconstruct a volume using weighted backprojection.

As shown in Fig. 30, 20 iterations were used to degrade the *Thermosome* particle to a spherical structure with a radius of about 3 voxels. Considering the volume obtained by the tomographic reconstruction, the particles are elongated in z-direction due to the restricted tilt range. Consequently, the 3D blobs resulting from the MCM process are elongated too. Since the amount of elongation is predefined, a cover correcting for the elongation can be assigned to each blob and used for discrimination similarly as for the circle in the 2D case.

The performance of the method is almost constant with a SNR above  $-1.5\text{dB}$  (Fig. 31). All the particles can be correctly identified, without any false findings, apart from those at the boundary of the volume. With a SNR of less than  $-2.5\text{dB}$  more than 60% of the particles could be directly identified, though the number of false findings is very high.

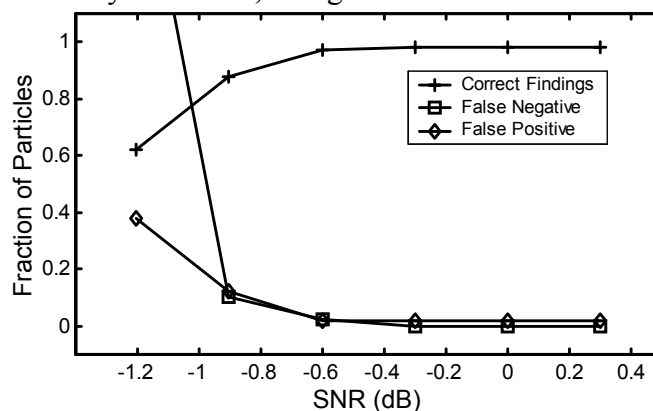


**Fig. 31.** Result of particle detection in a synthetic 3D image data. The solid line with crosses represents the particles, which have been detected with a difference of two pixels (Manhattan distance) from their true position. The diamonds indicate false findings, that is findings with no correspondence of an object. The circles represent the particles that haven't been detected.

### 3.3 Application on Real Data

The performance of the algorithm is exploited on real data, where 2D images as well as 3D images of biological macromolecules are processed. A comprehensive comparison with the detection results of a person is obtained.

#### 3.3.1 2D Processing

Several detection results on various kinds of images are performed in order to exploit the performance of the method. The first example is a negative staining image of VAT. The curvature of the molecules (diameter ca. 14nm, corresponding to 15 Pixels) with respect to the noise results in a longer “life-time” of the particles when processed. The images are from very low SNR and the position of the particles can not be unambiguously identified by eye. The original image is presented in Fig. 32a and the processed image after 20 iterations in Fig. 32b. The bright blobs correspond to possible positions of the molecules. Even though the SNR is very low, the blobs have a significant contrast and can be clearly separated from the background. The particles in contact with each other are not detected because the area resulting from the MCM procedures is twice as big as the correct blob.

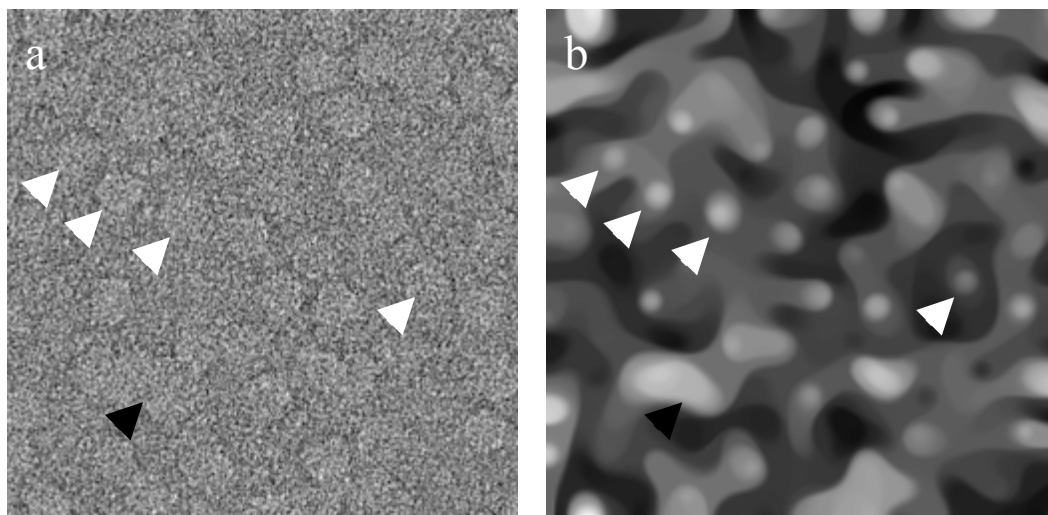


**Fig. 32.** 256\*256 pixels sized electron micrograph showing molecules with a diameter of about 30 pixels, (corresponding to 14nm). (b) The processed version of the image. Bright spots (“blobs”) appear at the positions of molecules. The white arrows point to some particles and the corresponding blobs created by MCM. The black arrow points to a place, where particles are in contact and therefore the diameter of the blob is much larger, than the rest.

### 3.3.2 Comparison of the Performance of Interactive Particle Detection and Automatic Procedure

A quantitative comparison between the human observer and the automatic procedure is very difficult for various reasons: First of all there is no guarantee that a person marks every particle on the field. Second, his choice is always subjective and the marked particles hence obey already a sort of a classification. Despite this, to make a performance evaluation, a data set interactively collected, from negative staining images of *Trilob* was compared to an automatically collected data set. *Trilob* is a particle consisting of three distinct subunits (Fig. 34). It represents the worst case for object detection with MCM, because no significant closed contour surrounds the particle. In this case the three subunits would degrade independently from each other.

Several electron micrographs have been recorded in order to collect a relatively large number of particles. In total 1200 particles have been selected interactively and 1500 particles after processing the data with MCM. A typical image, with the detection spots from the human (+) and MCM (O) is presented in Fig. 33. The result after averaging all the particles collected by both is presented in Fig. 34. After visual inspection no significant differences could be found, even though the automatic selected data set has not been classified before. The averages have also been compared with Fourier shell correlation, where the better (more selective) clicking performance of the human becomes clear. The results after classification of the data are identical.

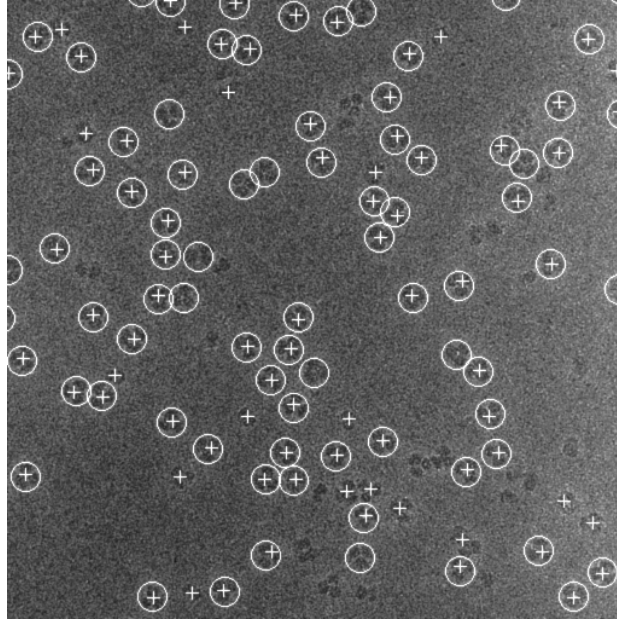


**Fig. 33.** Comparison of the human (+) and automatically marked particles (O)

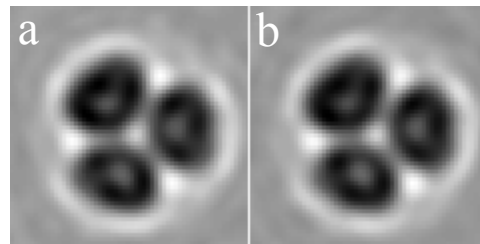


**Fig. 34.** 2D Average of the macromolecule *Pyrococcus furiosus*. Comparison of the averages of the (a) “human” marked particles and (b) MCM detected particles.

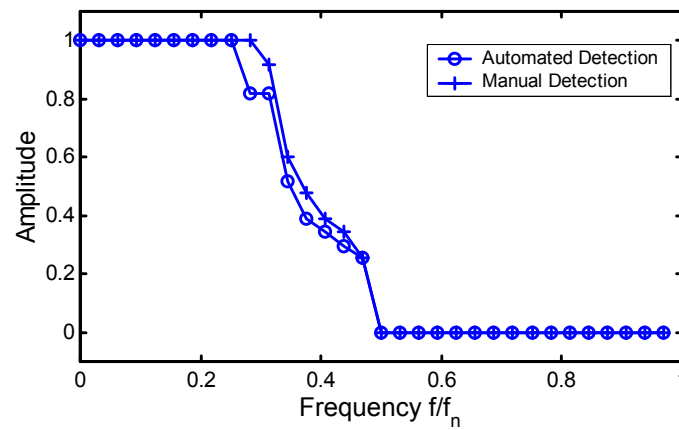


**Fig. 35.** Comparison of the different performances by the Fourier shell correlation coefficients. The better resolution of the automated selected data set corresponds to better SNR and therefore to a better performance.

### 3.3.3 3D Processing

Three tomographic tilt series of purified and ice-embedded *Thermosomes* (15nm diameter, 16nm height), were recorded and processed. The 3D reconstruction was performed by  $r^*$ -filtered backprojection into volumes of  $512 \times 512 \times 256$  voxels, each voxel corresponding to  $1\text{nm}^3$ . Fig. 36 shows one of these volumes reconstructed from a series taken in the angular range from  $-62^\circ$  to  $+70^\circ$  with an increment of  $1^\circ$ .

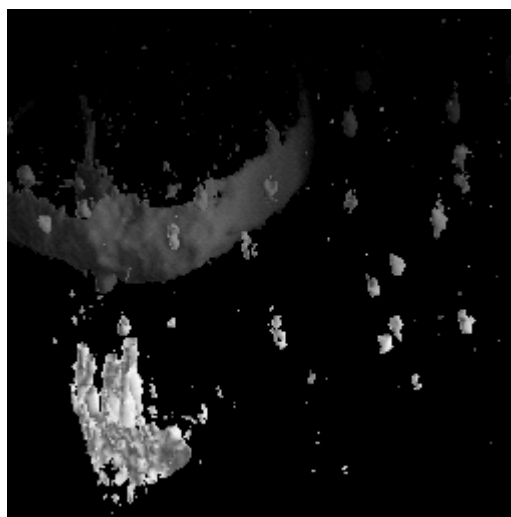


**Fig. 36.** : Isosurface presentation of a  $256^3$  voxels sized volume, reconstructed by  $r$ -filtered backprojection from a tilt series of *Thermosome* particles. The volume contains a vesicle (large object in the back left, with a diameter of about 100nm), molecules to be detected in the front, with a size of 15nm and artifacts due to contamination in the front left.

The volumes were processed using MCM until the gold clusters disappear and the only remaining objects are the biological molecules. Typically for the method, blobs appear with maximum peaks corresponding to the center of the *Thermosome*. All macromolecules visible in the volume could be automatically identified. The enormous data reduction gained by the MCM-based volume segmentation allows refining the cut-out volumes using classical methods like matched filter, for the translational as well as for the rotational position. Instead of scanning the entire volume applying time inefficient correlation techniques, a scan of the reduced volumes is sufficient (data reduction of 1/4000).

Segmentation with MCM is not a tool just considered for single particle analysis. The segmentation results can be further used for object segmentation in tomographic reconstructions of cells and organelles. The resulting blobs can be further analyzed by cross correlation techniques. With MCM it is possible to classify particles with one pixel difference in their diameter. This is just SNR dependent and therefore never the case in electron microscopic images.

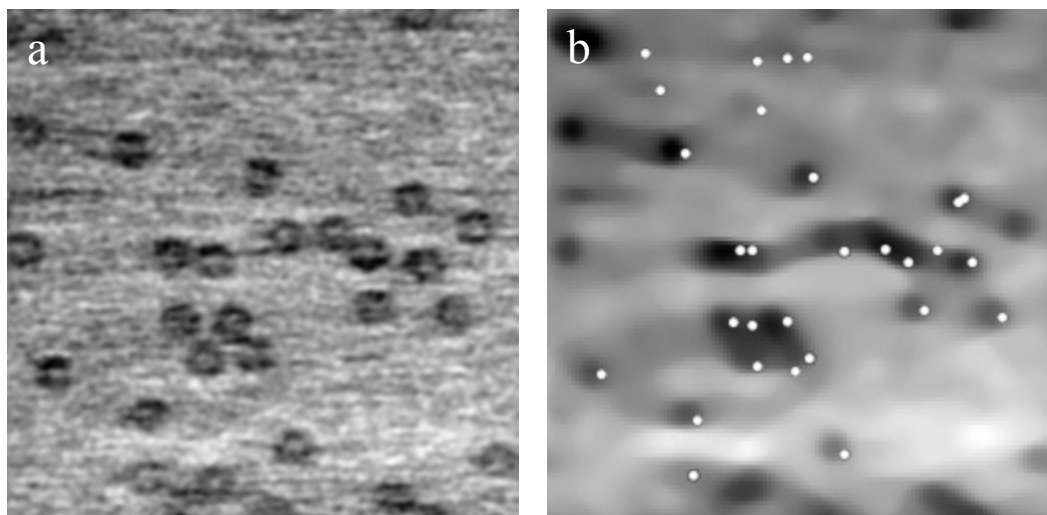


**Fig. 37.** Comparison of the detection result of *Thermosome* particles in a 3D reconstructed volume. a) One central xy-slice through the tomographic reconstruction is presented. b) and after processing with mean curvature motion. The white dots represent the positions of the *Thermosomes*.

### 3.4 Discussion

The mean curvature motion approach for automated data detection proposed here, has several benefits. The technique is not considered as a stand alone process, but as the first part of a fast and reliable object detection. As shown in the flow diagram below (Fig. 38), MCM is applied first. When subjecting noisy EM data to this procedure, areas corresponding to particle images shrink to small, almost noise-free blobs which can be detected automatically by a peak search routine. Obviously, the process includes an effective noise reduction and approximately preserves the center of mass of each particle. Due to the image segmentation, the following analysis with respect to type, exact position, and orientation of the particle, e.g. using matched filter, can be performed separately for each particle within a small volume centered on the blob. When compared to the entire image or volume, this corresponds to an enormous data reduction. The algorithm is also very fast. As an example, 15 sec are needed for one iteration of a  $256^3$  volume on a R10000 SGI processor. The number of iteration steps - typically 20-30 - is predefined depending on the particle size.

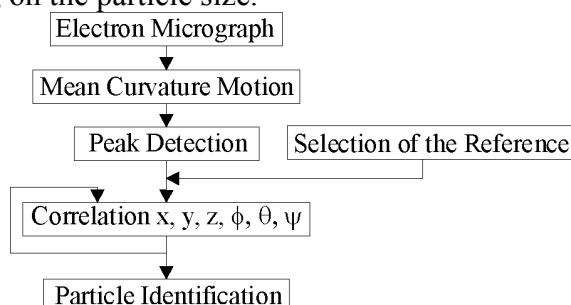


**Fig. 38.** Flow diagram of the detection procedure.

---

Considering a SNR of  $-1.5\text{dB}$ , the rate of successful and false findings is absolutely satisfactory. Problems occur when particles are in contact with each other. The peak search algorithm due to a larger blob will exclude these particles. Following the experience of the subsequent analysis this may not really be a loss because in the case of such findings the final averaging of particle images may be disturbed. Severe problems occur when a particle image appears as set of unconnected areas. Corresponding blobs will disappear after a few iteration steps and any detection is prevented. It is a subject of further investigation whether a suitable preprocessing of the image would help to overcome this problem.

One might think that simple low-pass filtering could be used instead of MCM. However, in contrast to MCM, there is no difference between blobs resulting from small, high contrast features and those from broader objects with less contrast. The pre-known size of the particles of interest can be used to adjust the iteration time accordingly. Applying the peak-search algorithm described above, the position of the objects can be determined with high accuracy, excluding the detection of artifacts in the volumes. To summarize the results, MCM is as a preprocessor a promising concept for an efficient and reliable approach to automatic object detection in 2D and 3D biological electron microscopy.



## Chapter 4

# Multidimensional Image Segmentation with Active Contours

Edge detection, segmentation, and shape recovery is essential for every visualization tool. Independent of an interactive, semi-automatic, or fully automated technique the separation of images (2D as well as 3D) into several more homogenous and coherent compartments becomes indispensable as the image complexity grows. In electron microscopy the feature of interest corresponds usually to a region whose pixels are of different grayness intensity, at least locally. The goal is to locate this shape within the image and then perform segmentation (separation from the rest of the image) and further shape analysis and perhaps recognition.

The most straightforward approach to this task is to use threshold criteria; simply decide that the boundary of the desired shape corresponds to the pixels whose values are larger or smaller than a user-defined value. Indeed, for regions with very sharply delimited contrasts between the interior and the exterior this works well. But in many cases the image contains small features and noise with comparable high contrast, which should not influence or included in the segmentation results. An imaginary curve has to be moved towards its interior or its exterior direction as a function of the local image properties, which should stop at the desired boundary. The first approach was motivated by the work of Kass, Witkin, and Terzopoulos (1988). Their idea was to define a certain amount of markers outside the boundary of the object. Spring forces (attractive and bending forces) connect these markers (from now on called “snake”) with each other. By creating a force balance between the forces contracting the snake and external forces caused by image features a solution can be developed. The handicap is that no topological changes can take place and no forces exist to push the snake into the areas with concave boundaries.

A new discretization technique, the so called “level set” appears to be the solution to the problem since arbitrary conformational changes of the snake can be handled unambiguously. The idea here is to embed the snake into a higher dimensional function (Malladi et al. 1996). Then it is moved in the direction of the normal, as a function of the image gradient, in order to segment the object of interest. Assumptions about the object properties are made, e.g. lower curvature and a higher contrast than the surrounding environment. The snake then becomes capable of ignoring the insignificant and uninteresting features e.g. noise and produces a satisfying segmentation result.

## 4.1 Segmentation Technique

Consider a closed, smooth curve  $I_p$  evolving in an Euclidean  $R^2$  plane in time  $t$ . It is assumed that the curve is moving along its normal vector field with speed  $F(\kappa)$ , a given scalar function for the curvature  $\kappa$ . Let  $\mathbf{x} = \mathbf{x}(s, t)^T$  be the position vector, which parameterizes the curve  $\gamma(s, t)$  by  $s$ ,  $0 \leq s \leq S$ , where  $s$  is that radian and  $t$  the time. One numerical approach than, is to take the Lagrangian description of the problem, produce equation of motion for the position vector  $\mathbf{s}$ , and then discretize the parameterizations with a set of discrete marker particles at the moving front. However this approach has several disadvantages and is in general unstable as discussed in Sethian (1996). Additional problems occur, because topological changes e.g. the curve merges or splits can not be handled. Therefore the idea is to embed the curve  $\gamma(t)$  as the zero level set in a higher dimensional function  $\phi(\mathbf{x}(t), t)$ , where  $\mathbf{x}$  are the Cartesian coordinates. The function  $\phi$  remains then a continuous function even if the curve  $\gamma(t)$  changes the topology.

Consider the motion of one level set  $\phi = const$  of the higher-dimensional function  $\phi$ . The zero level describes the snake position  $\gamma(t)$ , which should segment the object of interest. The equation of motion can then be written in the following form:

$$\gamma(t) \rightarrow \phi(\mathbf{x}(t), t) = 0 \quad (24)$$

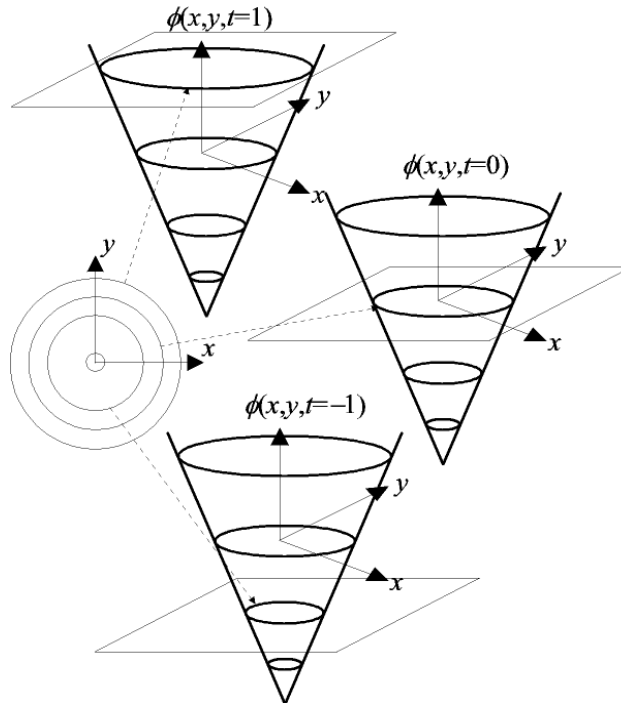


**Fig. 39.** Demonstration of the expansion or collapse of a single level set as the function of the normal and the curvature. Several different zero level sets are presented (Different iteration times). The same higher dimensional function handles the movement of one curve.

The speed function  $F$  points to the normal direction  $\mathbf{n}$  of this level set and is described by:

$$F = \mathbf{x}_t(t) \cdot \mathbf{n}, \quad (25)$$

Where  $\mathbf{x}_t(t)$  denotes the derivative corresponding to the evolution time  $t$  and the normal vector  $\mathbf{n}$  is given by:

$$\mathbf{n} = \frac{\nabla\phi}{|\nabla\phi|} \quad (26)$$

The chain rule produces,

$$\frac{\partial}{\partial t}\phi(\mathbf{x}(t), t) = 0 \quad (27)$$

and further:

$$\phi_t + \nabla\phi(\mathbf{x}(t), t) \cdot \mathbf{x}_t(t) = 0 \quad (28)$$

Substitution yields

$$\phi_t + F \cdot |\nabla\phi| = 0, \quad (29)$$

which is the level set equation describing the motion of a single level set in a higher dimensional function (Fig. 39).

The zero level set is evolving with the speed function  $F = \pm 1 - \varepsilon \cdot \kappa$ , where  $\varepsilon$  is a constant and  $\kappa$  the curvature. In two dimensions the curvature is described with the following equation:

$$\kappa = \frac{\gamma_{xx}\gamma_y^2 - 2\gamma_x\gamma_y\gamma_{xy} + \gamma_{yy}\gamma_x^2}{(\gamma_x^2 + \gamma_y^2)^{3/2}} \quad (30)$$

and equivalently in three dimensions the mean curvature  $\kappa_{Mean}$ :

$$\kappa_{Mean} = \frac{\left\{ \begin{array}{l} (\gamma_{yy} + \gamma_{zz})\gamma_x^2 + (\gamma_{xx} + \gamma_{zz})\gamma_y^2 + (\gamma_{xx} + \gamma_{yy})\gamma_z^2 \\ - 2\gamma_x\gamma_y\gamma_{xy} - 2\gamma_x\gamma_z\gamma_{xz} - 2\gamma_y\gamma_z\gamma_{yz} \end{array} \right\}}{(\gamma_x^2 + \gamma_y^2 + \gamma_z^2)^{3/2}} \quad (31)$$

The curvature  $\kappa$  acts in this case as a regularization term. It hinders the level set moving into narrow places and stabilizes it with respect to noise. The uniform extraction (contraction) in the direction of the normal with speed 1 (-1), depends on the sign of the speed function.

So far the curve is moving as the function of its own curvature and normal vector. In order to detect the boundaries of the object, a stopping criterion for the snake has to be determined. It can be a function of the gradient map of the image, as well as through user-interaction influenced. The gradient is the indicator for the existence of an edge, which characterizes the boundaries of an object. The corresponding weighting function  $g$  can be chosen in the following way:

$$g = \frac{1}{1 + |\nabla G_\sigma * I|}, \quad (32)$$

where the expression  $\nabla G_\sigma * I$  denotes the gradient of the image  $I$  convoluted with a Gaussian filter with variance  $\sigma$ . The values of the weighting function are almost equal to one for small gradients and approximately zero otherwise. The normal and the curvature of the level set are weighted, resulting in the following speed function:

$$F = g \cdot (\pm 1 - \varepsilon \cdot \kappa) \quad (33)$$

and the equation to be solved:

$$\phi_t + g \cdot (\pm 1 - \varepsilon \cdot \kappa) \cdot |\nabla \phi| = 0 \quad (34)$$

Especially in noise hampered images the gradient information becomes insecure and misleading. Nevertheless the gray value still contains the whole image information, which can also be used, resulting generally in better segmentation results. An appropriate method for extracting the object information, without depending on the local mean gray value is contrast equalization. The equalized image  $I_p$  is calculated by dividing a high passed filtered version  $HP\{I\}$  with low passed filtered version  $LP\{I\}$  of the original image  $I$ :

$$I_p = \frac{HP\{I\}}{LP\{I\}} \quad (35)$$

Instead of the gradient, the gray values of the equalized image are used for calculating the weighting function.

#### 4.1.1 Discretization Scheme

The motion equation (eq. 34) is hyperbolic and consequently can not be discretized by common techniques e.g. central differences. It can be proven that the discretization scheme is going to become unstable in finite iterations. The discretization stencil below is given in Sethian (1996). In the 2D case the following numerical approximation for the gradient is applied:

$$|\nabla \phi| = \sqrt{\min(0, D^{+x}\phi)^2 + \max(D^{-x}\phi, 0)^2 + \max(D^{-y}\phi, 0)^2 + \min(0, D^{+y}\phi)^2} \quad (36)$$

In the 3D case the stencil looks similar, with the additional  $z$  components:

$$|\nabla \phi| = \sqrt{\min(0, D^{+x}\phi)^2 + \max(D^{-x}\phi, 0)^2 + \max(D^{-y}\phi, 0)^2 + \min(0, D^{+y}\phi)^2 + \min(0, D^{+z}\phi)^2 + \max(D^{-z}\phi, 0)^2} \quad (37)$$

### 4.1.2 Initialization of the Segmentation Curve

The segmentation result is very sensitive to the initial snake conditions. Therefore the start position of the snake has to be determined accurately. The procedure works as follows: Usually a user-defined curve (or a user-defined point) is marked outside (or inside) of the feature to be segmented. The snake is then evolved from this start-conformation as a function of its normal, curvature, and the weighting function  $g$  of the image. It should converge and stop at the boundary of the feature or in case of several interesting features to break or merge in order to produce segmentation islands indicating different segmented features.

## 4.2 Missing Wedge Compensation with a modified Discretization Stencil

In 3D electron microscopy additionally to the low SNR the missing wedge influence has to be considered. The effect is that the gradient parallel to the  $z$ -axis in real space is zero and the level set weighting function no longer consists of a stopping-criterion in that direction any more.

Consider the following experiment: A performance simulation of the snake on a holey sphere, degraded with the missing wedge. The sphere simulates a vesicle in real electron microscopic images. Due to the missing information in the  $z^*$  axis, the edges of the sphere smooth out, by decreasing the Eulerian angle  $\vartheta$  ending in totally smoothed out poles (Fig. 40). The application of a hard threshold in a surface-rendering algorithm visualizes the following shape:

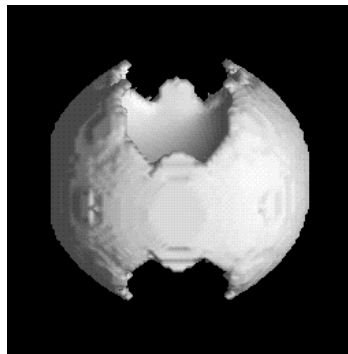


Fig. 40. Isosurface of a hole sphere with missing wedge.

The snake is initialized with the ideal start position for the detection of the object (in this case a sphere). After iterating the algorithm for a finite time the object boundary is approached and the image properties block the further evolution. With further application of the algorithm, the snake evolves into the gap of the sphere, through the poles (due to the missing wedge) and segments only the periphery. Further on the snake collapses to a toroidal structure and disappears, due to the high curvature of the boundaries, i.e. at the end no segmentation exists, even though the detectable object was noise free and with well-defined boundaries.

The reason why this happens is the vertical force component of the normal. The snake should move inwards (or outwards) in the z-direction only as a function of the curvature, so that the poles get covered but not penetrated. Therefore the evolution depends from angle of the normal to the z-axis. The snake moves in the orientation of the z-axis only as a function of the curvature and the vertical forces are set to zero. The PDE is modified accordingly and the equation of motion of the describing the movement of the snake can be written in the following way:

$$\phi_t + g \cdot (\pm |\nabla \phi|_z - \varepsilon \cdot \kappa \cdot |\nabla \phi|) = 0 \quad (38)$$

Where

$$|\nabla \phi|_z = \sqrt{\min(0, D^+ \phi)^2 + \max(D^- \phi, 0)^2 + \max(D^- \phi, 0)^2 + \min(0, D^+ \phi)^2} \quad (39)$$

Through this modification the segmentation algorithm is suitable for 3D electron microscopic images. It still does not work on a global basis, but considering the recent advances in virtual reality and visualization techniques the user interaction facilities are enhanced and so applicability grows. The user can define several points inside the 3D image, observe their evolution, and eventually modify the process interactively. In this way small shapes can be detected inside extremely complicated constructs (Fig. 42) and a semi automated segmentation can be facilitated.

### 4.3 Performance Study of Snake Segmentation

For a performance study, the level set segmentation algorithm has been applied on a large variety of 2D and 3D electron microscopic images. There is a major difference for 2D scenes and 3D images. In 2D scenes the user can interact with the snake in order to push it in certain directions in order to improve the segmentation or for example to hinder it inserting in regions he does not want to separate from the final result. User interaction appears to be necessary with this segmentation algorithm, due to the high sensibility of the algorithm from the start initialization as well as from the local parameter choice. This user interaction becomes a severe problem in the 3D case, due to the insufficient visualization equipment. The 3D image becomes very complex and several movements and temporal snake segmentations are hard to follow.

#### 4.3.1 Two Dimensional Electron Microscopic Data

The segmentation algorithm is first applied on a 2D EM-image of isolated and negatively stained 26S proteasomes (Fig. 41a). The exemplary image that is characterized by a high contrast contains a large variety of differently shaped particles. The idea is to let a level set evolve and create “islands” in which the particles are included with relatively high probability. The further analysis e.g. classification can be made a posteriori by correlation based techniques such as matched filter. The first initialization of the level is in this case a square at the outer boundary of the image. The

level set evolves towards the inner part of the image mainly through the force of the normal (Fig. 41b-c). Due to the small size of the particles the curvature parameter  $\varepsilon$  is chosen very small in order not to hinder the level set segmenting small feature.

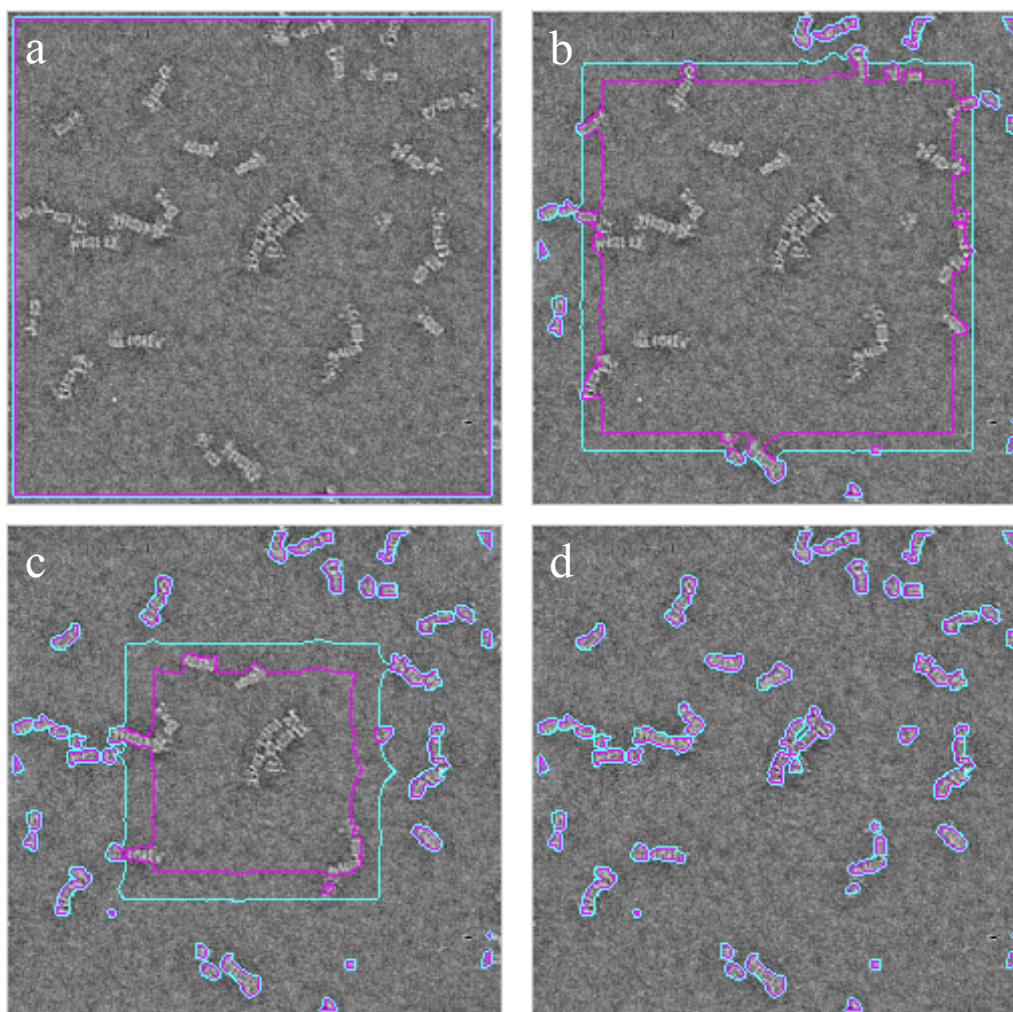


**Fig. 41.** Segmentation of single 26S proteasomes. (a) Start initialization of the snake, (b) evolution after 200 iteration, (c) after 400 iterations, (d) final segmentation. The colors represent different evolution steps (in order to improve the visualization).

The final segmentation (Fig. 41d) is very satisfactory, as several contours of the particles have been detected. The segmentation result can be used as an “edge map” for a curvature based method (gradient-dependent mean curvature motion). The different islands can then be separated and classified, as a function of their size and shape.

The second example is a xy slice through an electron tomographic reconstruction of T5 viruses attached to proteoliposomes. The level set should approach the boundaries of the viruses, including the virus tails and proteoliposomes, as accurately as possible in order to avoid noise distortions during the visualization. In this example the initialization of the snake is not automatic, but through user interaction several points around the object of interest are set (Fig. 42a). Compared with the former example the SNR is

considerably lower, and therefore the boundaries are interrupted. In order to produce an optimal segmentation the curvature parameter has to be very large.

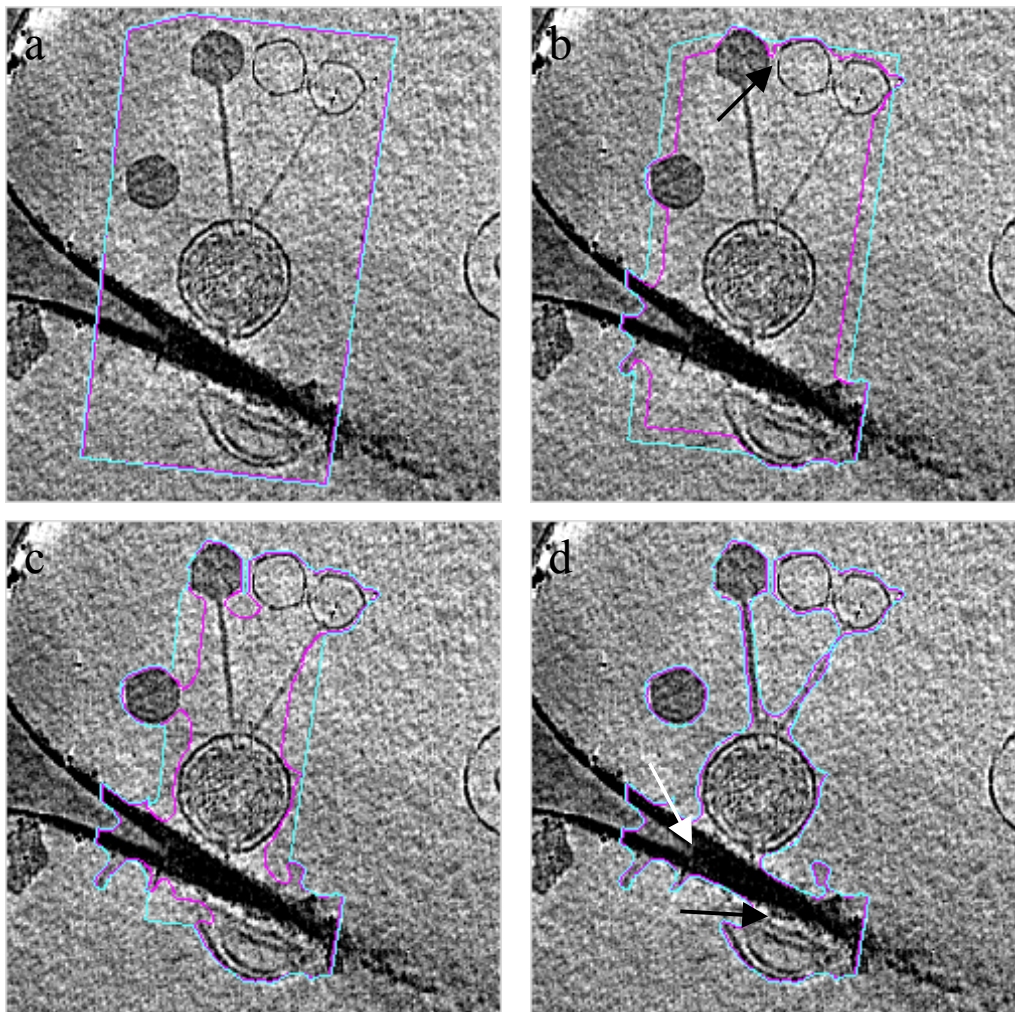


**Fig. 42.** Xy-slice from a tomographic reconstruction of T5 viruses attached to proteoliposomes. (a) Start initialization of the level set (Bright curve surrounding the viruses), (b) progress after 200 iterations; arrow demonstrates the place where the level set was forced (by user interaction) to insert into the hole to segment the empty space between the two virus tails. (c) Progress after 400 iterations and (d) final segmentation result. Black arrow notes the place where a separation would be desired. White arrow denotes the carbon bridge which remains in the segmentation result.

After the start initialization (Fig. 42a.) the level set evolves inwards. Due to the high curvature parameter it is unable to insert in the empty space between the two virus tails. In order to force a segmentation result in this space the curvature is explicitly set to zero locally. A different solution would be to place a second level set in this space, which should evolve in the outward direction. After 800 iterations the level set stabilizes at the boundaries of the objects. The approach is quite satisfactory; nevertheless the carbon film can not be separated from the virus-proteoliposomes complex.

The third and last 2D example is a segmentation of an ice embedded *Pyrodictium abyssi* cell. In this case the separation of the cell out of the background is desired. In Fig. 43a a xy-slice through the 3D reconstruction and the start initialization of the level set are presented. In the image the cell, some extracellular vesicles, and a canulla are clearly visible. The extracellular vesicles are surrounded by several small proteins, which make

the boundary very rough. The boundary of the cell has an excellent SNR, nevertheless at some places it is smoothed out, or interrupted due to cellular interactions. With the start initialization of the snake the canulla is avoided (Fig. 43a), which would block the further evolution of the snake.

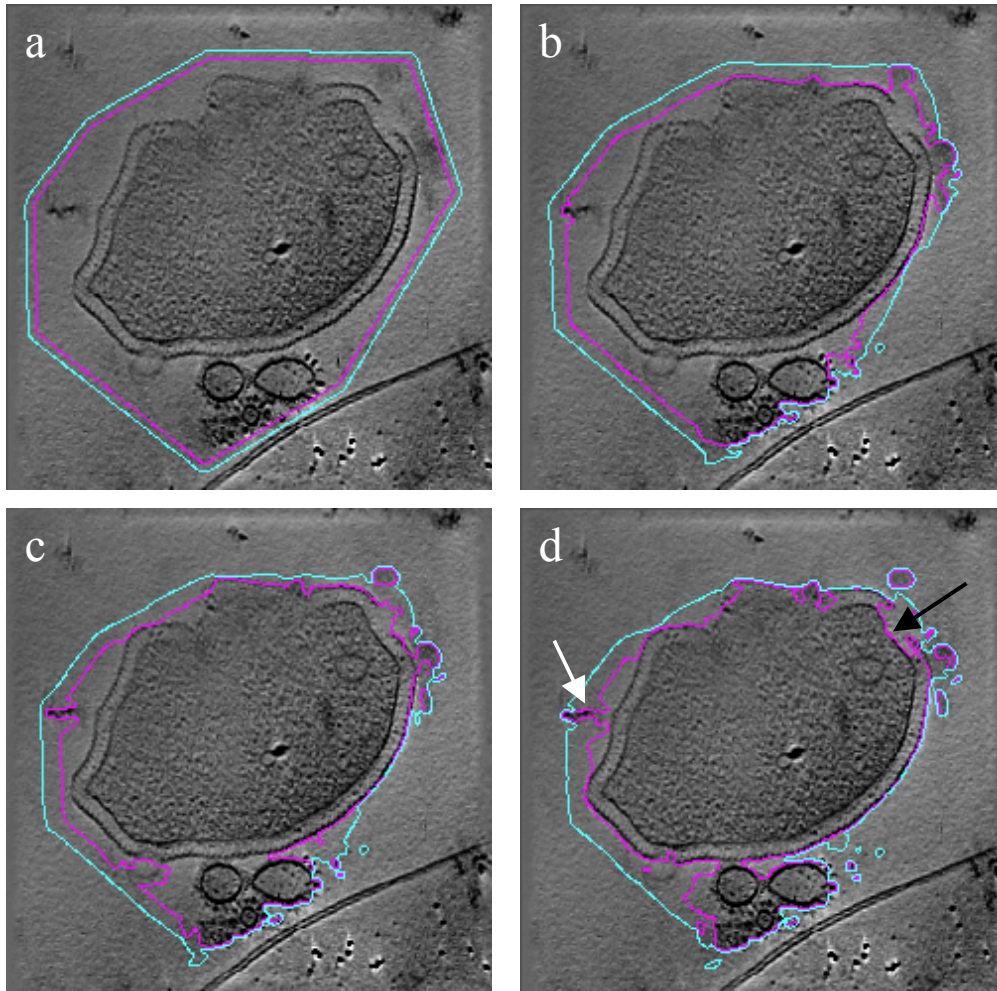


**Fig. 43.** Xy slice from a 3D tomographic reconstruction of a *Pyrodictium abyssi* cell. (a) Start initialization of the level set, (b) evolution after 200 iterations, (c) after 400 iterations and (d) final segmentation. Black arrow shows the place where the level set inserts into the membrane and jeopardizes the good segmentation. White arrow points to a segmented feature, which is obsolete.

The segmentation result (Fig. 43d) is not very satisfactory, as the snake did not detect most of the boundaries nicely. The extracellular vesicles could not be segmented from the rest of the cell. In the place where the outer boundary of the cell is missing, the curvature is not capable of hindering the level set inserting. With user interaction the result can be improved significantly. For this reason a different snake should be initialized, where the extracellular vesicles would be already excluded from the segmentation result as the force would be set to zero at several gaps at the membrane.

### 4.3.2 Simulations on 3D Synthetic Data

For the performance demonstration of the snake segmentation on 3D images the typical snake algorithm is applied on the synthetic sphere degraded with missing wedge, as well as the modified version. For a realistic segmentation a missing wedge from  $\pm 35^\circ$  has been used for degrading the sphere. The isosurface of this sphere is presented in Fig. 40. The poles of the sphere are smoothed out and do not appear in the isosurface presentation. The segmentation results of the original (Fig. 44a-c) and modified (Fig. 45) algorithm are presented.

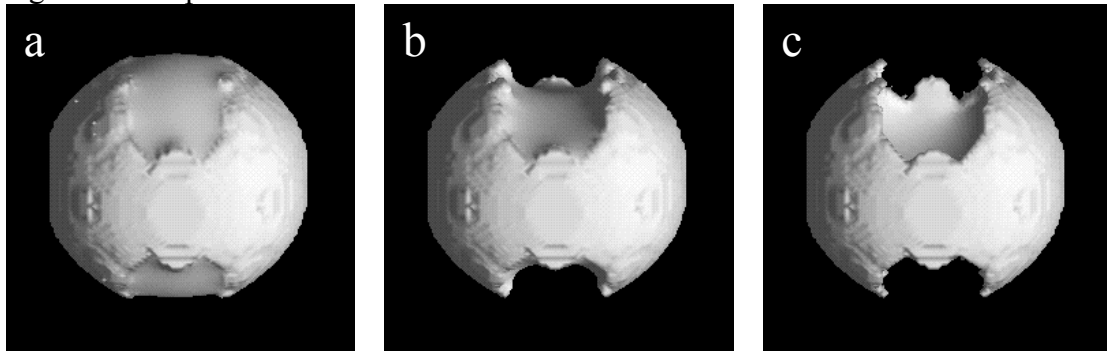


**Fig. 44.** Segmentation of a sphere with missing wedge. (a-c) present the evolution of the unmodified level set algorithm.

With the elimination of the force component in the z-direction the tops of the sphere appear flat, where in the other case they are not segmented at all (Fig. 44c). With this modification the algorithm becomes capable of segmenting the interior of a cell or organelle (Fig. 46-47).

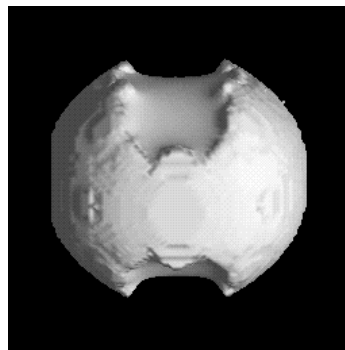


**Fig. 45.** Segmentation of the same sphere as in Fig. 44 with the modified level set algorithm. The missing information is not recovered, but the level set does not propagate into the interior of the sphere.

With this modification not only the segmentation of the exterior of the particle is facilitated, but due to the fact that gradient magnitude in the z-direction is very small the problem of bad segmentation would exist on every segmented feature.

### 4.3.3 Snake Segmentation of Three Dimensional Electron Microscopic Data

The 3D segmentation of an inside-out vesicle formed by mitochondrial inner membrane fragments represents a very challenging segmentation task, due to several difficulties,

including small features, which should be included in the segmentation result, as well as large scale missing wedge and therefore disappeared poles (Fig. 46). The interesting features in this 3D image are the macromolecular structures periodically located at the outer side of the vesicle membrane. In order to be able to visualize them several other high contrast features as part of a mitochondrion should be segmented out.

The first initialization of the level set was a cube surrounding the vesicle. The level set propagates towards the vesicle and produces the blue surrounding envelope. The level set does not propagate in the interior of the vesicle. Additionally all small features, probably corresponding to proteins, are included in the final segmentation (Fig. 46).

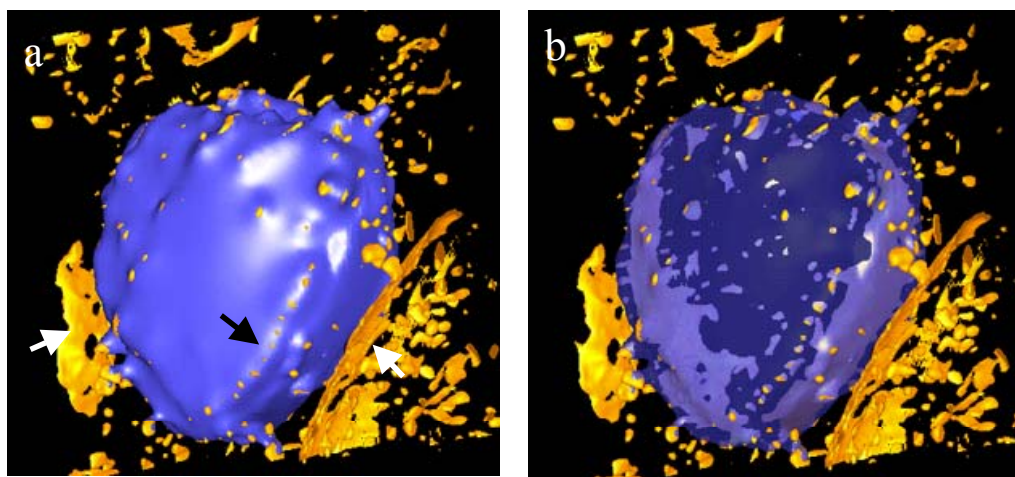


**Fig. 46.** Isosurface presentation of the inside-out vesicle. In blue color ( (b) transparent and (a) not) the segmentation result is presented. The white arrows point to the features which should be separated from the inside-Out vesicle. The black arrow points to the macromolecules attached to the vesicle membrane, which should be included in the segmentation result.

The same performance can be demonstrated at a *Pyrodictium cell*. In this case the cell is filled with several small structures (Fig. 47). The level set does not propagate again into the intracellular space (Fig. 47b), and the information inside can be further processed.

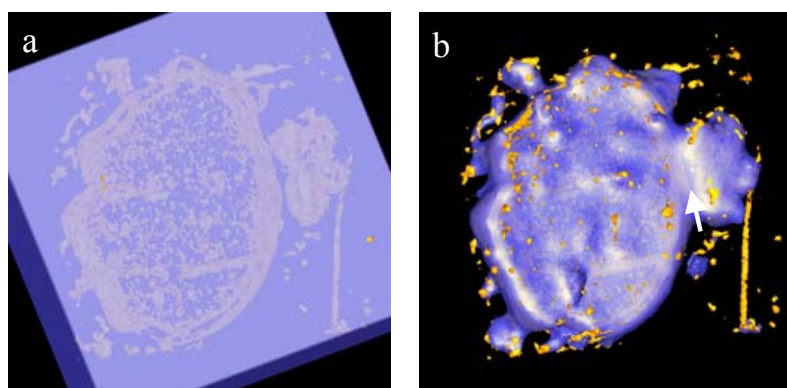


**Fig. 47.** Segmentation of a *Pyrodictium abyssi* cell. (a) Start conformation of the 3D-snake (cube) and (b) Final segmentation result. The snake did not insert in the intracellular space and the structural features (white dots) could be included in the segmentation. In the segmentation result the extracellular vesicles could not be separated from the rest of the cell (arrow).

The last example is the segmentation of T5 Viruses attached to proteoliposomes. In this case the snake is not capable of detecting the interesting biological features and includes

in the segmentation also the carbon foil (as in the 2D case) (Fig. 48). The segmentation can not be improved in this case, even with user interaction, because all the features lie very dense in the volume.

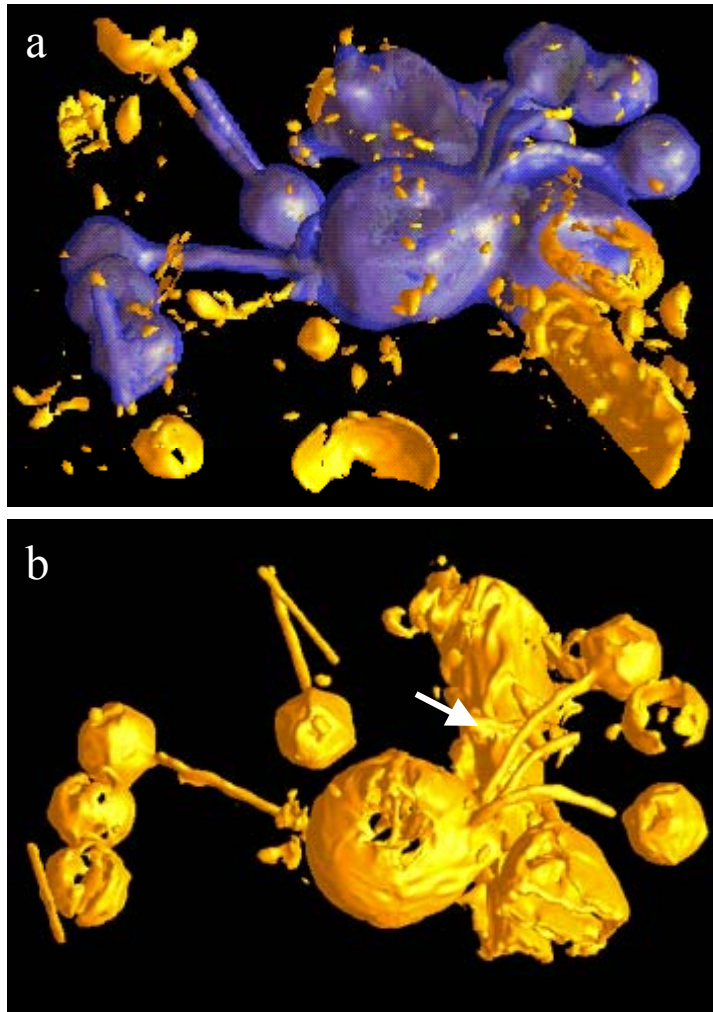


**Fig. 48.** Segmentation result of T5 Viruses attached to proteoliposomes. The carbon foil could not be separated from the segmentation result (white arrow).

#### 4.4 Discussion

Segmentation based on the level set technique is a very useful tool and a promising and exciting line of research in the near future. On the contrary to the conventional “snake” techniques, arbitrary boundaries can be detected and due to the level set technique the snake can split and merge without mathematical instabilities. Nevertheless the segmentation results still depend strongly on the initial conditions and usually require strong user interactions. The level set method can not be used in an automated way for global 2D and 3D image segmentation. The result in this case would be at best similar to simple thresholding schemes.

The most important application is in the field of 3D visualization and virtual reality, where a strong user- data interaction is necessary and desired. Several level sets can then

be placed in the interior or exterior of structures and are capable of revealing their local structure. The parameters can then be adjusted locally and a separation of different features is simple. In this case the level sets can replace different segmentation tools e.g. splines, cut/crop tools or user 2D segmentations.



## Chapter 5

# Multidimensional Image Segmentation with Eigenvectors

Image segmentation techniques can be classified into two broad families: the contour-based and the region-based approaches. Contour-based approaches, such as level sets, usually start with a first stage of edge detection, followed by a linking process towards a detectable boundary. Region-based approaches try to find partitions of the image pixels into sets corresponding to coherent image properties. The major difference between these techniques is the decision criterion: local vs. global. Contour-based techniques make local decisions (e.g. merge/split, stop/evolve), that can be proven premature. Region-based techniques make the decision by defining a global objective function. The advantage thereby is that decisions are made when information from the whole image is taken into account at the same time.

In contour-based approaches, the first step of edge detection is done locally. Subsequently efforts are made to improve results by a global linking process that seeks to exploit curvilinear continuity. In this sense the edge/no edge decision is made too early. To detect extended contours of very low contrast features a small threshold has to be set for the edge detector, which causes random edge segments to be found all over the image, making the task significantly harder.

The use of eigenvectors for segmenting 2D and 3D images is a new and exciting approach in this field. Different from the level set method, where a boundary is pushed towards an object, this technique takes the whole image into account and separates it into several regions, which can be used to distinguish the different objects from each other. The traditional method of object separation is histogram thresholding, commonly used for surface rendering. Unfortunately there are many images in which no clear-cut of the histogram peaks corresponds to distinct objects in the image. With the eigenvectors a foreground/background separation is obtained, therefore a parameter-defined cost function is minimized and the dominant feature is separated from the rest. By further applying the algorithm a tree-segmentation is achieved.

Humans use a large variety of different criteria to segment images, e.g. similarity, proximity, continuity, symmetry. In the field of electron microscopy the observer usually searches for a known shape or multiple occurring shapes to propose some sort of segmentation. The separation criterion is the gray value and contrast difference between the feature and the surrounding environment. The approach suggested here has the advantage of being able to integrate a large variety of different criteria, e.g. texture

detectors, energy formulations, gradient information, etc. Nevertheless the gray value information and the distance remain the most reliable parameters the segmentation is based on. Additionally, the energy can be taken into account to improve the segmentation result.

## 5.1 Algorithm

### 5.1.1 Graph theoretical approach

The image is considered as a weighted, undirected graph  $G = (V, E)$ , where each pixel corresponds to a node  $V$  and an edge  $E$  is formed between every pair of nodes. The weight  $w(i, j)$  of each edge is a function of the similarity between nodes  $i$  and  $j$ . The segmentation procedure partitions the whole set of nodes  $V$  into disjoint sets  $V_1, V_2, \dots, V_m$ , where some measure of the similarity among the vertices in a set  $V_i$  is high and across different sets low. The common criterion for splitting a graph  $G$  into two disjoint sets  $A, B, A \cup B = V, A \cap B = \emptyset$  is the ‘‘cut-criterion’’. The dissimilarity is measured by the sum of all connections between the sets  $A$  and  $B$ .

$$cut(A, B) = \sum_{u \in A} \sum_{v \in B} w(u, v) \quad (40)$$

The cut-criterion favors cutting small sets of isolated nodes in the graph. Shi and Malik (1997) suggested the extension of this criterion, in order to avoid this effect and improve the segmentation procedure. They introduced the *normalized-cut* criterion:

$$Ncut(A, B) = \frac{cut(A, B)}{asso(A, V)} + \frac{cut(B, A)}{asso(B, V)}, \quad (41)$$

where

$$asso(A, V) = \sum_{t \in V} \sum_{u \in A} w(u, t) \quad (42)$$

is the total connection weight of the nodes in the group  $A$  to  $V$ . In a similar way they defined the normalized association *Nasso* within groups for a given partition:

$$Nasso(A, B) = \frac{asso(A, A)}{asso(A, V)} + \frac{asso(B, B)}{asso(B, V)} \quad (43)$$

The weight minimization of the connections between the two groups  $A$  and  $B$  correspond to the separation of the image into two distinct groups.

### 5.1.2 Construction of the Affinity Matrix

The most essential feature for the algorithm is the affinity matrix  $\mathbf{W}$  containing the connection weight  $w_{i,j}$  and equivalently the similarity between two nodes  $i$  and  $j$ . It is

usually a function  $f$  of different features, e.g. gray value, gradient, color, texture, energy, etc.

$$w_{i,j} = f(i, j) \quad (44)$$

The electron microscope images (in 2D and 3D) are parallel projections of the density distribution of the sample, which is recorded in the gray value distribution of the image. Consequently it should influence the affinity matrix significantly. The geometric distance of the pixels to each other appears also to be a very natural and important criterion for segmenting an image. A further facilitating feature, which can be implemented in the affinity matrix, is the energy. Thereby the energy for connecting two pixels with each other is calculated. The advantage is that information contained in the different nodes between these two nodes, is used. Even though texture appears to be a very significant segmentation criterion in real world images, in electron microscope images significant texture regions do not appear often. The affinity matrix, used in the segmentation procedure, is a superposition of three components:

(a) the gray value component  $w_I$ :

$$w_I(i, j) = \exp\left(-\left(I_i - I_j\right)^2 / \alpha_I\right), \quad (45)$$

(b) the Euclidean distance component  $w_d(i, j)$

$$w_d(i, j) = \exp\left(-d(x_i, x_j) / \alpha_d\right), \quad (46)$$

and (c) the energy component  $w_e(i, j)$ :

$$w_e(i, j) = \exp\left(-\sum_{L_{ij} \cap A} \nabla I^2 / \alpha_e\right) \quad (47)$$

Where  $L_{ij} \cap A$  is the set of elements which lie on a line connecting the pixels  $i, j$ . The parameters  $\alpha_I, \alpha_d, \alpha_e$  represent the different affinities. Their setting determines the weight balance of the different components in the affinity matrix.

The different components sum to following affinity-matrix element  $w(i, j)$ :

$$w(i, j) = w_I(i, j) * w_d(i, j) * w_e(i, j) \quad (48)$$

Presently realizations use the gray value  $w_I(i, j)$  and the distance  $w_d(i, j)$  as they are the most reliable parameters. The gradient contains high frequency information, which is for high degraded data misleading. For noise free data the energy formulation is mainly used because of the following advantages:

- 1) Pixels with the same gray value separated by a thin line would be classified in the same group, as pixels not separated by the line.
- 2) High contrast thin edges are similarly weighted as bright edges with low contrast. With the energy formulation high contrast edges are higher weighted, as they usually determine defined boundaries.

Having defined the graph partition criterion to be minimized as well the construction of the affinity matrix the optimal partition should be computed.

### 5.1.3 Algorithms for Graph Partition

Shi and Malik proposed to solve the minimization of the *normalized-cut* criterion as an eigenvector problem (SM algorithm). They have proven that the second smallest eigenvector is the solution for minimizing the connections between the two subsets. This is in coincidence with the theorem of Fiedler, which states that the second smallest eigenvector separates the graph into two subgraphs, so that the connections between these subgraphs are minimized, which equivalently means that the connection in the graph is maximized. Minimization of the *normalized-cut* criterion can be achieved by solving the generalized eigenvalue system (Shi et al. 1997):

$$(\mathbf{D} - \mathbf{W})\mathbf{y} = \lambda\mathbf{D}\mathbf{y} \quad (49)$$

Where  $\mathbf{y}$  the solution of the problem,  $\mathbf{W}$  is the affinity matrix and  $\mathbf{D}$  a diagonal matrix. The element  $d(i, i)$  of the matrix  $\mathbf{D}$  is the row sum of the elements of the affinity matrix  $\mathbf{W}$ :

$$d(i, i) = \sum_j w(i, j) \quad (50)$$

Equation 49 can be rewritten in the following form:

$$\mathbf{D}^{-0.5}(\mathbf{D} - \mathbf{W})\mathbf{y} = \lambda\mathbf{D}^{0.5}\mathbf{y} \quad (51)$$

By substituting  $\mathbf{z} = \mathbf{D}^{0.5}\mathbf{y}$ ,

$$\mathbf{D}^{-0.5}(\mathbf{D} - \mathbf{W})\mathbf{D}^{-0.5}\mathbf{z} = \lambda\mathbf{z}, \quad (52)$$

Which is a standard eigenvalue problem. The matrix  $\mathbf{D}^{-0.5}(\mathbf{D} - \mathbf{W})\mathbf{D}^{-0.5}$  is symmetric positive definit. Therefore all eigenvalues of this matrix are non-negative.

The eigenvector  $\mathbf{z}_0$  corresponding to the eigenvalue  $\lambda_0 = 0$  is:

$$\mathbf{z}_0 = \mathbf{D}^{0.5}\mathbf{1} \text{ or } \mathbf{y}_0 = \mathbf{D}^{-0.5}\mathbf{D}^{0.5}\mathbf{1} = \mathbf{1}, \quad (53)$$

because of  $\mathbf{D} \cdot \mathbf{1} = \mathbf{W} \cdot \mathbf{1}$ , where  $\mathbf{1}$  is a vector of ones with the dimensionality of  $\mathbf{W}$ . As all the eigenvectors are perpendicular to each other:

$$0 = \mathbf{z}_1^T \cdot \mathbf{z}_0 = \mathbf{y}_1^T \mathbf{D}\mathbf{1}, \quad (54)$$

where  $\mathbf{y}_1$  is the solution of the *normalized-cut* problem, which has to fulfill this side condition.

Instead of using the second smallest eigenvector the matrix can be transformed in the following way:

$$\mathbf{D}^{-0.5}(\mathbf{D} - \mathbf{W})\mathbf{D}^{-0.5}\mathbf{z} = (\mathbf{E} - \mathbf{D}^{-0.5}\mathbf{W}\mathbf{D}^{-0.5})\mathbf{z} = \lambda\mathbf{z} \quad (55)$$

With  $\mathbf{E}$  the identity matrix. With further calculations eq. 55 becomes:

$$\mathbf{Ez} - \lambda \mathbf{z} = \mathbf{D}^{-0.5} \mathbf{W} \mathbf{D}^{-0.5} \mathbf{z} \quad (56)$$

The normalized matrix  $\mathbf{N} = \mathbf{D}^{-0.5} \mathbf{W} \mathbf{D}^{-0.5}$  is defined and eq. 56 can be written in the following form:

$$\mathbf{Nz} = (1 - \lambda) \mathbf{z} \quad (57)$$

Normalization lemma: Let  $\mathbf{v}$  be an eigenvector of  $\mathbf{N}$  with eigenvalue  $\lambda$ . Then  $\mathbf{D}^{-0.5} \mathbf{v}$  is a generalized eigenvector of  $\mathbf{W}$  with eigenvalue  $1 - \lambda$ . The vector  $\mathbf{D}^{0.5} \mathbf{1}$  is an eigenvector of  $\mathbf{N}$  with eigenvalue 1.

A simpler way of exploiting the segmentation information included in the affinity matrix is the algorithm of Scott and Longuet-Higgins (SLH algorithm). The largest  $k$  eigenvectors  $\mathbf{v}_1, \mathbf{v}_2, \dots, \mathbf{v}_k$  of the affinity matrix  $\mathbf{W}$  are calculated and the matrix  $\mathbf{V} = [\mathbf{v}_1, \mathbf{v}_2, \dots, \mathbf{v}_k]$  is created. The rows of  $\mathbf{V}$  are normalized so that they have unit Euclidean norm. The segmentation information can be embodied in

$$\mathbf{Q} = \mathbf{V} \cdot \mathbf{V}^T \quad (58)$$

Ideally  $q(i, j) = 1$ , if  $i$  and  $j$  belong to the same group and zero otherwise.

The combination of both algorithms has proven to be better than each one on its own. As Shi and Malik noticed the solution of their algorithm is not necessarily the correct partition of the affinity matrix. In the contrary, with the use of the first  $k$  eigenvectors (SLH algorithm) the correct solution is guaranteed. After testing of both algorithms the results after using the normalized matrix, where significant better. Additionally the SLH algorithm performed similar to the SM algorithm. Consequently the normalized affinity matrix from the Shi and Malik algorithm is used, combined with the SLH algorithm. The similarity of the algorithms is the use of the largest eigenvectors of the affinity matrix. The main differences are which eigenvectors to look at and whether to normalize the affinity matrix or not (Weiss 1999).

#### 5.1.4 Implementation of the Algorithm

The implementation of the algorithm is not trivial, especially in the 3D case. The affinity matrix  $\mathbf{W}$  consists of  $N^2$  elements (full version), where  $N$  is the number of pixels/voxels in the image that should be segmented. This would make the algorithm totally useless due to the huge amount of memory resources needed. Therefore a window with a width  $R$  is used. In this case it is not the distance from every element to the rest of the affinity matrix that is calculated but only the distance to the next neighbors. The affinity matrix then has  $N \cdot R^2$  nonzero elements in 2D images and  $N \cdot R^3$  in 3D images. In this case a sparse matrix representation is of great advantage. The calculation of the eigenvectors is then performed with the Lanczos algorithm.

In general after the first calculation of the eigenvectors the desired feature is not perfectly segmented. In this case the first eigenvector is separated into two parts (usually

by a threshold scheme) and the segmentation procedure is applied again to each part separately. Fiedler (1975) has proven that the third eigenvector is the connection-cost minimizing criterion for the second eigenvector. One could then use the segmentation information contained in the third eigenvector for further partitioning of the image. Nevertheless in practice the new calculation of the eigenvectors has been proven to be more efficient.

## 5.2 Segmentation Results

The current goal of electron tomography is to identify macromolecular structures in a cellular context. Therefore one needs to scan the whole tomographic volume with appropriate references in order to determine a possible occurrence of a macromolecule by means of cross correlation. Segmentation techniques can be applied to make a foreground/background separation or a cell/environment (ice, carbon foil, gold bead, etc.) separation in order to reduce the size of the 3D image to be scanned. The concept is to downsample the tomographic reconstruction by a factor of two to three, segment the interesting feature and then apply the 3D image scan.

The second and probably most important field of application of segmentation algorithms is the separation of the 3D image into distinct groups with similar properties e.g. gray value. The separate presentation of the distinct areas containing structural features improves the visualization significantly. Usually the user is forced to segment the features of interest manually. Apart from the subjective influences of this technique the procedure is very time consuming and impractical to perform, especially when interactive real-time segmentation is required during the visualization procedure. Nevertheless for simple 3D images and distinct features manual contouring remains a very common tool for improving the visualization. Although the user is able to separate distinct features from their environment the invested work becomes immense if several compartments of the cell or organelle need to be separated. Manipulations of the segmentation result in order to test small modifications are not possible. The user has to define the place of interest every time explicitly, segment it by hand, and continue with the visualization. An automatic segmentation tool would be of tremendous help.

### 5.2.1 2D Segmentation

The first example presenting the performance of this segmentation technique on 2D images is a xy-slice from the tomographic reconstruction of a *Pyrodictium abyssi* cell (Fig. 49a). An ideal segmentation should separate the cell from the extracellular vesicles on the right side of the image and eventually also from the canulla. In order to improve the segmentation result, the image has been first denoised with nonlinear anisotropic diffusion (Fig. 49b). The segmentation procedure is very sensitive to noise and thus denoising is necessary. Simple denoising, obtained with techniques like lowpass or median filtering produce results equivalent to more complex ones.

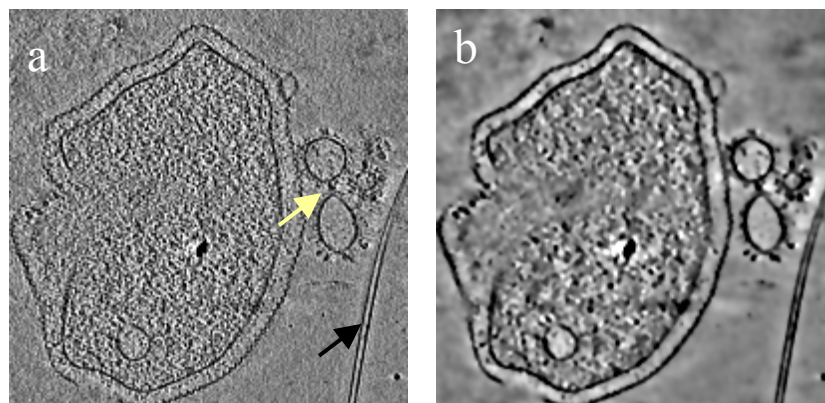


**Fig. 49.** Central xy-slice through a tomographic reconstruction of a *Pyrodictium abyssi* cell; (a) original slice and (b) slice denoised by nonlinear anisotropic diffusion. The white arrow points to the extracellular vesicles and the black arrow points to the canulla.

The inspection of the segmentation results confirms the foreground/background separation for which this technique has been designed (Fig. 50). The second eigenvector of the affinity matrix consists of bright gray values at the area covered by the and darker values everywhere else (Fig. 50a). The contour of the cell is precisely defined (See also red contour in Fig. 51). The cell can then be separated from the rest of the environment with a simple thresholding scheme.

In order to separate the extracellular vesicles from the canulla and the background a new segmentation cycle is initialized, producing an unambiguous classification of the objects. By further segmenting of the cell the cell boundary (S-layer) can be separated as an independent feature (white and black lines in Fig. 50b). The whole segmentation procedure is presented in Fig. 50.

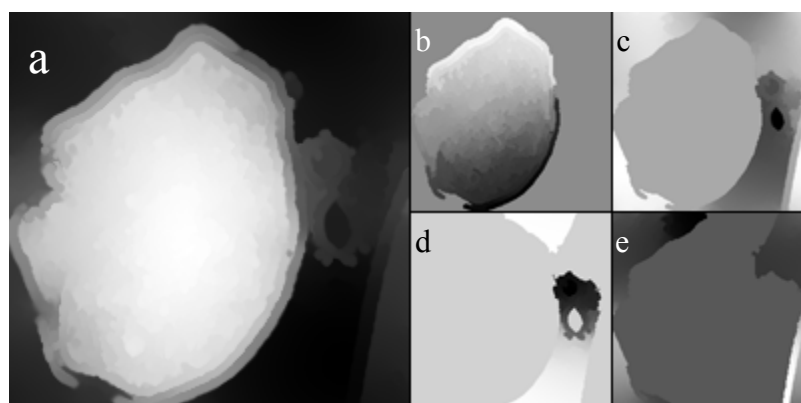


**Fig. 50.** Segmentation results of the *Pyrodictium abyssi* cell; (a) the original second eigenvector as produced from the combination of the SLH and SM algorithms. (b) Further segmentation of the bright values. In white and black the boundary (S-layer) of the cell is coded. (c) Segmentation of the darker values. The extracellular vesicles get separated from the ice, the canulla, and the background. (d) Final segmentation of the extracellular vesicles. (e) Final segmentation of the canulla.

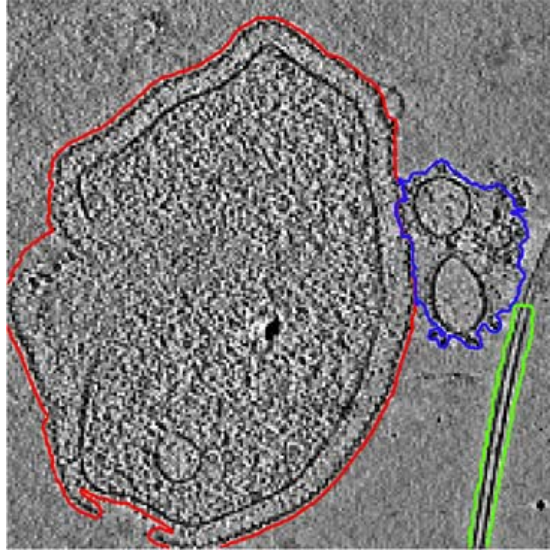


**Fig. 51.** Segmentation results in a combined form as contour plots. Every feature on the image could be unambiguously segmented. The red boundary represents the contour of the cell, the blue boundary the extracellular vesicles, and the green the canalla.

The second example is a xy-slice from a 3D reconstructed inside-out vesicle of a mitochondrion (Fig. 52a). The segmentation of this image is usually very difficult for conventional techniques, for the following reasons: The inside-out vesicle is located close to the mitochondrion and the top and the bottom side of vesicle are not defined, rather just indicated by the position of small particles (gray dots). Furthermore the vesicle is connected with several other features, with similar contrast, which should not be included in the segmentation result.

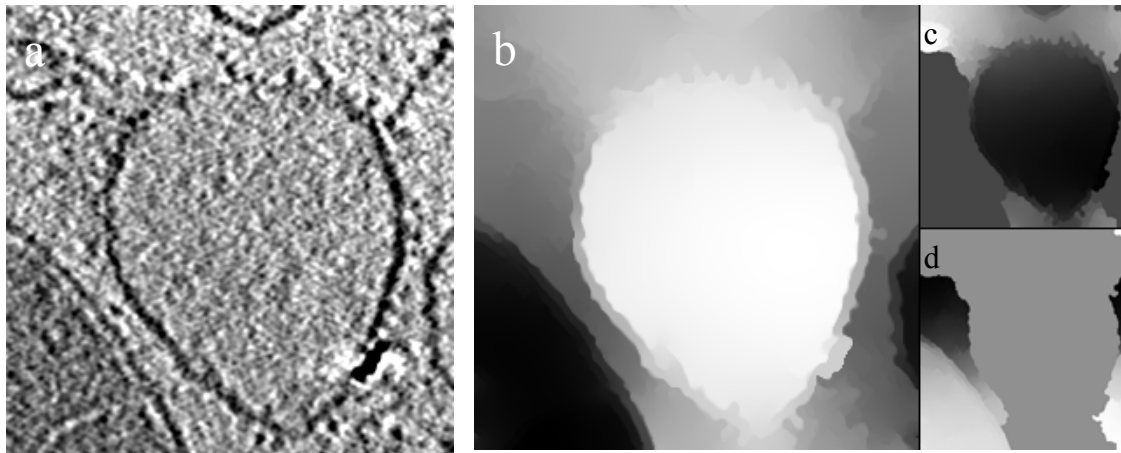


**Fig. 52.** Segmentation of an inside-out vesicle; (a) xy-slice from the original reconstruction, (b) the second eigenvector as calculated from the affinity matrix. The inside-out vesicle has clearly been separated from the rest. (c) Contour detection of the vesicle. (d) Separation of the mitochondrion from the rest.

In the presentation of the second eigenvector (Fig. 52b) four different gray-value classes can be distinguished. The bright part represents the interior of the inside-out vesicle. The gray field indicates the membrane and the different particles attached to the vesicle. The darker part is the whole background with all the different features. Finally the darkest

part is the mitochondrion next to the vesicle. In Fig. 53 contours of the segmentation result are presented. The segmentation result is very good. This performance is observed without any kind of a priori information about the vesicle.

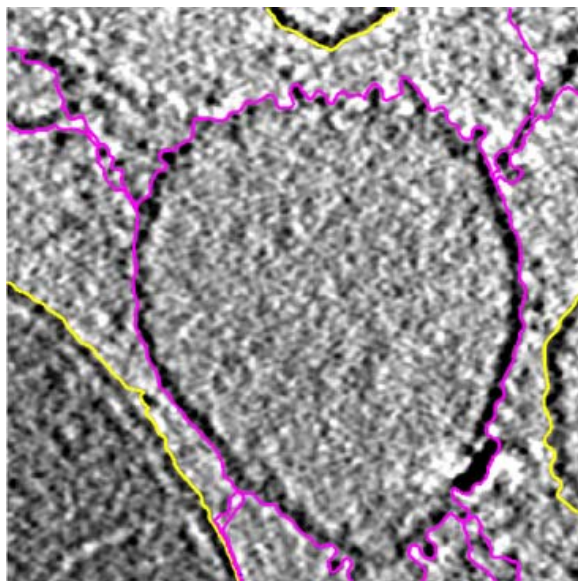


**Fig. 53.** Contour presentation of the segmentation of the inside-out vesicle. The purple line represents the segmentation of the outer membrane of the inside-out vesicle including several small objects around. The yellow line indicates the segmentation of the mitochondria and the other vesicles.

### 5.2.2 Segmentation of 2D Single Particle Images

A large application field, where the eigenvector segmentation technique can be a very helpful tool is automated single particle analysis. In order to achieve a resolution down to 0.8 nm several hundred thousand particles need to be collected. There has always been the need for an automation of this procedure. Therefore one has to record the images of the molecules with the microscope first. New developments in the field require an automated procedure for this task. The particle solution is applied to a quantifoil grid with several regularly spaced holes in a carbon film. Using an automated acquisition scheme the position of the holes is detected and an image of the molecules is recorded. The particles lying in the holes and not on the carbon foil have to be detected afterwards in order to produce a correct average. This segmentation technique is capable of separating ice and carbon in a very fast and reliable way, without any user interaction.

The performance of the segmentation is demonstrated in the following example. In Fig. 54 a 2D image of *drosophila* 26S proteasomes embedded in unsupported uranyl acetate/ice film is recorded. Typical of the 2D images is that a part of the carbon film has also been recorded. For further image analysis only the macromolecules in the ice are of interest, because they are not subjected to structural modifications. For the automated particle detection (e.g. MCM, cross correlation, etc.), segmentation has to exclude the molecules on the carbon foil. The segmentation with eigenvectors proves here to be a very fast and reliable technique. The original image from the microscope is

downsampled with a factor of four. A median filter is applied afterwards with a width of 3-5 pixels usually, in order to suppress some of the noise, by parallel preserving the edge properties. The resulting image is segmented with the second eigenvector. The parameters defining the affinity matrix can be set automatically. Usually a window function with 7 pixel width is used and the gray value affinity is 5% of the contrast of the processed image. The segmentation result is again ideal.

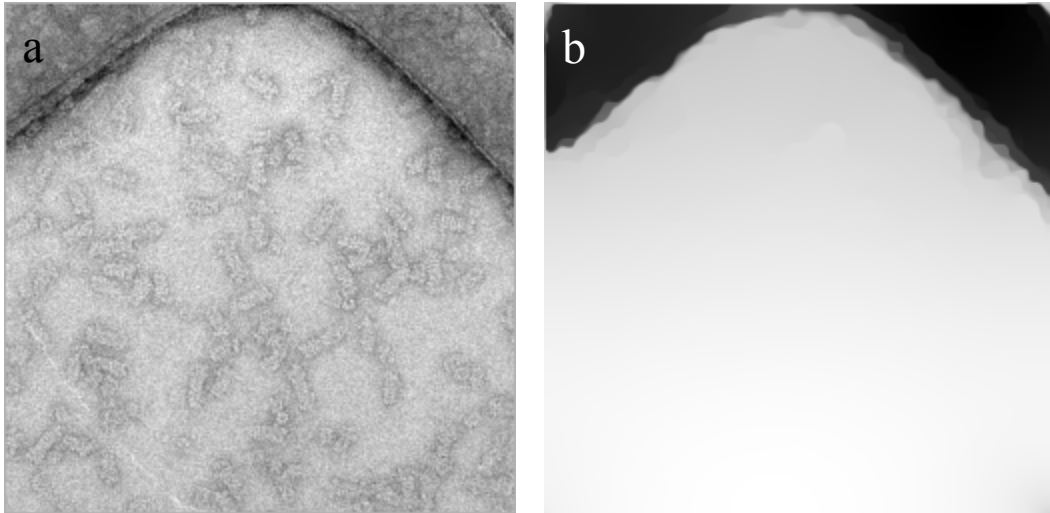


**Fig. 54.** Segmentation result on 2D electron microscopic images. (a) Original image with 26S proteasomes (b) Segmentation result.

The separation of the ice from the carbon can be made by simple thresholding of the histogram of the segmented image (Fig. 54b). In order to choose automatically the correct place (ice or carbon) an average of the gray values of each segmented area is calculated. Under the assumption that the ice is going to possess brighter gray values the correct place is chosen.

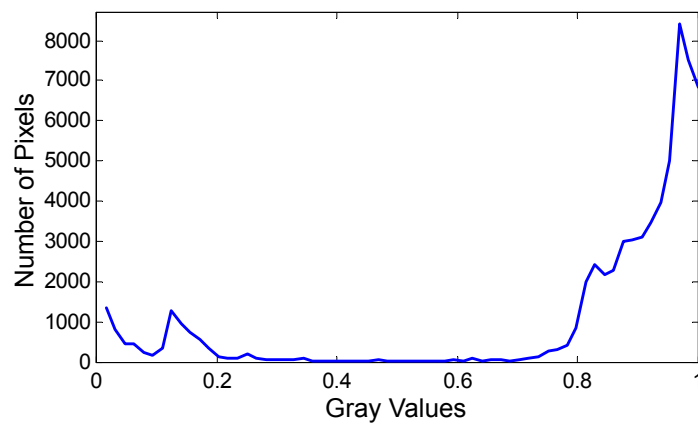


**Fig. 55.** Histogram of the segmentation result. The separation between darker and brighter gray-values is trivial.

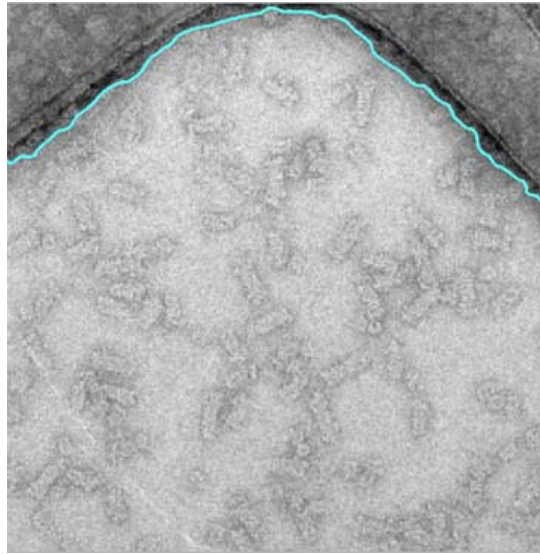


**Fig. 56.** Contour of the segmentation after using automated thresholding scheme.

### 5.2.3 Segmentation of 3D Images

The segmentation of the 3D images is from a mathematical point of view identical to the 2D case. Apart from the increased number of pixels involved in the segmentation, the window function is not 2D anymore but 3D. This increases the number of nonzero elements of the affinity matrix  $\mathbf{W}$  by a factor  $R$ , where  $R$  is the window size and respectively increases also the memory requirements.

In the electron tomographic reconstructions the information in the  $z^*$  direction in the Fourier space is missing, because the sample can not be tilted to high angles. This causes an effect of an anisotropic blurring, which is equivalent to a slower change of information in the  $z$ -direction. For this reason the 3D window for collecting the values can be chosen anisotropically or the number of slices used for the segmentation in the  $z$ -direction can be reduced. In the next examples the first option has been used.

The electron tomographic reconstruction of T5 viruses attached to proteoliposomes is the first example for 3D segmentation with eigenvectors. In order to improve the visualization the carbon film has to be separated from the rest. In this way a view from the “down” side of the volume should be possible. The task for this tomographic reconstruction was to visualize the virus tails as they penetrate the vesicle wall and inject their DNA inside the vesicle. The question arising thereby is, whether the virus tail penetrates the wall, or injects the DNA through a porin molecule lying in the vesicle wall. In the first case a density should be observed, due to the thickness difference of the tail and the DNA. Therefore a segmentation procedure is applied in order to remove the carbon foil and allow the visualization from every angle.

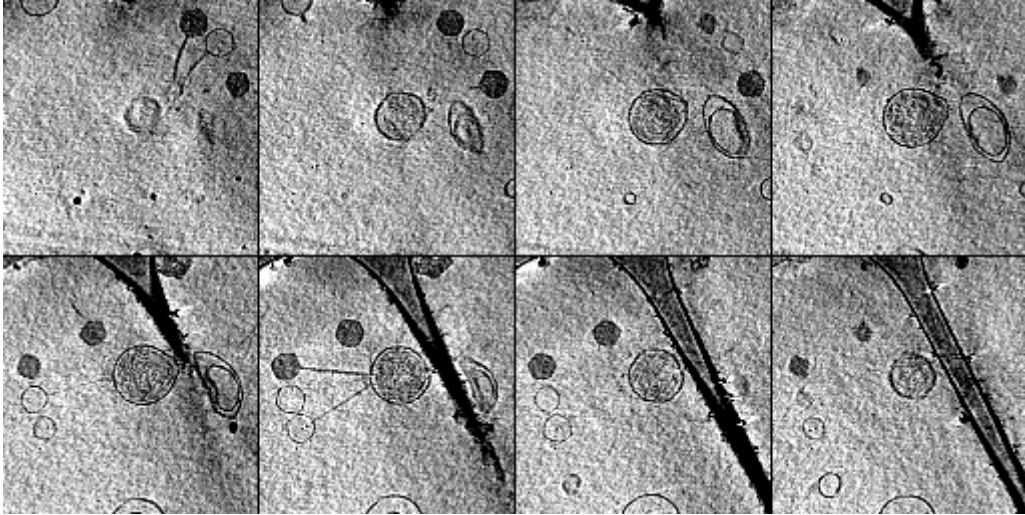


**Fig. 57.** Xy-slices from the original tomographic reconstruction of T5 viruses attached to proteoliposomes. In the center of the 3D image a vesicle can be observed with DNA inside, which has been injected by the six viruses attached.

In order to support the segmentation procedure the 3D image has been denoised with nonlinear anisotropic diffusion (Fig. 58). The contrast differences between the carbon foil and the vesicles are not very significant. Especially in the inner part of the carbon the gray values are brighter and consequently a thresholding scheme can not be applied. The result of the segmentation with level set is presented in chapter 4.

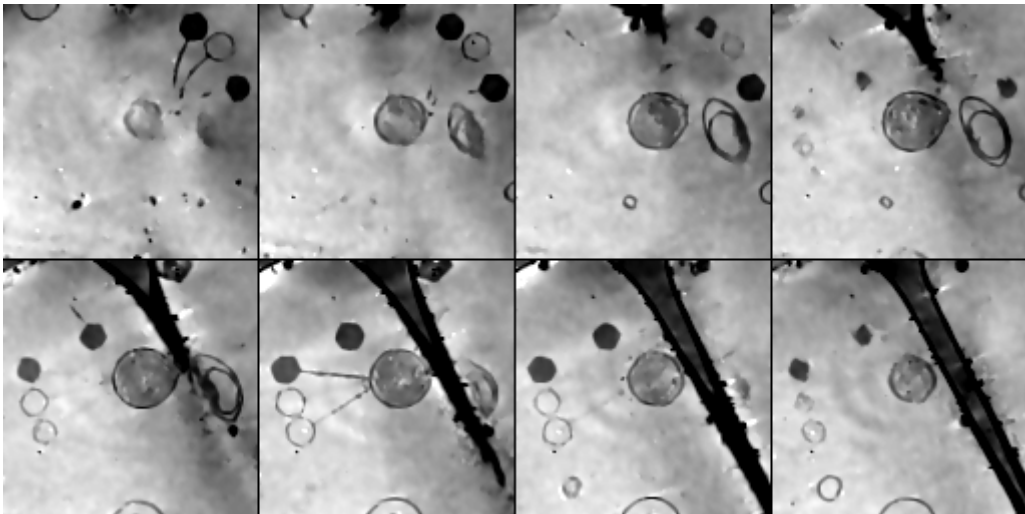


**Fig. 58.** Denoising with nonlinear anisotropic diffusion the xy-slices applied to the T5 viruses attached to proteoliposomes.

The segmentation result is absolutely satisfying (Fig. 59). In the segmented image the carbon film is precisely defined. Some viruses as well as the vesicle are also represented, but with less weight compared to the carbon film. By simply discretizing the 3D segmentation to a binary image a mask can be built, which is multiplied to the original reconstruction. Surface-rendered presentations are shown in Fig. 60 and 61. Several views to the vesicle are now possible.

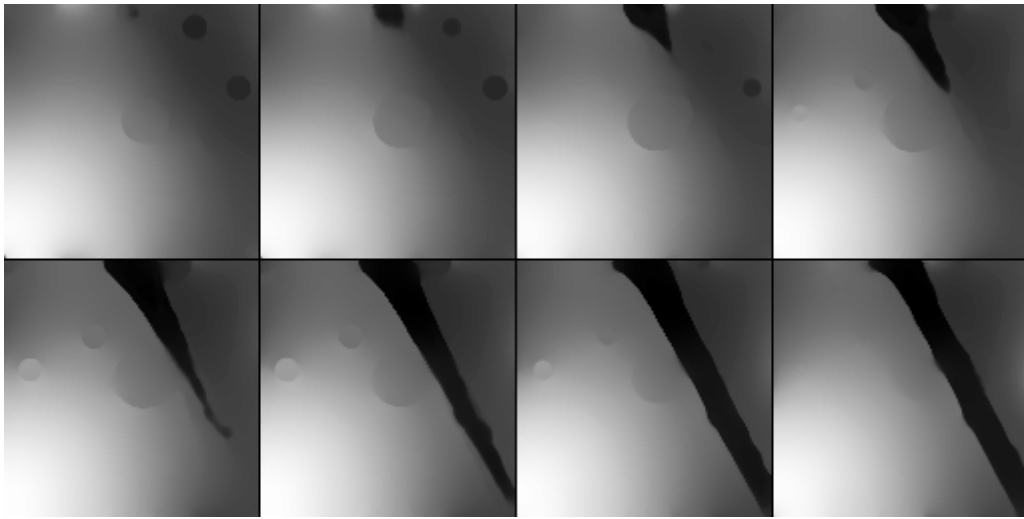


**Fig. 59.** The segmentation result. The separation of the carbon from the rest of the volume is achieved.

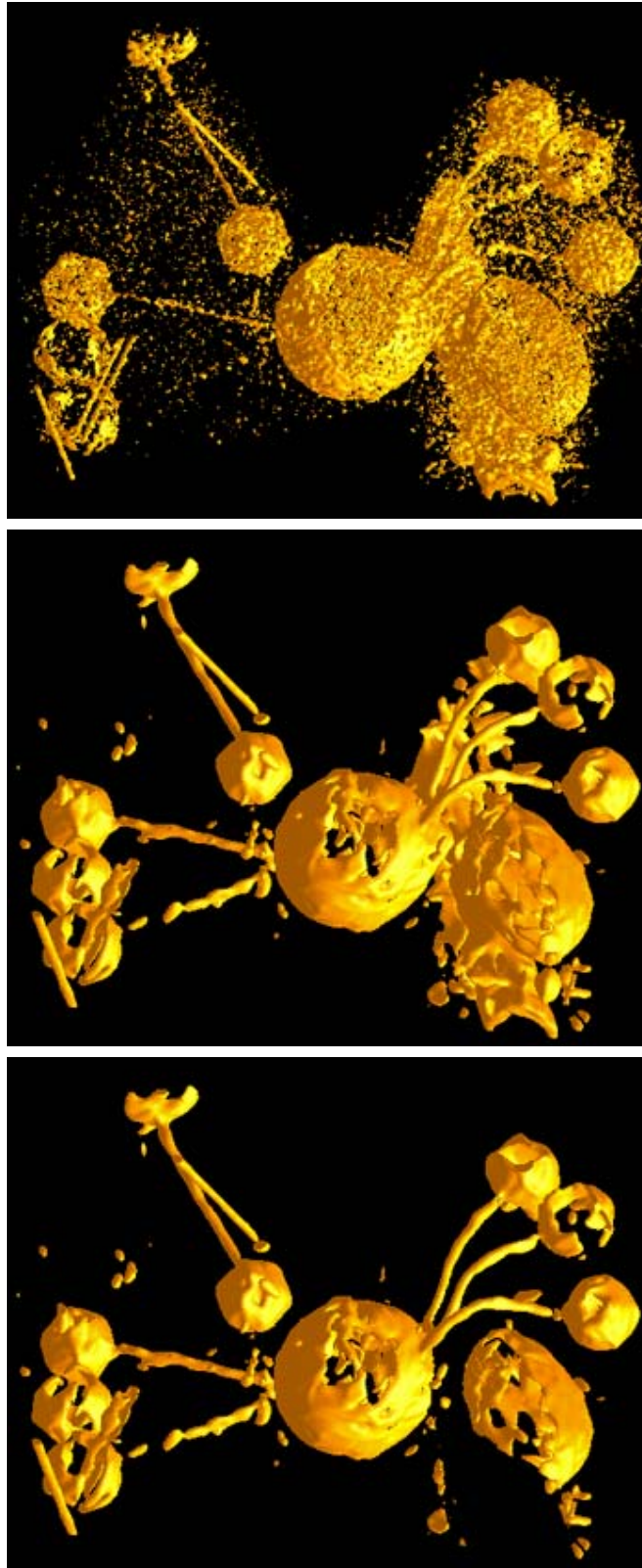


**Fig. 60.** Isosurface representation of the vesicle with the viruses attached. View from top (a) Original reconstructed 3D image, (b) after denoising with nonlinear anisotropic diffusion and (c) after segmentation

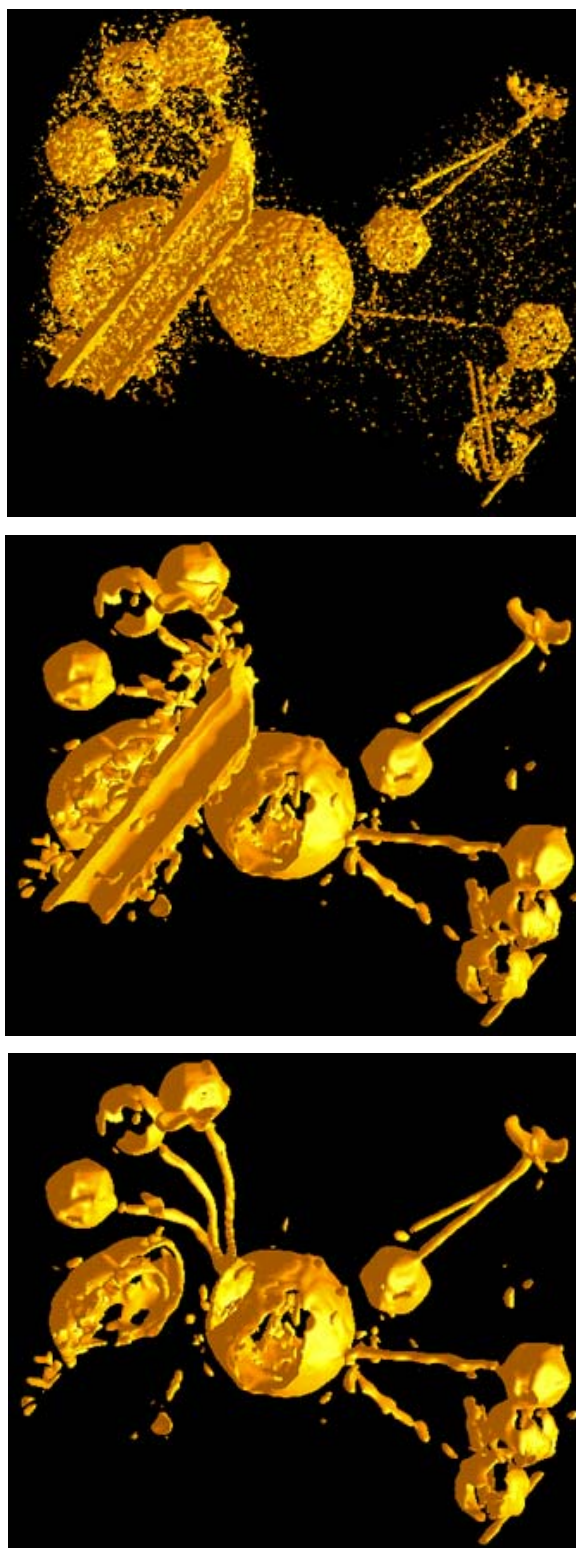


**Fig. 61.** A different view from the same isosurface presentation. The same order as in Fig. 60. In the segmented version the binding point of the tails at the vesicle can be visualized from the bottom side. This view would be not possible without segmentation.

### 5.3 Discussion

The segmentation with eigenvectors consists of several advantages compared to other methods and has one tremendous virtue: It always produces a plausible segmentation. The results are satisfying, especially for 2D images. In 3D images the missing wedge has some influence on the performance, nevertheless the segmentation outperforms any other applied technique. This technique is not restricted to the gray value images or to gradient calculations. Any kind of image similarity can be implemented in the affinity matrix and the eigenvectors are going to include it in the segmentation result.

From the computational point of view, the complexity grows linearly with the size of the processed images. In the 2D images the segmentation is always fast and reliable. In 3D images due to the large number of elements which must be included the memory resources can appear insufficient, but this is the only handicap of the method.

---

## References

- S. Achenbach, W. Moshage, and K. Bachmann (1996) "Coronary angiography by electron beam tomography", *Herz*, vol. 21, no. 2, pp. 106-117
- L. Alvarez, F. Guichard, P. L. Lions and J. M. Morel (1993) "Axioms and Fundamental Equations of Image Processing", *Archive for Rational Mechanics and Analysis*, vol. 123, pp. 199-257
- W. Baumeister, J. Walz, R. Grimm (1999) "Electron tomography of molecules and cells", *Trends in Cell Biology*, vol. 9, pp.81-85
- J. J. Benedetto (1998) "Noise reduction in terms of the theory of frames", *Signal and Image Representation in Combined Spaces*, Y. Y. Zeevi and R. R. Coifman (Eds.), Academic Press, pp. 259-284
- L. F. Bielak, R. B. Kaufmann, P. P. Moll, C. McCollough, R. S. Schwartz, and P. F. Sheedy (1994) "Small lesions in the heart identified at electron beam CT: calcification or noise", *Radiology*, vol. 192, pp. 631-636
- J. Boehm, A. S. Frangakis, R. Hegerl, S. Nickell, D. Typke, W. Baumeister (2000) "Towards detecting macromolecules in an unperturbed cellular context: Template matching applied to electron tomograms", *PNAS*, vol. 97, no. 26, pp. 14017-14874
- S. S. Chen, D. L. Donoho, and M. A. Saunders, (1999) "Atomic decomposition by basis pursuit", *SIAM J. of Scientific Computing*, vol. 20, no. 1, pp. 33-61
- I. Cohen, S. Raz, and D. Malah (1999) "Translation-invariant denoising using the minimum description length criterion", *Signal Processing*, vol. 75, no. 3, pp 201-223
- R.R. Coifman, and D.L. Donoho (1995) "Translation-invariant de-noising", in *Wavelets and Statistics*, Anestis Antoniadis (ed.), Springer, Lecture Notes in Statistics, pp. 225-250
- J. A. Cutrone, D. Georgiou, S. U. Khan, A. Pollack, M. M. Laks, and B. Brundage (1995) "Right ventricular mass measurement by electron beam computed tomography; validation with autopsy data", *Investigative Radiology*, vol. 30, no. 1, pp. 64-68
- I. Daubechies (1992) "Ten lectures on wavelets", *SIAM Publications*

- D. L. Donoho (1993) "Nonlinear wavelet methods for recovery of signals, images, and densities from noisy and incomplete data", American Mathematical Society, *Different Perspectives on Wavelets*, vol. 1, pp. 173-205
- D. L. Donoho (1995) "De-noising by soft thresholding", *IEEE Trans. on Information Theory*, vol. 41, no. 3, pp. 613-627
- A. S. Frangakis, R. Hegerl (1999) "Nonlinear anisotropic diffusion in three-dimensional electron microscopy", *Scale-Space Theories in Computer Vision*, Lecture Notes in Computer Science, Springer, Berlin, vol. 1682, pp. 386-397
- A. S. Frangakis, A. Stoschek, R. Hegerl (2001) "Wavelet transform filtering and nonlinear anisotropic diffusion assessed for signal reconstruction performance on multidimensional biomedical data", *IEEE Trans. Biomedical Eng.*, to appear
- M. Fiedler (1975) "A property of eigenvectors of nonnegative symmetric matrices and its application to graph theory" *Czech. Mathematical Journal*, vol. 25, pp. 619-633
- M. W. Grayson (1987) "The heat equation shrinks embedded plane curves to round points", *J. of Differential Geometry*, vol. 26, pp. 285-314
- R. Grimm, M. Baermann, W. Haeckl, D. Typke, E. Sackmann, W. Baumeister (1997) "Energy filtered electron tomography of ice-embedded actin and vesicles", *Bioph. J.*, vol. 72, pp. 482-489
- D. Grönemeyer, R. Seibel, R. Erbel, A. Schmidt, A. Melzer, J. Pläsmann, M. Deli, A. Schmermund, D. Baumgart, R. Welsch, J. Ge, and G. George (1996) "Equipment configuration and procedures: preferences for interventional micro therapy", *J. of Digital Imaging*, vol. 9, no. 2, pp. 81-96
- B. M. ter Harr Romeny (Ed.) (1994) *Geometry-driven diffusion in computer vision*, Kluwer, Dordrecht
- R. G. Hart (1968) *Science*, vol. 159, pp. 1464-1467
- S. Haykin (1994) *Neural Networks: a comprehensive foundation*, Macmillan
- R. Hegerl, and W. Hoppe (1976) "Influence of electron noise on three-dimensional image reconstruction", *Z. Naturforschung*, vol. 31, pp. 1717-1721
- R. Hegerl (1996) "The EM program package: a platform for image processing in biological electron microscopy", *Journal of Structural Biology*, vol. 116, pp. 30-34
- W. Hoppe, R. Langer, G. Knetsch, P. Poppe (1968) *Naturwissenschaften* 7, pp. 333-336
- R. A. Horowitz, A. J. Koster, J. Walz, C. L. Woodcock (1997) "Automated electron microscope tomography of frozen-hydrated Chromatin: the irregular three-dimensional

- Zigzag architecture persists in compact, isolated fibers”, *J. of Structural Biology*, vol. 120, pp. 353-362
- M. Kass, A. Witkin, D. Terzopoulos (1988) “Snakes: Active contour models”, *Int. J. Comput. Vision*, vol. 1, pp. 362-385
- A. J. Koster, R. Grimm, D. Typke, R. Hegerl, A. Stoschek, J. Walz, and W Baumeister (1998) “Perspectives of molecular and cellular electron tomography”, *J. of Structural Biology*, vol. 120, pp. 276-308
- J. Kovacevic, and M. Vetterli (1992) “Nonseparable multidimensional perfect reconstruction filter banks and wavelet basis for”, *IEEE Trans. on Information Theory*, vol. 38, no. 2, pp.533-555
- M. Lang, H. Guo, J. E. Odegard, C. S. Burrus, and R. O. Wells (1996) “Noise Reduction Using an Undecimated Discrete Wavelet Transform”, *IEEE Signal Processing Letters*, vol. 3, pp. 10-16
- J. Liang, and T. W. Parks (1996) “A translation-invariant wavelet representation algorithm with applications”, *IEEE Trans. on Signal Processing*, vol.44, no.2, pp.225-232
- R. Malladi, J. Sethian, B. C. Vemuri (1996) “A fast level set based algorithm for topology –independent shape modeling”, “*Journal of Mathematical Imaging and Vision*”, vol. 6, pp. 269-289
- S. G. Mallat (1989) “A theory for multiresolution signal decomposition: The Wavelet Representation”, *IEEE Trans. on PAMI*, vol. 11, no. 7, pp. 674-693
- S. G. Mallat, and Z. Zhang (1993) “Matching pursuits with time-frequency dictionaries”, *IEEE Trans. on Signal Processing*, vol. 41, no. 12, pp. 3397-3415
- J. Malik, S. Belognie, T. Leung, J Shi (1999) ”Contour and Texture Analysis for Image Segmentation”, submitted to *Int. J. Comp. Vision*
- W. E. Moshage, S. Achenbach, B. Seese, K. Gachmann, and M. Kirchgeorg (1995) “Coronary artery stenoses: three-dimensional imaging with electrocardiographically triggered, contrast agent-enhanced. Electron-Beam CT”, *Radiology*, vol. 196, pp. 707-714
- E. Mousseaux, A. Hernigou, M. Azencot, M. Sapoval, M. Auguste, and J. Gaux (1996) “Evaluation by electron beam computed tomography of intracardiac masses suspected by transoesophageal echocardiography”, *Heart*, vol. 76, pp. 256-263,
- D. Nicastro, A. S. Frangakis, D. Typke, W. Baumeister (2000) “Cryo-electron tomography of Neurospora mitochondria: three-dimensional organization and ultrastructure of whole ice-embedded organelles”, *J. Structural Biology*, vol. 129, pp. 48-56

- M. Nitsch, J. Walz, D. Typke, M. Klumpp, L. O. Essen, W. Baumeister (1998) "Group II chaperonin in an open conformation examined by electron tomography", *Nature Structural Biology*, vol. 5, nm. 10, pp.855-857
- S. Osher and J. A. Sethian (1988) "Fronts propagating with curvature dependent speed: Algorithms based on Hamilton-Jacobi formulation", *Journal of Computational Physics*, Vol. 79, pp. 12-49
- P. Perona, and J. Malik (1989) "Scale-space and edge detection using anisotropic diffusion", *IEEE Trans. on PAMI*, vol.12, no. 7, pp. 629-639
- J. Radon (1917) "Über die Bestimmung von Funktionen durch ihre Integralwerte längs gewisser Mannigfaltigkeiten" *Berlin Sächsische Akademie der Wissenschaften*, vol. 29, pp. 262-279
- B. Rockel, J. Walz, R. Hegerl, J. Peters, D. Typke, W. Baumeister (1999) "Structure of VAT, a CDC48/p97 ATPase homologue from the archaeon *thermoplasma acidophilum* as studied by electron tomography" *FEBS Letters*, vol. 451, pp.27-32
- D. J. de Rosier and A. Klug (1972) "Three-dimensional image reconstruction from the viewpoint of information theory" *Nature*, vol. 238, pp. 435-439
- W. O. Saxton, W. Baumeister (1982) "The correlation averaging of a regularly arranged bacterial cell envelope protein" *J. of Microscopy*, vol. 127, pp.127-138
- J. A. Sethian (1985) "Curvature and the Evolution of Fronts", *Communications in Mathematical Physics*, vol. 101, pp. 487-499
- J. A. Sethian (1996) "Level Set Methods Evolving Interfaces in Geometry, Fluid Mechanics, Computer vision, and Materials Science", Cambridge University Press
- M. J. Shensa (1992) "The discrete wavelet transform: wedding the a trous and Mallat algorithms", *IEEE Trans. on Signal Processing*, vol. 40, no. 10, pp. 2464-2482
- J. Shi, J. Malik (1997) "Normalized cuts and Image Segmentation", *Proc. IEEE Conf. on Comp. Vision and Pattern Recognition*, pp. 731-737
- E. P. Simoncelli, W. T. Freeman, E. H. Adelson, and D. J. Heeger (1992) "Shiftable multiscale transforms", *IEEE Trans. on Information Theory*, vol. 38, no. 2, pp. 587-607
- A. Stochek, R. Hegerl (1997) "Denoising of Electron tomographic reconstructions using multiscale transformations", *J. Structural Biology*, vol. 120, pp. 257-265
- A. Stoschek, T. P. Y. Yu, and R. Hegerl (1997) "Denoising of electron tomographic reconstructions from biological specimen using multidimensional multiscale

transforms”, *Proc. of the 1997 Int. Conf. on Acoustics, Speech, and Signal Processing*, München, Germany, IEEE Computer Society Press, vol. 4, pp. 2793-2796

A. Stoschek, X. Huo (1999) "Experiments with combined image transforms and its implications for biomedical image analysis", International Workshop on Digital and Computational Video, Tampa, USA

G. Strang, T. Nguyen (1996) *Wavelets and filter banks*, Wellesley-Cambridge, Wellesley

M. Unser, P. Thevanaz, and L. Yaroslavski (1995) “Convolution-based interpolation for fast high-quality rotation of images”, *IEEE Trans. on Image Processing*, vol. 4, no. 10, pp. 1371-1381

S. Wang, R. Detrano, A. Secci, W. Tang, T. Doherty, G. Puentes, N. Wong, and B. Brundage (1996) “Detection of coronary calcification with electron-beam computed tomography: Evaluation of interexamination reproducibility and comparison of three image-acquisition protocols”, *American Heart Journal*, vol. 132, no. 3, pp. 550-558

J. Weickert (1994) “Scale-space properties of nonlinear diffusion filtering with a diffusion tensor”, report no. 110, Laboratory of Technomathematics, University of Kaiserslautern, Germany

J. Weickert (1998) *Anisotropic diffusion in image processing*, B. G. Teubner Stuttgart

J. Weickert (1999) ”Coherence enhancing diffusion filtering” *Int. J. of Computer Vision*, vol. 31, No. 2/3, pp. 111-127, 1999

Y. Weiss (1999) “Segmentation using eigenvectors: a unifying view”, *Proc. Int. Conf. Comp. Vision*, vol.2, pp. 975-982

A. P. Witkin (1983) “Scale-space filtering”, *Proc. 8th International Joint Conference on Artificial Intelligence*, vol.2, pp.1019-1022

Witkin, D. Terzopoulos, M. Kass (1987) “Signal matching through scale-space”, *Int. J. Comput. Vision*, vol. 1, pp. 134-144

T. Yu, A. Stoschek, and D. Donoho (1996) “Translation- and direction-invariant denoising of 2D and 3D images: Experience and algorithms”, *Proc. of the SPIE, Wavelet App. in Signal and Image Processing IV*, vol. 2825, pp. 608-619